CURRENT STATE OF ALASKA'S GLACIERS AND EVOLUTION OF BLACK RAPIDS GLACIER CONSTRAINED BY OBSERVATIONS AND MODELING

By

Christian Kienholz, B.S., M.S.

A Dissertation Submitted in Partial Fulfillment of the Requirements

for the Degree of

Doctor of Philosophy

in

Geophysics

University of Alaska Fairbanks

December 2016

APPROVED:

Dr. Regine Hock, Committee Chair
Dr. Anthony Arendt, Committee Member
Dr. Andrew Bliss, Committee Member
Dr. Matthias Braun, Committee Member
Dr. Franz Meyer, Committee Member
Dr. Martin Truffer, Committee Member
Dr. Paul McCarthy, Chair
Department of Geosciences
Dr. Paul Layer, Dean
College of Natural Science and Mathematics
Dr. Michael Castellini, *Dean of the Graduate School*

Abstract

Glaciological studies rely on a wide range of input data, the most basic of which, accurate glacier extents, were not available on an Alaska wide scale prior to this work. We thus compiled a glacier database for Alaska and neighboring Canada using multi-sensor satellite data from 2000 to 2011. The inventory yielded a glacierized area of 86,720 km^2, which corresponds to ~12% of the global glacierized area outside the ice sheets. For each of the ~27,100 glaciers, we derived outlines and 51 variables, including centerline lengths, outline types, and debris cover, which provide key input for observational and modeling studies across Alaska. Expanding on this large-scale observational snapshot, we conducted two case studies on Black Rapids Glacier, Eastern Alaska Range, to assess its evolution during the late 20th and 21st centuries. Black Rapids Glacier, 250 km^2 in area, was chosen given its surge-type dynamics and proximity to critical infrastructure. Remotely sensed and in-situ elevation observations over the 1980–2001–2010 period indicated strong mass loss of Black Rapids Glacier (~0.5 m w.e. a^{-1}), with higher thinning rates over the 2001–2010 (~0.65 m w.e. a^{-1}) than the 1980–2001 period (~0.4 m w.e. a^{-1}). A coupled surface mass balance-glacier dynamics model, driven by reanalysis climate data, reproduced the glacier shrinkage. It identified the increasingly negative summer balances, a consequence of the warming atmosphere, as the main driver for the negative mass balance trend. Elevation observations in Black Rapids' surge reservoir suggested a surge was not imminent at the time of the analysis due to the lack of ice thickening. Re-initiation of sufficient elevation growth in the surge reservoir would require more favorable surface mass balances, as observed in the early 1980s. Compared to nearby Gulkana Glacier (a USGS benchmark glacier), the observed specific mass losses at Black Rapids Glacier were less pronounced, ~0.4 vs. 0.5 m w.e. a^{-1} (1980–2001) and ~0.65 vs. 0.95 m w.e. a^{-1} (2001–2010). The larger difference between the two glaciers' mass balances over the 2001–2010 period was partly caused by rockslide debris deposited on Black Rapids Glacier in 2002. This ~4.5 m thick debris layer, spread across 11.7 km^2 of Black Rapids lower ablation area, was modeled to suppress Black Rapids' glacier wide mass loss by ~20%. Modeling Black Rapids' evolution until 2100 suggested sustained glacier retreat, even under a repeated constant climate scenario, with ~225 km^2 of area remaining in 2100. Using a warming scenario (RCP 8.5), the modeled retreat was strongly accelerated with only ~50 km^2 of glacier area left in 2100. Given its thick, low-slope valley portion, Black Rapids Glacier is very susceptible to climate change. Its neighboring glaciers in the Eastern Alaska Range have similar properties, suggesting region wide glacier retreat in the future. To constrain this further, the Black Rapids case studies should be extended to the regional scale, a step now facilitated by the new Alaska wide glacier database.

Table of Contents

List of Figures

List of Tables

List of Appendices

Acknowledgements

Thank you to my advisor Regine Hock and committee members Anthony Arendt, Martin Truffer, Franz Meyer, Andy Bliss and Matthias Braun for taking me on as a PhD student and for critical guidance throughout the last five years. In their own ways, they each contributed greatly to the successful course of my PhD. My advisor Regine's passion for glaciers and science has been extraordinary. She has made her students' progress one of her highest academic priorities and thus always gave precise, immediate feedback and the right amount of encouragement when needed. By frequently hosting potlucks and baking cakes for the Glaciers people, Regine also proved important for the social life of our research group. Thanks to Regine for canoeing tours, downhill skiing, table tennis games, and field work opportunities on the Jarvis and Susitna Glaciers. Anthony Arendt was my co-advisor until he moved on to take a position at the University of Washington (UW) in 2014. Even after leaving for UW, Anthony supported my research with both advice and important funding, which is very much appreciated. As a gifted speaker and writer, Anthony always had excellent feedback. He spearheaded new IT technologies and often took the lead on many IT related tasks while part of the Glaciers Group. Road biking and cross-country skiing with Anthony was a welcome diversion from the work in the lab; skiing with him sure improved my cross-country technique. Martin Truffer was a great teacher whose ideas and feedback, and advice in general, were always welcome. Martin enabled my exchange to the University of Alaska Fairbanks (UAF) in 2009, after which I decided to pursue graduate school here. Martin took me along for fieldwork, teaching me that it can be both productive and much fun. Thank you to Martin for partly funding the latter part of my PhD. Thanks also for raclette dinners and memorable flights from Fairbanks to Black Rapids Glacier and across the Hayes Range, to the White Mountains and the 'Into the Wild' bus. Franz Meyer has been very positive and supportive throughout my MS and PhD. His curiosity outside his immediate field of research and his commitment to excellent teaching and research have been very inspiring. Andy Bliss joined my committee in the later part of my PhD and helped whenever needed. I always appreciated Andy's calm and friendly personality. Thank you Andy and your family for hosting several Thanksgiving celebrations over the years. Matthias Braun was the PI on the National Aeronautics and Space Administration (NASA) project that funded my first three years of graduate school. Although we had only a few days of overlap in Fairbanks back in 2011, we remained in contact over the years to come. A highlight was the exchange to the University of Erlangen, where Matthias organized a great stay.

In addition to my committee members, many thanks to Chris Larsen, Mark Fahnestock and Will Harrison for their always thoughtful feedback during seminars. Thank you to Andy

Aschwanden for discussing questions and thoughts whenever needed, and for stopping by with high-end chocolate on an almost daily basis. Thank you to all my fellow students, especially my office mate Aurora Roth, who improved many working days with her cheerful personality. Technicians Sam Herreid and Justin Rich are very much acknowledged for having spent many hours on creating outlines for the inventory project. Regular discussions with Justin Rich helped improve my programming skills.

Outside our group, thanks to Shad O'Neel from the United States Geological Survey (USGS) for giving me ample field work opportunities. The USGS trip to Scott Glacier in 2014 with Louis Sass and Dan McGrath was among my best field trips in Alaska. Likewise, Gabe Wolken from the Alaska Division of Geological & Geophysical Surveys is acknowledged for fieldwork opportunities and continued interest in my research.

Thank you to Brian Anderson from the University of Wellington, New Zealand, for providing modeling code and ideas during my stay there in 2015. Jon-Ove Hagen from the University of Oslo and Luke Copeland from the University of Ottawa are both acknowledged for their organizational work for the Norwegian exchange program GlacioEx, which provided many useful exchange and course opportunities. As part of GlacioEx, I was able to stay at the University of Oslo twice and participate in field courses in Canada and Iceland.

Many thanks to Heinz Zumbühl and Samuel Nussbaumer for the support throughout my studies at the University of Bern in Switzerland. They were instrumental to my decision to continue in glaciology rather than moving on with geology in Switzerland. Heinz Zumbühl introduced me to Martin Truffer in 2008, which resulted in my exchange to UAF in 2009 and thus ultimately my PhD. Thank you to Peter Mani, director at *geo7*, who understood my desire to return to Alaska, and who has kept great interest in my path since.

Thank you to my parents Markus and Ursula in Switzerland, and my brothers Peter and Mathias and both their families in Australia, for their support throughout my PhD. Participating in your very different lives in very different places was enriching. I will always remember our calls throughout the Alaska winter/Australia summer when our places were as different as they could possibly be. My dad's love for engineering has always been inspiring and kept reminding me that I should do much more of that in the future.

Finally, special thanks to Gabrielle for spending a great five years with me in Fairbanks, in the same state but still far away from beloved Juneau. Gabrielle's supportive and understanding spirit has been truly amazing; skiing, hiking, biking, and canoeing across the U.S., New Zealand and Switzerland were much fun, too. Thank you also to Gabrielle's family for providing a warm welcome during our ski trips to Juneau.

Thank you to NASA, the National Science Foundation, the National Park Service, and the UAF Graduate School for grants and scholarships which made my PhD possible. I am grateful for having had the opportunity to learn and progress in an ideal place for glaciology.

Chapter 1
General Introduction

Alaska and neighboring Canada host ~12% of the global glacierized area outside the ice sheets. Since the end of the Little Ice Age in the 18th century, these glaciers have undergone strong retreat (Molnia, 2008) with many consequences, the most prominent of which is global sea level rise (e.g., Radić et al., 2014). The retreat has caused strong isostatic rebound (e.g., Larsen et al., 2005), which in many Alaska regions close to glaciers (e.g., coastal communities like Juneau) has far exceeded the impact of sea level rise. Glacier wastage across Alaska is anticipated to change the amount and timing of stream runoff, which may affect important fish migrations but also have consequences as far reaching as regional ocean circulation (O'Neel et al., 2015). Given such broad impacts, advancing our knowledge about Alaska's glaciers and their change is important.

Prior to the 1950s, Alaska's glaciers were documented sporadically by sketches, photographs and early maps (Molnia, 2008). The first Alaska wide USGS maps, created in the 1950s, documented the glaciers systematically but with limited accuracy. Though the Alaska High Altitude Aerial Photography (AHAP) program covered all of Alaska in the late 1970s and early 1980s, these images were not used to update the USGS maps systematically. Given the strong glacier retreat since the 1950s and the lack of systematic updates, Alaska's USGS maps are outdated today.

In the 1990s, airborne laser altimetry surveys were initiated by the University of Alaska Fairbanks Geophysical Institute to quantify glacier changes by comparing the altimetry-derived glacier elevations to the 1950 map elevations (Echelmeyer et al., 1996). While these studies focused on individual glaciers initially (e.g., Sapiano et al., 1998), the methods were later refined to determine Alaska wide glacier changes (Arendt et al., 2002, 2006). Repetition of altimetry surveys every few years ultimately allowed for determining glacier changes among individual altimetry surveys (e.g., Arendt et al., 2006). While this marked an important step forward, these studies faced the problem that the outline and area-altitude distributions available did not match the dates of the altimetry surveys, thus increasing the results' uncertainties. In the late 2000s, with more powerful computers, region wide glacier modeling studies complemented the above observational studies (e.g., Radić and Hock, 2011). Like the altimetry studies, they required accurate glacier outlines and area-altitude distributions and were thus affected by the lack of a modern glacier inventory.

In 2008, a team led by Anthony Arendt and Regine Hock at the UAF Geophysical Institute initiated an effort to compile a new glacier inventory for Alaska and neighboring Canada based on modern satellite imagery. The National Park Service funded the first part of the project, so initial efforts focused on Alaska's nine glacierized National Parks, which contain approximately

half (~44,000 km^2) of the ice in the entire region (Loso et al., 2014). Parallel studies conducted at the University of Zurich (Le Bris et al., 2011) and the University of Northern British Columbia (Bolch et al., 2010) obtained outlines for ~16,000 km^2 of ice in Western Alaska and ~18,000 km^2 in the Coast Mountains. To reach Alaska wide coverage, the remaining outline gaps (~9000 km^2 of ice across several regions) had to be filled. This work, funded by NASA as part of a regional modeling study, resulted in the first PhD project, presented here as Chapter 2. The goals of this project were to:

- Complete the Alaska wide glacier inventory
- Derive additional inventory products/attributes
- Provide relevant inventory statistics.

The outlining efforts were conducted manually using imagery from Landsat and other satellites. Attributes and derivative products were derived based on both previous (Kienholz et al., 2013, 2014) and newly developed workflows, which were designed to be applicable to many glaciers. The final glacier database comprised more than 50 variables, among them a vector product distinguishing four glacier margin types (glacier divides, land-terminating boundaries, lake-terminating boundaries, marine-terminating boundaries), a vector product containing glacier centerlines, and a gridded product representing debris cover. While we distributed intermediate versions of the inventory for several studies (e.g., Radić et al., 2014), the inventory was completely finished in 2015. The laser altimetry processing pipeline (Larsen et al., 2015) and several other observational and modeling studies (e.g., Fahnestock et al., 2015; Ziemen et al., 2016) began using the new inventory products the same year. The final outlines and selected attributes were submitted to the Randolph Glacier Inventory (RGI, http://www.glims.org/RGI/randolph.html, Pfeffer et al., 2014), from where they have been freely available since RGI version 4.0. We also set up a relational database at the Geophysical Institute hosting the full glacier inventory. The study's accompanying paper was published in the Journal of Glaciology (Kienholz et al., 2015).

While the inventory study provided a comprehensive large-scale observational snapshot of Alaska's glaciers, glacier changes were not quantified during that project. To focus on the glacier change aspect, we conducted two case studies on Black Rapids Glacier, Eastern Alaska Range, which complement similar case studies in other regions of Alaska and neighboring Canada (e.g., Flowers et al., 2011; Trüssel et al., 2013, 2015; Ziemen et al., 2016). We chose Black Rapids Glacier given its surge-type dynamics, proximity to critical infrastructure, and long research history. The overarching goals of these two case studies were to:

- Use observations to determine Black Rapids' area and mass changes over the past decades

- Pair the observations with a glacier model to reconstruct the glacier's recent behavior and project it into the future
- Interpret observations and model results with regard to Black Rapids' surge recurrence.

We emphasized surge recurrence given its poorly understood interaction with climate warming. Climate warming may affect both surge recurrence intervals and magnitudes, however, glaciers might also cease surging entirely (Dowdeswell et al., 1995; Eisen et al., 2001; Flowers et al., 2011; Bevington and Copland, 2014). Prior to our case studies, it was not completely clear which of these options would apply to Black Rapids Glacier.

The first Black Rapids case study used a wide range of observations (DEMs, laser altimetry data, in situ elevation measurements, satellite imagery) to reconstruct Black Rapids' mass balance over the time periods 1980–2001–2010. This work indicated area and mass losses, which were particularly marked over the more recent period (2001–2010). Large rockslide deposits and terrain displacements triggered by the M 7.9 Denali Fault earthquake in 2002 complicated the analysis (Jibson et al., 2006; Elliott et al., 2007). We quantified the effects of both processes on the glacier mass balance, which had only been approximated previously. As part of this study, we also assessed the applicability of the 1980 AHAP imagery to the derivation of historical glacier elevation information.

The second case study focused on modeling aspects. We implemented a surface mass balance–glacier dynamics model to reconstruct Black Rapids' mass balance time series for the period 1980–2015 and to project it for the period 2015–2100. The study showed Black Rapids Glacier in a severe state of disequilibrium with the climate, indicating continued glacier retreat in the future. The study also indicated a surge in the near future to be unlikely. As part of the second case study, we evaluated a new product for the climate forcing, which proved to be a step forward compared to climate data used in previous studies.

The two Black Rapids case studies each resulted in a paper, given here as Chapters 3 and 4. The first paper was published in the Journal of Geophysical Research: Earth Surface (Kienholz et al., 2016) and the second one is in preparation for submission to Frontiers in Earth Science.

All three studies relied on extensive datasets, which we compiled and analyzed in a relational database environment. Aside from evaluating the scientific problems, the studies were ideal for exploring methodological questions with regard to data hosting and analysis, for example, how to best integrate the database with a glacier model.

References

Arendt, A., K. Echelmeyer, W. Harrison, C. Lingle, S. Zirnheld, V. Valentine, B. Ritchie, and M. Druckenmiller (2006). Updated estimates of glacier volume changes in the western Chugach Mountains, Alaska, and a comparison of regional extrapolation methods. *Journal of Geophysical Research 111*(F3), F03019.

Arendt, A. A., K. A. Echelmeyer, W. D. Harrison, C. S. Lingle, and V. B. Valentine (2002). Rapid wastage of Alaska glaciers and their contribution to rising sea level. *Science 297*(5580), 382–386.

Bevington, A. and L. Copland (2014). Characteristics of the last five surges of Lowell Glacier, Yukon, Canada, since 1948. *Journal of Glaciology 60*(219), 113–123.

Bolch, T., B. Menounos, and R. Wheate (2010). Landsat-based inventory of glaciers in western canada, 1985-2005. *Remote Sensing of Environment 114*(1), 127–137.

Dowdeswell, J., R. Hodgkins, A. Nuttall, J. Hagen, and G. Hamilton (1995). Mass balance change as a control on the frequency and occurrence of glacier surges in Svalbard, Norwegian High Arctic. *Geophysical Research Letters 22*(21), 2909–2912.

Echelmeyer, K., W. Harrison, C. Larsen, J. Sapiano, J. Mitchell, J. DeMallie, B. Rabus, G. Adalgeirsdottir, and L. Sombardier (1996). Airborne surface profiling of glaciers: a case-study in Alaska. *Journal of Glaciology 42*(142), 538–547.

Eisen, O., W. Harrison, and C. Raymond (2001). The surges of Variegated Glacier, Alaska, USA, and their connection to climate and mass balance. *Journal of Glaciology 47*(158), 351–358.

Elliott, J. L., J. T. Freymueller, and B. Rabus (2007). Coseismic deformation of the 2002 Denali fault earthquake: contributions from synthetic aperture radar range offsets. *Journal of Geophysical Research: Solid Earth (1978–2012) 112*(B6), B06421.

Fahnestock, M., T. Scambos, T. Moon, A. Gardner, T. Haran, and M. Klinger (2015). Rapid large-area mapping of ice flow using Landsat 8. *Remote Sensing of Environment 185*, 84–94.

Flowers, G., N. Roux, S. Pimentel, and C. Schoof (2011). Present dynamics and future prognosis of a slowly surging glacier. *The Cryosphere 5*(1), 299–313.

Jibson, R. W., E. L. Harp, W. Schulz, and D. K. Keefer (2006). Large rock avalanches triggered by the M 7.9 Denali Fault, Alaska, earthquake of 3 November 2002. *Engineering Geology 83*(1), 144–160.

Kienholz, C., S. Herreid, J. Rich, A. Arendt, R. Hock, and E. Burgess (2015). Derivation and analysis of a complete modern-date glacier inventory for Alaska and northwest Canada. *Journal of Glaciology 61*(227), 403–420.

Kienholz, C., R. Hock, and A. A. Arendt (2013). A new semi-automatic approach for dividing glacier complexes into individual glaciers. *Journal of Glaciology 59*(217), 913–925.

Kienholz, C., R. Hock, M. Truffer, A. A. Arendt, and S. Arko (2016). Geodetic mass balance of surge-type Black Rapids Glacier, Alaska, 1980–2001–2010, including role of rockslide deposition and earthquake displacement. *Journal of Geophysical Research: Earth Surface 121*, 1–24.

Kienholz, C., J. L. Rich, A. A. Arendt, and R. Hock (2014). A new method for deriving glacier centerlines applied to glaciers in Alaska and northwest Canada. *The Cryosphere 8*(2), 503–519.

Larsen, C., E. Burgess, A. Arendt, S. O'Neel, A. Johnson, and C. Kienholz (2015). Surface melt dominates Alaska glacier mass balance. *Geophysical Research Letters 42*(14), 5902–5908.

Larsen, C. F., R. J. Motyka, J. T. Freymueller, K. A. Echelmeyer, and E. R. Ivins (2005). Rapid viscoelastic uplift in southeast Alaska caused by post-Little Ice Age glacial retreat. *Earth and Planetary Science Letters 237*(3), 548–560.

Le Bris, R., F. Paul, H. Frey, and T. Bolch (2011). A new satellite-derived glacier inventory for Western Alaska. *Annals of Glaciology 52*(59), 135–143.

Loso, M., A. Arendt, C. F. Larsen, J. L. Rich, and N. Murphy (2014). Alaskan National Park Glaciers: Status and Trends. Technical report, National Park Service, Fort Collins, Colorado.

Molnia, B. F. (2008). Glaciers of North America – Glaciers of Alaska. In R. S. William and J. G. Ferrigno (Eds.), *Satellite image atlas of glaciers of the world*. U.S. Geological Survey Professional Paper 1386-E, 525 pp.

O'Neel, S., E. Hood, A. L. Bidlack, S. W. Fleming, M. L. Arimitsu, A. Arendt, E. Burgess, C. J. Sergeant, A. H. Beaudreau, K. Timm, et al. (2015). Icefield-to-ocean linkages across the northern Pacific coastal temperate rainforest ecosystem. *BioScience 65*(5), 499–512.

Pfeffer, W. T., A. A. Arendt, A. Bliss, T. Bolch, J. G. Cogley, A. S. Gardner, J. O. Hagen, R. Hock, G. Kaser, C. Kienholz, E. S. Miles, G. Moholdt, N. Mölg, F. Paul, V. Radić, P. Rastner, B. H. Raup, J. L. Rich, and M. J. Sharp (2014). The Randolph Glacier Inventory: a globally complete inventory of glaciers. *Journal of Glaciology 60*(221), 537–552.

Radić, V., A. Bliss, A. C. Beedlow, R. Hock, E. Miles, and J. G. Cogley (2014). Regional and global projections of twenty-first century glacier mass changes in response to climate scenarios from global climate models. *Climate Dynamics 42*(1), 37–58.

Radić, V. and R. Hock (2011). Regionally differentiated contribution of mountain glaciers and ice caps to future sea-level rise. *Nature Geoscience 4*(2), 91–94.

Sapiano, J., W. Harrison, and K. A. Echelmeyer (1998). Elevation, volume and terminus changes of nine glaciers in North America. *Journal of Glaciology 44*(146), 119–135.

Trüssel, B. L., R. J. Motyka, M. Truffer, and C. F. Larsen (2013). Rapid thinning of lake-calving Yakutat Glacier and the collapse of the Yakutat Icefield, southeast Alaska, USA. *Journal of Glaciology 59*(213), 149–161.

Trüssel, B. L., M. Truffer, R. Hock, R. J. Motyka, M. Huss, and J. Zhang (2015). Runaway thinning of the low-elevation Yakutat Glacier, Alaska, and its sensitivity to climate change. *Journal of Glaciology 61*(225), 65–75.

Ziemen, F., R. Hock, A. Aschwanden, C. Khroulev, C. Kienholz, A. Melkonian, and J. Zhang (2016). Modeling the evolution of the Juneau Icefield between 1971 and 2100 using the Parallel Ice Sheet Model (PISM). *Journal of Glaciology 62*(231), 199–214.

Chapter 2

Derivation and analysis of a complete modern-date glacier inventory for Alaska and northwest Canada[1]

2.1 Abstract

We present a detailed, complete glacier inventory for Alaska and neighboring Canada using multi-sensor satellite data from 2000 to 2011. For each glacier, we derive outlines and 51 variables, including centerline lengths, outline types, and debris cover. We find 86,723 km^2 of glacier area (27,109 glaciers $>$ 0.025 km^2), ~12% of the global glacierized area outside ice sheets. 12.0% of the area is drained by 39 marine-terminating glaciers (74 km of tidewater margin) and 19.3% by 148 lake- and river-terminating glaciers (420 km of lake-/river margin). The overall debris cover is 11%, with considerable differences among regions, ranging from 1.4% in the Kenai Mountains to 28% in the Central Alaska Range. Comparison of outlines from different sources on $>$ 2500 km^2 of glacierized area yields a total area difference of ~10%, emphasizing the difficulties in accurately delineating debris-covered glaciers. Assuming fully correlated (systematic) errors, uncertainties in area reach 6% for all Alaska glaciers, but further analysis is needed to explore adequate error correlation scales. Preliminary analysis of the glacier database yields a new set of well constrained area/length scaling parameters and shows good agreement between our area-altitude distributions and previously established synthetic hypsometries. The new glacier database will be valuable to further explore relations between glacier variables and glacier behavior.

2.2 Introduction

Comprehensive glacier inventories are essential for many applications in glaciology. An inventory allows for describing the state of a glacierized region (e.g., Schiefer et al., 2008; Radić and Hock, 2010; Frey et al., 2012), while comparing multitemporal inventories allows for quantifying glacier changes (e.g., Nuth et al., 2013). Glacier inventories are also required to extrapolate local mass balance measurements to individual glaciers and entire regions (e.g., Arendt et al., 2006). They further provide the starting point for projections of glacier evolution (Marzeion et al., 2012; Radić et al., 2014). If glacier inventories are incomplete, up/down-scaling procedures are required (Radić and Hock, 2010; Bahr and Radić, 2012), significantly increasing uncertainty in the model results (Radić and Hock, 2011). With the increasing number of regional and global glaciological and hydrological assessments (e.g., Bliss et al., 2014), the importance of large-scale glacier inventories has grown.

[1]Published as Kienholz, C., S. Herreid, J. L. Rich, A. A. Arendt, R. Hock, and E. W. Burgess (2015), Derivation and analysis of a complete modern-date glacier inventory for Alaska and northwest Canada, *Journal of Glaciology 61* (227), 403–420.

A substantial portion (~12%) of the global mountain glaciers and ice caps are located in Alaska and adjacent Canada (henceforth referred to as 'Alaska glaciers'). The earliest complete maps of glacier extent were built from U.S. Geological Survey (USGS) aerial photography acquired mostly in the late 1940s and early 1950s, and in adjacent Canada from Natural Resources Canada (NRCAN) photography acquired in the 1970s and 1980s. Incorrect interpretation of seasonal snow and debris-covered ice, in addition to technical blunders (e.g., systematic shifts due to lacking ground control), resulted in numerous erroneous glacier outlines. Nevertheless, digital versions of these outlines were used in many regional mass balance assessments (e.g., Arendt et al., 2002; Larsen et al., 2007; Berthier et al., 2010). In light of the widespread glacier retreat since the compilation of the first maps (Barrand and Sharp, 2010; Bolch et al., 2010; Le Bris et al., 2011), the glacier outlines further became outdated, increasing the need for a detailed, modern-date inventory for Alaska.

In 2008, the University of Alaska Fairbanks (UAF) initiated an effort to compile a complete modern-date glacier inventory for Alaska based on extensive manual digitization from satellite imagery combined with modern-date outlines from parallel studies (e.g., Bolch et al., 2010; Le Bris et al., 2011), submitted to the global GLIMS database (http://glims.org, Raup et al., 2007). Since 2012, versions of the inventory have been released and used, for example, to determine glacier changes within Alaska's National Parks (Loso et al., 2014). The inventory has also contributed to the global Randolph Glacier Inventory (RGI, Pfeffer et al., 2014).

Our new inventory version presented here is a major step forward compared to previous versions. It includes glacier divides improved substantially with measured velocity fields (Burgess et al., 2013), more complete metadata, and a greatly expanded set of derived attributes and datasets than presented for Alaska in Pfeffer et al. (2014). Our latest database includes more than 50 derived variables across 17 main categories. Among the derived datasets are a vector product that distinguishes four glacier margin types (glacier divides, land-terminating boundaries, lake-terminating boundaries, marine-terminating boundaries), a vector product containing glacier centerlines (including side branches), and a gridded product representing debris cover.

The main goal of this paper is to present the applied techniques, to assess the quality of the derived products, and to give an overview of the inventory statistics. In addition, we perform preliminary analyses of selected inventory variables, and derive, for example, area-length scaling relations and characteristic debris curves as a function of elevation.

2.3 Study area

Our study area, identical to the RGI region 1, covers Alaska, southwest Yukon and northwest British Columbia (Figure 2.1a). Glaciers cluster mainly along the mountain ranges of the southern

Alaska coast, an area characterized by maritime climate and topography reaching > 5000 m a.s.l.. The extreme relief is an effective barrier for the prevailing southwestern winds (e.g., Shulski and Wendler, 2007), causing high annual accumulation rates and thus favorable conditions for glaciers. Further to the north, the climate is more continental and supports only smaller glaciers. The Brooks Range, the northernmost inventoried region, has few glaciers despite its location north of 65°N and elevations > 3000 m a.s.l., due to extremely low precipitation rates (Geck et al., 2013).

We divide the inventoried glaciers into 21 subregions based on previous work (Field, 1975; Molnia, 2008) and with modifications for practical purposes. While these inventory regions group glaciers of the same mountain range or subrange together, they can extend across multiple watersheds and climate zones, which often have their boundaries over glacierized terrain (e.g., Bieniek et al., 2012). Bering Glacier is unique as it originates in the St. Elias Mountains and ends in the Eastern Chugach Mountains. We allocate Bering Glacier to the Eastern Chugach Mountains as splitting of the glacier's accumulation and ablation areas would be impractical.

2.4 Data

2.4.1 Satellite imagery

Glacier outlines are derived from optical satellite imagery from four sources: IKONOS, Landsat, ASTER, and SPOT (Table 2.1). For the mapping of glacier debris cover, we use Landsat 5 imagery only. The source imagery covers mostly the period 2004 to 2010; in areas with persistent cloud coverage, it dates back as far as 2000 (Figure 2.1b,c). Given its outstanding spatial resolution (~1 m), we favor the commercial IKONOS imagery for the outlining, which is, however, only available to us for Alaska National Parks (Figure 2.1a, Loso et al., 2014). Outside the National Parks, we rely mostly on orthorectified Landsat 5 and Landsat 7 imagery (Level L1G), freely available through the U.S. Geological Survey (USGS) Earth Explorer website (http://earthexplorer.usgs.gov, access: 25 August 2013). For selected areas (Aleutians, Coast Range, Alexander Archipelago), we complement Landsat with orthorectified ASTER imagery (Level 14OTH), provided through the USGS GLOVIS website (http://glovis.usgs.gov, access: 25 August 2013). For the Canadian part of the St. Elias Range, we rely partially on orthorectified SPOT 4 and SPOT 5 imagery, downloaded from National Resources Canada's website GeoGratis (http://www.geogratis.gc.ca; access: 25 August 2013).

Prior to the digitization, the IKONOS images (geocoded, pansharpened true-color composites) are orthorectified using their rational polynomial coefficients (RPCs) and the Digital Elevation Model (DEM) of the area covered. The already orthorectified Landsat data is combined into true- and false-color composites using the TM/ETM+ bands 3, 2, 1 (R,G,B), 5, 4, 3 (SWIR,NIR,R) or 4,

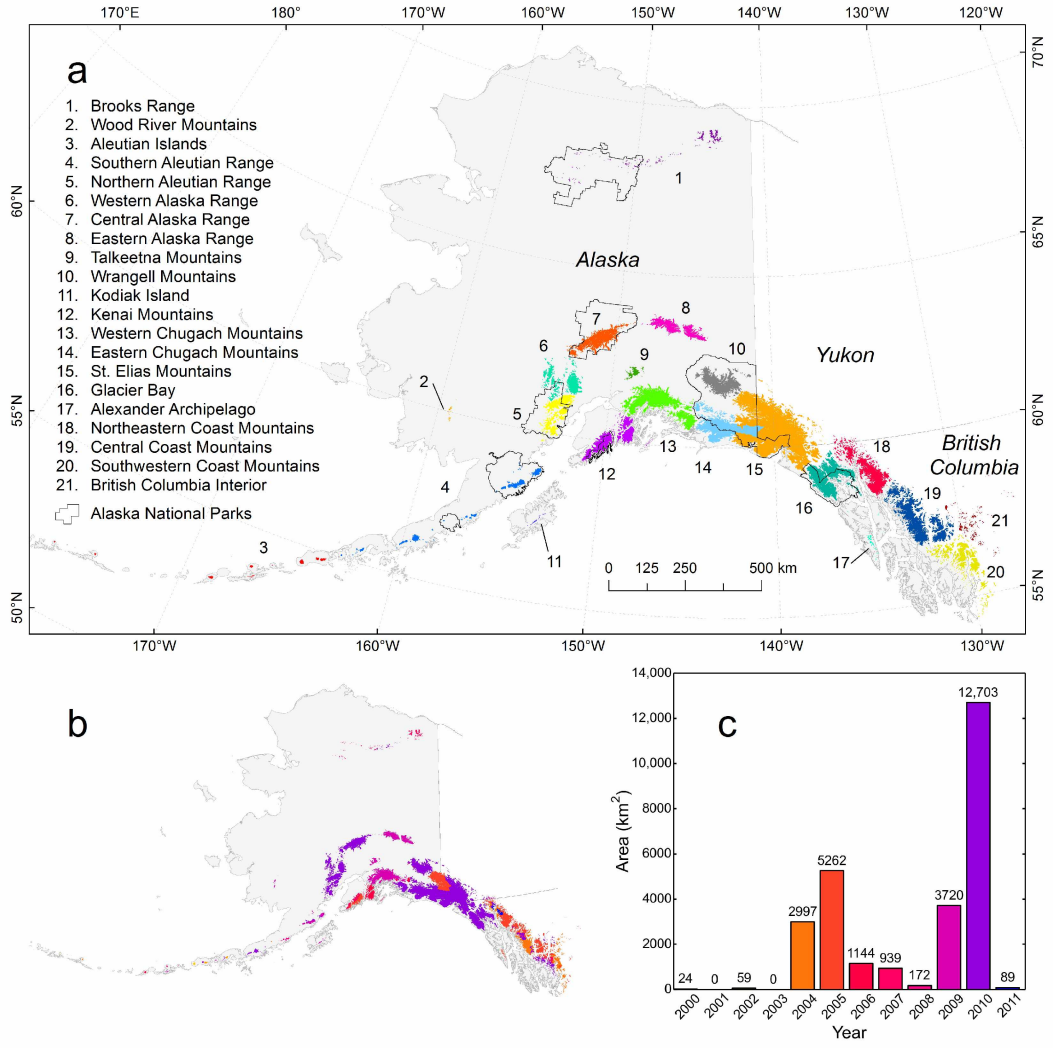

Figure 2.1: a) The 21 inventoried glacier regions, covering territory in Alaska, Yukon and British Columbia. b) Map and c) bar chart illustrating the area of glaciers inventoried for each year.

Table 2.1: Properties of the used satellite imagery. R = red, G = green, B = blue, NIR = near infrared, SWIR = shortwave infrared, pan = panchromatic.

Sensor	Channels used	Spatial resolution	Swath width
		m	km
IKONOS	RGB, pan.	0.8 (pan), 3.2 (color)	11
Landsat 5 TM	RGB, NIR, SWIR	30	185
Landsat 7 ETM+	RGB, NIR, SWIR, pan.	15 (pan), 30 (color)	185
Terra ASTER	NIR, R, G	15	60
SPOT 4/SPOT 5	Pan	10	60

3, 2 (NIR,R,G). In the case of Landsat 7, we use the panchromatic band 8 to create pansharpened 15 m color composites. The orthorectified ASTER data is processed into false-color (NIR,R,G) composites and in the case of SPOT 4/5, we use the 10 m panchromatic orthoimagery as downloaded from the GeoGratis website.

2.4.2 DEM

We use a multi-source DEM consistent with the time-span of our inventory (Figure 2.2a). This DEM, compiled by Kienholz et al. (2014), is based on four different DEM products: a DEM derived from airborne Interferometric Synthetic Aperture Radar (IFSAR), the Shuttle Radar Topography Mission (SRTM) DEM, SPOT DEMs, and the global ASTER DEM version 2 (ASTER GDEM2). Both the IFSAR and the SRTM DEM are interferometrically derived from radar data; the IFSAR DEM from airborne X-band data obtained in summer 2010 (http://ifsar.gina.alaska.edu, access: 10 December 2013), and the SRTM DEM from spaceborne C-band data obtained in February 2000 (Farr et al., 2007). The SPOT DEM and the ASTER GDEM2 are based on photogrammetric analysis of stereo imagery from the HRS instrument onboard the SPOT satellite (Korona et al., 2009) and the ASTER instrument onboard the Terra satellite (Tachikawa et al., 2011). Based on previous quality assessments (e.g., Frey and Paul, 2012) and our own inspections, we prefer the radar-derived DEMs over those derived from optical imagery. In the case of overlapping SPOT and ASTER DEMs, preference is given to the SPOT DEM. While the DEM quality is good overall, it can be poor in areas where both the underlying SPOT and GDEM contain blunders (e.g., due to clouds). In total, 14% of the glacierized area is covered by the IFSAR DEM, 36% by the SRTM, 28% by SPOT, and 22% by the ASTER GDEM (Figure 2.2a).

2.4.3 Velocity fields

We use remote sensing derived glacier velocity fields to map glacier divides. The velocity fields are derived using offset tracking and ALOS-PALSAR synthetic aperture radar data acquired between 2007 and 2011 (Burgess et al., 2013), consistent with the time range of our inventory. The ALOS data covers ~75% of the glacierized area (Figure 2.2b). As measured velocity fields are spatially discontinuous (e.g., due to decorrelation in the imagery used), the actual coverage is ~50% of the glacierized area. Regions without coverage include the Brooks Range, the Aleutian Islands, and the southern part of the Coast Mountains. To facilitate the mapping of the glacier divides, the initial velocity vectors are converted into streamlines, a set of lines tangent to the glacier velocity vectors.

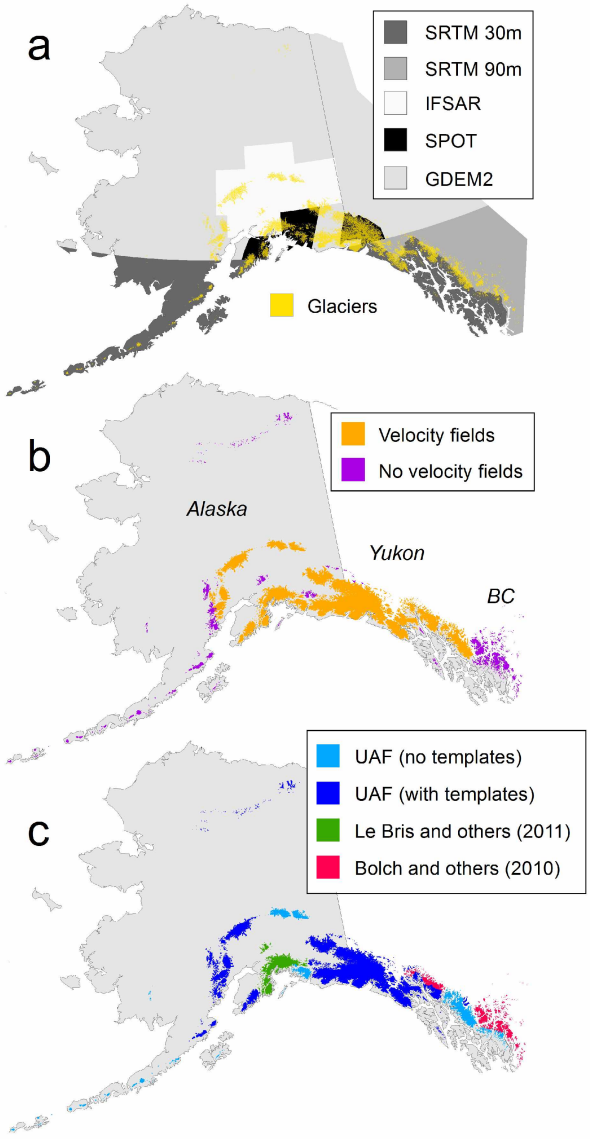

Figure 2.2: a) DEM sources with glaciers in yellow b) Coverage of velocity fields used for mapping ice divides c) Outline sources. Note that the digitization of the UAF outlines was often guided by existing outlines used as templates. The extents of the Bolch et al. (2010) and Le Bris et al. (2011) outlines show where we used their outlines without or with only minor changes.

2.4.4 Outlines from previous studies

This study directly incorporates outlines from two previous studies, available through the GLIMS database (Raup et al., 2007). The outlines provided by Bolch et al. (2010) cover ~30,000 km^2 in British Columbia and Alberta, ~18,000 km^2 of which is in our study area; those of Le Bris et al. (2011) cover ~16,000 km^2 in western Alaska and lie completely within our study area. Both studies rely on Landsat imagery and employ R/SWIR band ratioing (red vs. shortwave infrared, TM3/TM5) with manual threshold selection to obtain initial glacier complexes. Le Bris et al. (2011) use an additional blue threshold (TM1) to improve the results in areas with cast shadows. Filtering is employed to remove isolated misclassified debris cells surrounded by glacier ice. Debris-covered ice, water bodies, and perennial snow are improved manually after the automated steps.

2.5 Methods

2.5.1 Glacier outlines

Because clouds, debris cover, and perennial snow are common in Alaska, our 'UAF outlines' (i.e., outlines other than those adopted from Bolch et al. (2010) and Le Bris et al. (2011), Figure 2.2c), are not directly based on automated classification algorithms. We often use available ice outlines as templates and modify them manually based on the best available satellite imagery. Our template outlines in Alaska are primarily from 1:63,360 USGS maps compiled between the late 1940s and the 1970s. In the Yukon, they stem from the 1:50,000 National Topographic Data Base, mainly reflecting the 1980s. Digital versions of these outlines are provided by Berthier et al. (2010), B. Manley (unpublished data) or downloaded from the corresponding websites (http://earthexplorer.usgs.gov, ftp://ftp2.cits.rncan.gc.ca). In some areas (e.g., Eastern Alaska Range, parts of the Coast Mountains, Figure 2.2c), we digitize the glacier complexes from satellite imagery without using template outlines.

The manual editing is guided by GLIMS standards (Raup and Khalsa, 2007). Importantly, we consider debris-covered ice as part of the glacierized area unless it is clearly detached from the main glacier. As debris-covered ice is challenging to delineate, we often consult additional data, including imagery from other dates (having different shading) as well as contours and shaded relief maps derived from the DEM (facilitating the interpretation of landforms). Such an approach helps to improve the quality of the outlines, but does not guarantee full consistency or even the correct solution. The analysis of radar interferograms has shown potential for the derivation of debris covered glacier areas (Atwood et al., 2010; Frey et al., 2012). However, these methods require extensive processing of proprietary radar imagery, preventing their application in this study.

Following the digitization, we subdivide the glacier complexes into individual glaciers, using the algorithm described in Kienholz et al. (2013). This algorithm splits glaciers along watershed boundaries which approximate flow divides provided the DEM is accurate. Glacier complexes that drain into multiple termini are treated as separate glaciers, even if historically they have been treated as one glacier. This facilitates their allocation to individual watersheds (the termini may reach into different watersheds), the assignment of glacier type variable (e.g., one terminus may be land-terminating while the other may be lake-terminating) and the application of centerline algorithms. Some glacier complexes are manually split into multiple glaciers even if they drain into one common terminus. This occurs, for example, if the dynamic interaction is minimal (e.g., if there is a large area of stagnant, debris-covered ice between the glaciers) or if the glaciers show different dynamic behavior (e.g., surging and non-surging). Studies requiring fewer partitions between glaciers (e.g., regional mass balance extrapolations) can be accommodated by merging glacier polygons.

2.5.2 Combination of outline sources

There is ~20% overlap between outlines compiled at UAF and those obtained by Bolch et al. (2010) and Le Bris et al. (2011), in which case we here give preference to the UAF outlines. After combining the outline sources (Figure 2.2c), we check the glacier divides visually using streamlines derived from the ALOS-PALSAR velocity fields. Streamlines approximate the 2-D projections of ice trajectories, which facilitates large-scale visual checks (Figure 2.3a). While checking the divides, we also check for remaining blunders (e.g., perennial snow misclassified as glaciers, misclassified debris-covered areas) and make manual adjustments if necessary. Finally, we apply a minimum threshold of 0.025 km^2 throughout the inventory.

2.5.3 Centerlines

Automatic generation of glacier centerlines provides a consistent means for determining location and length of glacier branches. This data is utilized for conducting length change assessments (e.g., Winsvold et al., 2014), planning airborne monitoring programs (e.g., snow radar; McGrath et al., 2013), and objectively measuring branch topology (e.g., Sevestre et al., 2013). For each glacier > 0.1 km^2, we calculate centerlines semi-automatically, using a cost grid–least-cost route approach (Kienholz et al., 2014). This approach identifies centerlines between glacier heads and termini by calculating least-cost routes on a cost grid with highest values along glacier boundaries and in higher glacier reaches. In an additional step, the initial centerlines are split into centerlines that cover individual branches only. While we largely follow the steps in Kienholz et al. (2014), we

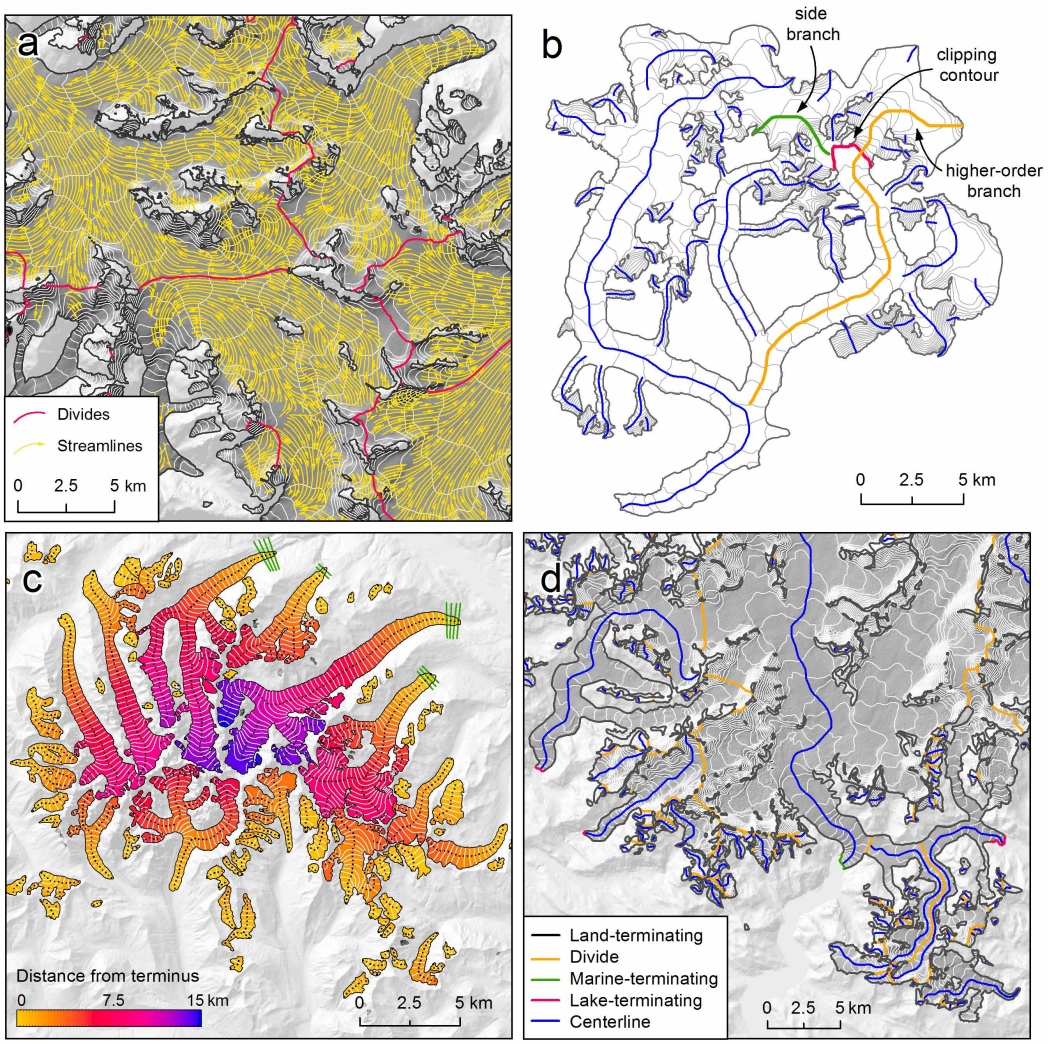

Figure 2.3: a) Streamlines and glacier divides overlaid on glaciers of the Juneau Icefield area (Coast Mountains). White lines correspond to 50 m contours derived from the SRTM DEM. b) Illustration of the approach to split the centerlines into individual branches. The clipping contour (shown in red) is the last contiguous contour between the higher-order branch (orange) and its side branches (one shown in green). The side branches are cut along the clipping contour, and only the part in contact with the glacier head is retained. c) Interpolated distance grid for selected glaciers of the Central Alaska Range. The color-coded grid and the white 250 m contours indicate the approximate distance of each glacier's grid cell to its terminus. The black dots illustrate the evenly spaced points along the centerlines used to interpolate the distance grid through spline interpolation. The green lines are the cross-profiles that are used to support the spline interpolation in the terminus area. d) Outline types and centerlines derived for a subset of the Coast Mountains.

apply a different method to derive the final centerlines, as illustrated in Figure 2.3b. Kienholz et al. (2014) use one area-dependent buffer distance per glacier to split the centerlines, which does not account for the different branch widths typically occurring on a glacier (see their step 3). Here, we define the centerline extent in the sense that centerlines end as they reach an elevation band in continuous contact with the next higher-order branch. In practice, we split the centerlines along the uppermost continuous elevation contour between the centerline and the connected higher-order branch. This contour is selected from a set of 5 m contours calculated for each glacier.

2.5.4 Derived variables

To quantify a wide range of glacier properties, we acquire a comprehensive set of inventory variables. Table 2.2 presents the full list of derived variables, while the following sections focus on the derivation of some key variables.

2.5.4.1 Distance grid and area-length distribution

Many glacier observations (e.g., surface velocities; Burgess et al., 2012) are best expressed with distance along flow as the independent variable. While centerlines provide this information for one-dimensional applications (i.e., along approximated flowlines), higher-dimensional applications (e.g., distributed modeling of debris cover, automated determination of glacier length changes) may benefit from a fully distributed distance grid. We here derive a distance grid for each glacier using the distance information conveyed by our centerlines. In an initial step, we sample the centerlines (100 m sampling distance) to obtain distance information at discrete points. We then fit a continuous surface through these points by applying a spline interpolation (Franke, 1982). By using glacier outlines as interpolation boundaries, we prevent interpolation across branches. To improve the interpolated surface in the terminus area, we add additional points along cross-profiles, with the same distance information as the point on the centerline (Figure 2.3c). To calculate the area-length distributions, we adopt two approaches: non-normalized and normalized regarding length (Table 2.2).

Table 2.2: List of derived inventory variables. The climate data is derived from the PRISM dataset (Daly et al., 1994).

Category	Attribute (unit)	Description
Identifiers	GLIMSID	Provisional GLIMS ID based on glacier latitude and longitude.
	RGIID	RGI ID (unique within each RGI version).
Region	01Region	RGI first-order region (one region).
	02Region	RGI second-order region (six regions).
	03Region	UAF inventory subregion (21 regions).
Date	BgnDate (YYYYMMDD)	Date of outline.
Name	Name	Name of glacier.
Location	CenLon, CenLat (°)	Longitude and Latitude of glacier centroid (WGS84).
	X, Y (m)	X and Y coordinates of glacier centroid (Alaska Albers).
	Xterm, Yterm (m)	X and Y coordinates of glacier terminus (Alaska Albers).
	Wtrsh (AABBCCDDEE)	USGS watershed identifier (Region, Subregion, Basin, Sub-basin, Watershed).
	DistCoast (km)	Minimum distance from the glacier centroid to the coastline.
	DistPoint (km)	Distance from the glacier centroid to a fixed point in the Gulf of Alaska.
Area	AreaTot (km^2)	Planar glacier area.
Area-altitude distribution	ElevArea0_50, ..., ElevArea6150_6200 (m^2)	Area per 50 m elevation bin between sea level and 6200 m.
	ElevMin, Elev5, Elev10, ..., ElevMax (m a.s.l.)	Elevation at which cumulative area, starting at lowest elevation, reaches given percentage of AreaTot. 5% area thresholds.
	SkewAAD	Skewness of the normalized area-altitude distribution.

Continued on next page

Table 2.2 – continued from previous page

Category	Attribute (unit)	Description
	ElevMean	Area-averaged elevation.
Area-length distribution	ElevLen0_250, ..., ElevLen199750_200000 (m^2)	Area per 250 m length bin between 0 and 200 km. (measured from terminus).
	LenMin, Len5, Len10, ..., LenMax (m)	Length at which cumulative area, starting at the terminus, reaches given percentage of AreaTot. 5% length thresholds.
Slope	SlopeTot (°)	Average slope of total glacier area (AreaTot).
	SlopeTerm (°)	Average slope of terminus area (lowest 10% of glacier area).
	SlopeMed (°)	Average slope of area between Elev45 and Elev55.
	Slope5, Slope10, ..., Slope100 (°)	Average slope per 5% of cumulative area (starting at terminus)
	SlopeLine (°)	Average slope along the main centerline.
	SlopeLine10, ..., SlopeLine100 (°)	Average slope per 10% length of the main centerline.
Aspect	AspectTot (° from North)	Average aspect of the entire glacier area.
	AspectB50 (° from North)	Average aspect below median elevation.
	AspectA50 (° from North)	Average aspect above median elevation.
	AspectLine (° from North)	Average aspect along the main centerline.
	AspectLine10, ..., AspectLine100 (°)	Average aspect per 10% length of the main centerline.
Length	LengthMax (m)	Length of the longest centerline.
	LengthTot (m)	Cumulative length of all centerlines.
Shape	LenPeri (m)	Length of glacier outline.
	Compactn	Compactness ratio. Perimeter of a circle with area corresponding to the glacier area, divided by the actual perimeter length of the glacier.

Continued on next page

Table 2.2 – continued from previous page

Category	Attribute (unit)	Description
Branch number	BraNum0_5, BraNum5_10, ..., BraNum95_100	Branch numbers of 5% length bins. LengthMax is the 100% reference length.
	BraCu5, BraCu10, ..., BraCu100	Branch number at which the cumulative branch length reaches given percentage of LengthTot (branches are sorted by length, starting with the longest branch). 5% steps, starting at 5% of LengthTot.
Glacier type	GlacType	Marine-terminating, lake-terminating or land-terminating.
Margin type	LenTdw (m)	Length of tidewater margin.
	LenLake (m)	Length of lake/river-terminating margin.
	LenLand (m)	Length of land-terminating margin.
	LenDiv (m)	Length of divides.
	LenDeb (m)	Length of land-terminating margins enclosing debris.
Debris	DebrisArea (km^2)	Debris cover in km^2.
	DebrisFract (%)	Debris cover in percent of the total glacier area.
	DebArea0_50, ..., DebArea6150_6200 (m^2)	Debris cover per 50 m elevation bin.
	Debris5, Debris10, ..., Debris100 (%)	Debris cover per 5% of the cumulative area.
Climatology	PreciSuMed (mm·100/month)	Mean monthly summer precipitation (May-September) at median elevation.
	PreciWiMed (mm·100/month)	Mean monthly winter precipitation (October-April) at median elevation.
	TempSuMed (°C·100)	Mean summer temperature at median elevation.
	TempWiMed (°C·100)	Mean winter temperature at median elevation.

2.5.4.2 Slope and aspect

Glacier aspects and slopes are commonly examined as controls on glacier mass balance and dynamic adjustment (e.g., Huss, 2012; Anderson and Mackintosh, 2012; Geck et al., 2013). Spatial sampling strategies vary among studies, ranging from using glacier-averaged to localized values only. Here, we calculate glacier-averaged slopes and aspects according to Paul et al. (2009) and complement them with slopes and aspects averaged over the area above and below the median glacier elevation, which represent roughly the accumulation and ablation area. We also record the mean slopes per 5% hypsometry bin, which can be averaged to obtain slopes over larger hypsometry ranges (e.g., the mean slope of the glacier tongue, defined as the mean slope of the lowermost 10% in Huss, 2012). Finally, we calculate slopes and aspects along the entire glacier centerlines as well as for sub-segments that make up 10% of the total centerline length (see Supplementary Materials for the equations).

2.5.4.3 Debris

Maps of debris cover are a key requirement to assess the effect of debris cover on glacier mass balance (e.g., Reid and Brock, 2010; Anderson and Mackintosh, 2012), which is not currently well understood, at least on regional scales (e.g., Berthier et al., 2010; Kääb et al., 2012). We here use the Landsat 5 band ratio TM4/TM5 with a threshold of 1.8 to differentiate bare ice from debris covered ice (Paul et al., 2004). To address small, erroneous debris patches and misclassified supraglacial lakes, we apply two filters: one that removes area classified as debris-covered with a surface area < 5000 m^2 and a second one that fills holes within the debris-covered area that are $< 10{,}000$ m^2 in size. After applying the filters, we combine the debris layers from individual scenes into one Alaska-wide dataset. Areas of overlap between scenes are manually clipped, keeping the debris maps of higher quality and/or later date of satellite image acquisition. The combined map is checked visually, and remaining erroneous patches of debris (e.g., in clouded areas) are removed. The final grid is used to determine each glacier's overall debris cover, as well as the debris cover per 50 m and 5% bin of the area-altitude distribution. Debris maps are generated for nearly all of our study area, but due to cloud cover, they are only partially generated for the Brooks Range and Southern Aleutian Range. Some of the smaller regions (Wood River Mountains, Aleutian Islands, Kodiak Island, and Alexander Archipelago) lack coverage completely, however, making up only 0.6% of the total glacierized area.

2.5.4.4 Glacier type

Frontal ablation (i.e., mass loss predominantly by calving and subaqueous melting, Cogley et al., 2011) is a potentially large contributor to glacier mass loss. The identification of glaciers with frontal ablation is thus desirable, for example, to better accommodate the needs of mass balance studies (e.g., Arendt et al., 2006). We here distinguish land-, marine-, and lake/river-terminating glaciers based on our own visual inspection of optical satellite imagery and DEMs as well as previous work (Molnia, 2008; McNabb and Hock, 2014). For this study, a glacier is classified as marine-terminating if it reaches tidewater at the time of the used image. Glaciers ending on an outwash plain close to tidewater (e.g., Taku Glacier) are considered land-terminating even if they are subject to the tidewater glacier cycle (Meier and Post, 1987). A glacier is classified as lake-terminating if major parts of its terminus reach a proglacial lake or river or if the imagery suggests substantial calving through marginal lakes.

2.5.4.5 Margin type

In addition to the overall glacier type, we classify the actual glacier margins, which aids, for example, partitioning of mass balance components or the estimation of outline uncertainties. Aside from lake- and marine-terminating margins, we distinguish land-terminating margins and flow divides (Figure 2.3d). The flow divides are derived from the original glacier outlines through an automated five step workflow (Figure 2.B-1). The resulting lines are then manually updated with the lake- and marine-terminating boundaries as derived from the satellite imagery. We use the final product to determine the lengths of the four margin types for each glacier. By intersecting the land-terminating outlines with the debris layer, we roughly approximate the outlines enclosing debris, a quantity that is used to estimate the outline uncertainties. Compared to fluxgate estimates, our lake- and tidewater lengths will always be systematically longer, as our margins do not necessarily run perpendicular to the glacier flow direction.

2.5.4.6 Climatology

For each glacier, we derive a basic climatology, consisting of mean monthly summer (May–September) and winter (October–April) precipitation and temperature at the median glacier elevation, using the median elevation as a surrogate for the equilibrium line (Braithwaite and Raper, 2010). The climatologies are derived from the Parameter-elevation Relationships on Independent Slopes Model (PRISM) dataset, which applies an analytical climate-elevation regression to distribute station precipitations and temperatures over a regularly spaced grid (Daly et al., 1994). Here, we use monthly gridded datasets with a spatial resolution of 2000 m,

representing the time period 1971–2000. Despite its coarse spatial resolution and considerable uncertainties in areas without weather stations, this climatology provides first-order climate information that aids mass balance related studies (e.g., Braithwaite and Raper, 2007).

2.5.4.7 Watersheds

We allocate all glaciers in Alaska to > 500 glacierized USGS 5th-level watersheds that make up 26 basins in six regions (agdcftp.wr.usgs.gov/pub/projects/AWSHED; access: 25 April 2014). The implementation consists of a spatial query that pairs each glacier terminus with the watershed in which it lies. The glacierized portions of the watersheds are automatically updated to match the divides of our glaciers. These watersheds allow the quantification of the glacierized areas per watershed, which will allow a better assessment of runoff changes in the future.

2.6 Uncertainties

The following sections assess the uncertainties in the glacier outlines, the centerlines and the debris layer. For other variables, we assume typical uncertainties derived in previous work (e.g., Frey and Paul, 2012).

2.6.1 Outlines

2.6.1.1 Inaccuracies in the outlines

To assess outline inaccuracies, we first adopt the approach introduced by Pfeffer et al. (2014). Here, the error e (km^2) of each glacier is given as a function of the glacier area s (km^2),

$$e = k \cdot e_1 \cdot s^p \quad , \tag{2.1}$$

where p (0.7), e_1 (0.039), and k (3.0) are empirically derived exponents and coefficients based on previously published estimates of area measurement uncertainties (Pfeffer et al., 2014).

In addition, we employ an approach that is based directly on the length of the glacier margins, along which the outlining errors occur. This approach is adapted from previous work (e.g., Rivera et al., 2007; Krumwiede et al., 2014) with the error e (km^2) given by,

$$e = \sum_{i=1}^{I} l_i \cdot w_i \quad , \tag{2.2}$$

where l_i (km) is the length of the glacier margin of type i, and w_i (km) is the mismatch between the true outlines (generally unknown) and the digitized outlines for margin type i. For clean ice boundaries, we use a w of $\pm$15 m (Paul et al., 2013) while we increase the uncertainty to $\pm$150 m for outlines enclosing debris (Frey et al., 2012). For simplicity, we use the same uncertainties w_i for all satellite sensors. Also, we do not account for the fact that glacier margins resemble fractals, with lengths l_i varying with the degree of generalization applied. Finally, we recognize that the error from Equation 2.2 can deviate from the corresponding error obtained through margin buffering (suggested by Paul et al., 2013), however, with differences that tend to be relatively small for hand-digitized, smooth outlines.

Table 2.3: Area-errors for all Alaska glaciers based on Equations 2.1 and 2.2 and five assumptions regarding error correlation. Equation 2.1 is applied on the glacier complexes rather than individual glaciers, accounting for errors that sum to zero if both sides of the divide are included. Likewise, glacier divides (11,687 km, 5.8% of the margins) are excluded in the case of Equation 2.2.

Correlation scenario	Error estimates	
	Equation 2.1	Equation 2.2
	km^2 (%)	km^2 (%)
1 Errors fully correlated	2072 (2.4)	5183 (6.0)
2 Four independent regions	1353 (1.6)	3648 (4.2)
3 21 independent regions	579 (0.7)	1657 (1.9)
4 27,109 independent glaciers	–	203 (0.2)
5 ~200,000 indep. 1 km segments	–	12 (0.01)

Summing up the glacier-specific errors from Equations 2.1 and 2.2 across our study region assumes systematic (i.e., fully correlated) outlining errors. Over large scales, outlining errors are likely not fully correlated, thus at least partially averaging out, which is addressed statistically by combining the uncorrelated errors in quadrature. However, determining realistic region-wide errors is hampered by the difficulty of defining the spatial scales at which the errors become uncorrelated. Therefore, we present errors for all Alaska glaciers based on five potential error correlation scenarios (Table 2.3). Scenario 1 is most conservative, assuming fully correlated errors. Scenario 2 distinguishes four regions that have outlines from different imagery and techniques: UAF high resolution (i.e., IKONOS), UAF low resolution (mostly Landsat), outlines from Bolch et al. (2010), and from Le Bris et al. (2011). This scenario then assumes fully correlated errors within each region, but uncorrelated errors among the four regions. The progressively less conservative

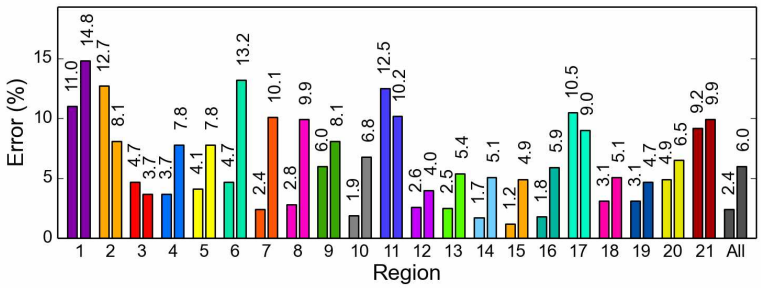

Figure 2.4: Percentage errors for the 21 subregions and all Alaska glaciers, using Equations 2.1 (with $k = 3$, bar on the left) and 2.2 (bar on the right).

scenarios 3, 4 and 5 treat the errors from the 21 inventory regions, the 27,109 glaciers and the ~200,000 one km outline segments as uncorrelated, respectively.

The spread in the resulting total errors is substantial, ranging from 0.01 to 6.0% of the total glacierized area. We here choose the most conservative scenario 1, recognizing that the final Alaska-wide errors might be lower. Figure 2.4 illustrates the corresponding errors for the 21 subregions and for all of Alaska.

2.6.1.2 Omission errors

Equations 2.1 and 2.2 include errors related to inaccurate mapping, but do not account for omission errors. To get a first-order estimate for such omission errors, we apply a downscaling approach introduced in Bahr and Radić (2012) and applied in Pfeffer et al. (2014), which suggests a power law size distribution down to the smallest glacier sizes. Assuming that the power law between the 0.125–0.25 and the 0.25–0.5 km^2 size classes applies to the smallest size class (here 1/128 km^2), we miss 1062 km^2 (1.2%) of ice area, made up by ~40,000 glacierets (Figure 2.5a). The fraction of missed area is higher for regions that comprise small glaciers only. In the case of the Brooks Range (largest glaciers < 10 km^2), the potentially missed glacier area corresponds to 11% of the currently inventoried area (Figure 2.5b, estimates for all regions are shown in Figure 2.B-2). Our power law (fitted between the 0.125–0.25 and the 0.25–0.5 km^2 size classes) is less steep than a power law fitted over larger size ranges (Figure 2.5). We choose this flatter power law by considering that all our cumulative curves level out towards smaller size classes (even in regions digitized from high-resolution IKONOS imagery), indicating that the power law obtained over larger size classes may not apply to smaller glacier classes.

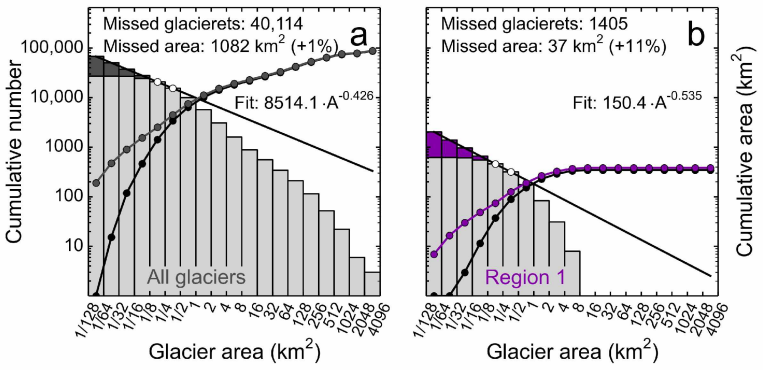

Figure 2.5: Missed glacierets for a) all Alaska and b) the Brooks Range glaciers, assuming the power law size distribution between the 0.125–0.25 and the 0.25–0.5 km^2 size classes down to the smallest size class. The light gray histogram shows the cumulative frequency distribution of glacier size while the dark gray/purple histogram indicates potentially missed glacierets. The black line shows the power law fit. Dotted lines show the cumulative glacier area with and without the potentially missed glacierets included.

2.6.1.3 Outline comparison

In addition to the above formal error estimates, we compare two sets of outlines in the Northern Aleutian Range region, which includes $>$ 1600 glaciers, both debris covered and largely debris free (Figure 2.B-3a). The first set of outlines, compiled by Le Bris et al. (2011), is derived semi-automatically from a 2007 Landsat scene. The second set uses these outlines as a template, but is manually adapted to match IKONOS imagery taken between 2006 and 2010. Both datasets have identical glacier divides so that area differences directly reflect differences in glacier outlining (which in turn depend on the interpretation of the GLIMS guidelines, the applied techniques (automated vs. manual), and the used imagery (high vs. low resolution)). While the IKONOS-derived outlines for the entire region make up 2878.5 km^2, the Landsat-derived outlines have an area that is 9.8% lower (2597.4 km^2). The IKONOS-derived outlines are systematically larger than the Landsat-derived outlines, with largest relative area differences for the smallest glaciers (Figures 2.6a; 2.B-3b). The absolute area differences increase with glacier outline lengths (Figure 2.6b). Dividing the area difference of 281.1 km^2 by the total IKONOS outline length (9008 km, excluding divides) yields an average systematic difference of 31.2 m along the entire perimeter. To distinguish between outlines enclosing clean ice (8349 km) and debris (659 km), we solve Equation 2.2, obtaining differences of 14.5 m and 237.6 m, respectively. Assuming both datasets contribute similar magnitudes to the total error (summed in quadrature, e.g., Williams et al., 1997), we obtain

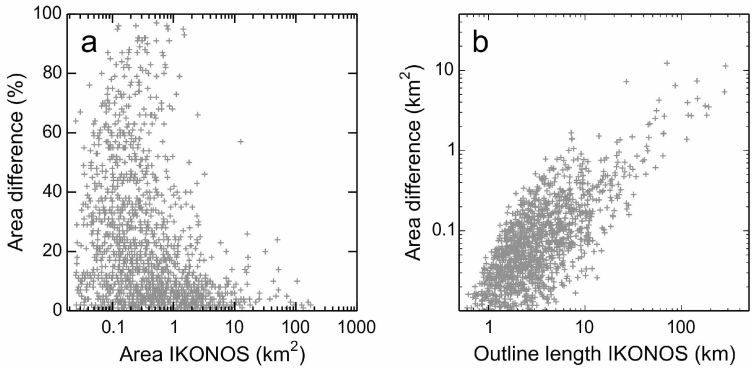

Figure 2.6: a) Relative area differences as a function of the IKONOS area. b) Absolute area difference as a function of the IKONOS outline length.

uncertainties of 10.25 m (clean ice) and 168 m (debris), in approximate agreement with w of ± 15 and ± 150 m used to assess our regional errors.

We note that the two compared datasets likely show two end member interpretations of the GLIMS guidelines, with conservative (Le Bris et al., 2011) and liberal (this study) inclusion of debris-covered sections. Unlike in previous studies (e.g., Bolch et al., 2010; Paul et al., 2013) the two compared datasets are also not fully independent (Landsat outlines are used as a template for the IKONOS outlines) and from imagery taken up to three years apart. Despite these constraints, this large-scale comparison highlights the difficulties associated with delineating debris covered ice and shows that ~10% area differences can be expected, even on a regional scale. This supports the choice of a conservative error correlation scenario for the regional error estimate (Table 2.3).

2.6.2 Centerlines

Machguth and Huss (2014) derived glacier lengths for Alaska using the same outlines and DEM as this study, but a different method. As part of the study, they compared the centerline lengths obtained from the two methods. For large glaciers (> 10 km^2), they find close agreement between the two approaches, with length errors less than 5%. Discrepancies increase towards smaller size classes, with potential length errors on the order of 20% for the smallest size class (0.1 to 0.5 km^2). We here adopt these numbers and express potential length errors e_l (km) as a continous function of the glacier area s (km^2) using the power law,

$$e_l = l \cdot c \cdot s^p, \tag{2.3}$$

where l is the glacier length (km), c = 0.1 and p = –0.3. Coefficient and exponent are chosen to obtain 20% length errors at 0.1 km^2 and 5% errors at 10 km^2 (resulting in 2.5% and 1.25% errors at 100 and 1000 km^2, respectively). This equation does not account for possible systematic differences which may occur towards smaller size classes, as indicated by Machguth and Huss (2014) (our lengths tending to be systematically longer than theirs). Also, it does not account for varying DEM quality, which can locally reduce the accuracy of the derived centerline lengths.

2.6.3 Debris

Based on visual inspections, we expect the debris percentages per glacier to be within 5% of the actual value, however, with uncertainties that can greatly increase towards smaller glaciers. Overall, the debris cover is likely underestimated for two main reasons. Seasonal snow in the used satellite imagery masks some of the debris if the snowline lies below the glacier equilibrium line. Also, clouded areas are masked out so that debris is missed in those areas. The applied filters have two opposing effects: they tend to reduce debris in areas with sparse debris cover, while increasing debris in areas where debris cover is dense. While these effects partially cancel out over larger regions, the number of glaciers with low debris percentages is biased negatively while the number of glaciers with high debris cover is biased positively.

2.7 Inventory characteristics

The following sections describe the main inventory characteristics and examine relationships among some of the derived variables. While this work aims at giving an overview, the derived data allows for more in-depth analyses in future studies.

2.7.1 Number, area, length

The Alaska glacier inventory (summarized in Table 2.4), comprises 27,109 glaciers (585 named) with a total area of 86,723 km^2. Glaciers make up ~ 3.5% of Alaska's total area, which is less than previously estimated (e.g., 5%, Molnia, 2008).

The largest contiguous ice mass in Alaska exceeds 30,000 km^2 in area, spanning parts of the St. Elias and Eastern Chugach Mountains and feeding the largest glaciers in our inventory (Figure 2.B-4): Seward Glacier (flowing into the Malaspina piedmont), Bering Glacier, and Hubbard Glacier. While Seward Glacier is largest, its 137 km length makes it second longest, behind Bering Glacier (197 km) and ahead of Hubbard Glacier (131 km). Combining glaciers with common termini into one glacier system, the Malaspina Glacier system is largest (4640 km^2), followed by the Bering Glacier system (4300 km^2). Unlike previous studies (e.g., Beedle et al., 2008), we here

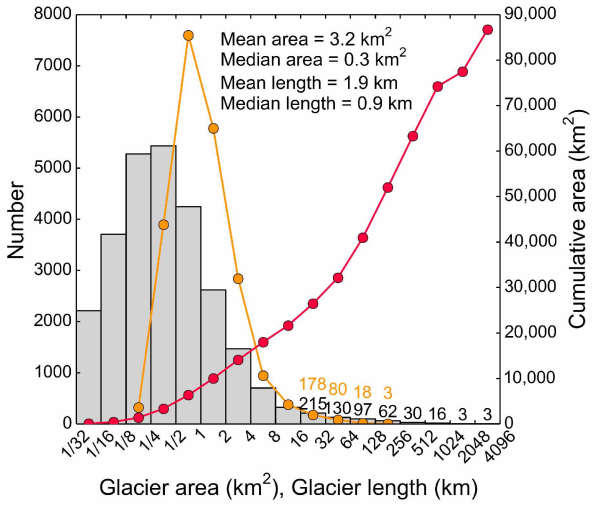

Figure 2.7: a) Frequency distributions of glacier area (histogram, left axis) and length (orange line, left axis). The cumulative glacier area (right axis) is shown in red.

distinguish Bering Glacier from the unnamed middle lobe of the Bering Glacier system due to its distinct surge dynamics (Burgess et al., 2012). This explains why Bering Glacier is largest in Beedle et al. (2008), while second-largest in our study.

On average, Alaska's glaciers have a length of 1.9 km and an area of 3.2 km^2. Both glacier area and length distributions are strongly left-skewed, yielding median values that are much lower than the means (0.9 km and 0.3 km^2, Figure 2.7). Glaciers smaller than the median area account for only 2.2% of the total glacierized area, while the three largest glacier systems (Malaspina, Bering and Hubbard) make up ~14% of the total glacier area.

2.7.1.1 Area-length relationship

Area and length typically have a log-log relationship (Bahr et al., 1997). Our analysis of this relationship yields slightly variable fits for the 21 study regions, with the Central Alaska Range (dominated by mountain glaciers) having the longest, and the Kenai Mountains (dominated by ice field outlet glaciers) having the shortest glaciers with respect to their area. Differences are most pronounced if considering only glaciers above a certain size threshold (e.g., 1 km^2 in Figure 2.8a). Our derived log-log relationship for all glaciers ($1.55 \cdot A^{0.647}$) is slightly steeper than the relationship $1.59 \cdot A^{0.606}$ of Machguth and Huss (2014), who used a different method for the derivation of the glacier lengths and a lower minimal size threshold. The two fits intersect at 1.85 km^2, with higher lengths of the Machguth and Huss (2014) approach below the intersection. In our case, one single log-log fit tends to overestimate the length of the largest glaciers. The

Table 2.4: Summary of the glacierized areas per region.

Region	Number of glaciers larger than				Area			Length[1]	
	0.025 km^2	1 km^2	10 km^2	100 km^2	Total km^2 (%)	Max. km^2	Mean km^2	Max. km	Mean km
01 Brooks Range	616	83	1	0	345.6 (0.4)	12.8	0.6	8.3	1.2
02 Wood River Mountains	81	9	0	0	36.9 (0.04)	6.5	0.5	4.7	0.9
03 Aleutian Islands	162	69	7	0	354.5 (0.41)	33.8	2.2	9.9	2.1
04 Southern Aleutian Range	625	210	34	0	1528.4 (1.76)	79.5	2.4	19.4	1.9
05 Northern Aleutian Range	1632	358	41	5	2878.5 (3.32)	173.2	1.8	42.1	1.6
06 Western Alaska Range	1328	244	23	4	2264.1 (2.61)	341.5	1.7	45.5	1.5
07 Central Alaska Range	994	188	31	8	3781.3 (4.36)	479.5	3.8	77.9	2.0
08 Eastern Alaska Range	837	183	37	5	2650.9 (3.06)	234.6	3.2	42.7	1.9
09 Talkeetna Mountains	279	58	7	0	346.6 (0.4)	56.1	1.2	14.7	1.6
10 Wrangell Mountains	994	268	50	9	4767.3 (5.5)	1028.8	4.8	84.6	2.2
11 Kodiak Island	85	4	0	0	29.5 (0.03)	3.5	0.3	3.8	0.7
12 Kenai Mountains	1525	299	65	8	4174.5 (4.81)	377.2	2.7	36.6	1.7
13 Western Chugach Mountains	2454	467	76	17	7530.8 (8.68)	773.9	3.1	56.1	1.9
14 Eastern Chugach Mountains	1340	251	27	9	7806.3 (9.0)	3025.1	5.8	196.8	2.0
15 St. Elias Mountains	3605	742	113	36	25266.6 (29.13)	3362.7	7.0	137.0	2.1
16 Glacier Bay	1721	360	66	19	6450.1 (7.44)	549.3	3.7	59.7	1.8
17 Alexander Archipelago	166	17	0	0	78.0 (0.09)	7.5	0.5	3.8	0.8
18 Northeastern Coast Mountains	2044	443	52	10	5116.4 (5.9)	521.4	2.5	59.9	1.6
19 Central Coast Mountains	3391	842	78	11	7716.8 (8.9)	612.7	2.3	57.4	1.5
20 Southwestern Coast Mountains	2625	506	46	3	3235.3 (3.73)	142.1	1.2	25.4	1.3
21 British Columbia Interior	605	80	3	0	364.3 (0.42)	14.1	0.6	7.7	1.0
Total	27109	5681	757	144	86722.7 (100)	3362.7	3.2	196.8	1.9

[1] Derived for glaciers > 0.1 km^2.

overestimation is reduced using two fits, here separated at 10 km^2 (Figure 2.8b). We note that length and average glacier width also correlate (Figure 2.8c). As expected, the correlation coefficients decrease towards smaller glaciers, where a wider range of glacier geometries exists.

2.7.2 Slope and aspect

Average slopes, measured along the main centerlines, range from ~1 to 50°, with largest glaciers having the lowest slopes (Figure 2.9a). A log-log fit between length and slope explains about 60% of the variability, with notable outliers. For example, Foraker Glacier in the Central Alaska Range is exceptionally steep for its length (10° at 24 km). Among the flattest glaciers are the 32 km long Yakutat Glacier and neighboring Novatak Glacier (38 km), with slopes of 1.5 and 1.8°, respectively. Both glaciers drain a low-lying, strongly receding coastal icefield (Trüssel et al., 2013) and their exceptionally low slopes may indicate their limited ability to adapt to climate warming. Figure 2.9a indicates region- and type-specific differences. For example, the glaciers of the Kenai Mountains tend to be flatter than glaciers in other regions. Also, marine-terminating glaciers tend to be steep compared to other glaciers, especially if they are short.

Glaciers have a characteristic slope distribution along their elevation profile (Figure 2.9b). Across three distinguished size classes, they are steepest in their highest reaches (90–100% of their elevation range) and flattest at ~20% of their elevation range. In the lower reaches of the three size classes, the average slopes vary between 5 and 20%, which is an indicator of the glaciers' ability to adapt their geometry to climate changes (e.g., Huss, 2012; Harrison, 2013). Low slope glaciers tend to adapt slowly, thus often having the most negative mass balances under warming conditions.

Northeastern to Northwestern aspects dominate the aspect range of the inventory, both in terms of area (area-aspect distribution in Figure 2.10) and glacier numbers (Figure 2.B-8). While N-S contrasts are subtle overall, they can be strong for individual regions. For example, the Brooks Range region has 80 km^2 in the N-oriented and only 10 km^2 in the S-oriented bin. This is likely due to the short-wave radiation that is strongly reduced in N-aspects at these high latitudes, and thus an important control on the glacier's mass balance in this continental climate. With its minimum area in W-NW aspects, the Aleutian Islands region has a notably different area-aspect distribution than the remaining regions, due to its unique location and topography (volcanic island chain).

2.7.2.1 Grid-derived vs. centerline-derived slopes and aspects

Slopes and aspects, traditionally derived along the main glacier centerline, are known to differ substantially from slopes and aspects derived from the full glacier grid. Figure 2.11a shows how our grid-derived slopes compare to the values derived along the main centerline, distinguishing

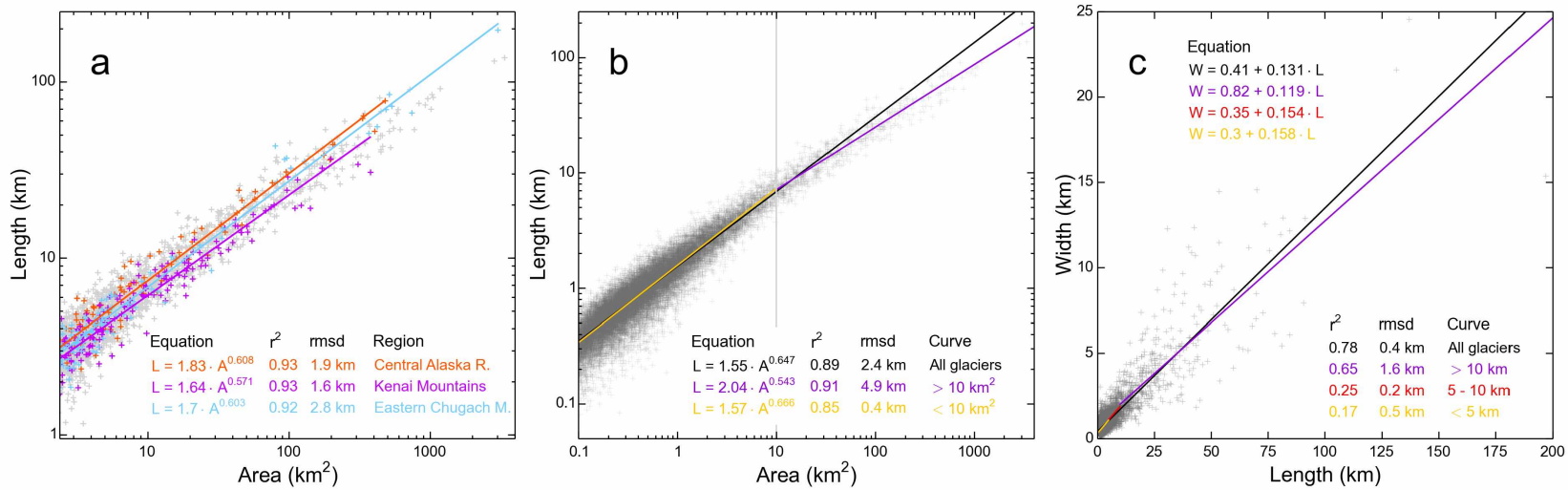

Figure 2.8: Relation between glacier area and length including best fit lines for a) three selected regions (crosses are grey unless part of the selected regions) and b) all glaciers (black line) as well as for two different size classes (orange and purple) separated at 10 km^2. c) Relation between length and average glacier width with best fit lines for three length classes separated at 5 and 10 km. All fits are highly significant ($p < 0.001$).

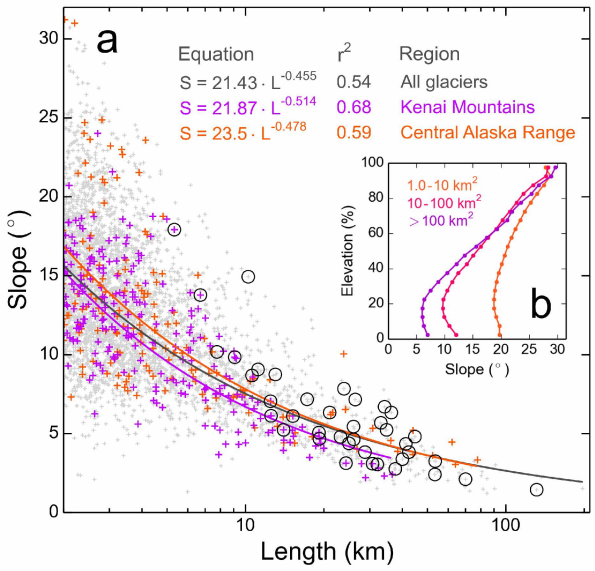

Figure 2.9: a) Glacier slopes measured along centerline as a function of length. Length is truncated at 3 km for better readability. Marine-terminating glaciers are marked with black circles. Log-log fits are given for selected regions, including r^2. Only the abscissa has a log-scale. The fits are highly significant ($p < 0.001$). b) Average grid-derived slopes per 5% elevation bin for three glacier size classes.

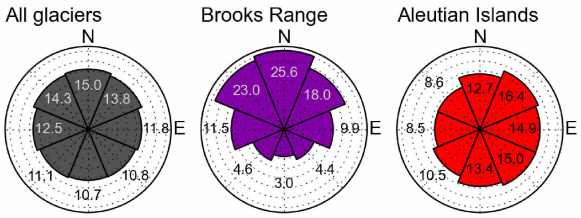

Figure 2.10: Area-aspect distribution for the entire study area and two subregions (Brooks Range, Aleutian Islands), using eight aspect bins normalized by area (areas summing up to 100%). Annotations give the area percentages per bin.

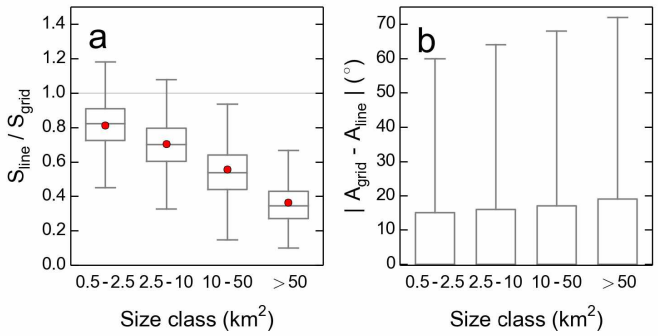

Figure 2.11: Agreement of grid- and centerline-derived slopes and aspects for four different size categories. a) Ratio of centerline- and grid-derived slopes (S). b) Absolute difference between the grid- and the line-derived aspects (A). The whiskers represent 1.5 times the interquartile range (IQR) and red points show the arithmetic means of the distribution. Outliers are not shown for improved readability.

four size classes. The differences between the two quantities increase towards larger size classes; for the size category > 10 km^2, more than half of the glaciers have grid-derived slopes at least twice as steep as the centerline-derived slopes. Figure 2.11b shows that more than half of the deviations in aspect are within 20° throughout the four size classes, with outliers that can be substantially higher. Discrepancies are greatest for the largest size class, where glaciers have many, often differently oriented side branches.

2.7.3 Area-altitude distribution

Glacier ice ranges in elevation from 6165 m (Mount McKinley, Central Alaska Range) to sea level, reached in seven regions (Figure 2.12). The regionally averaged median elevations extend from 975 m (Kodiak Island) to 2225 m (Wrangell Mountains). Regions containing large piedmont glaciers, or spanning multiple subregions of distinct topography and climate, tend to have secondary peaks and plateaus in their hypsometric curves. Overall, only 1960 glaciers (7.2%) span elevation differences greater than 1000 m, while smaller glaciers with limited elevation ranges are more abundant (Figure 2.12d). Median glacier elevation increases with distance from the coast (Figure 2.B-6a). Both the slope of the fit and the corresponding correlations are highest along the coast, leveling off towards the interior, hinting at strong coastal precipitation gradients. Figures 2.B-6b,c illustrate precipitation and temperature distributions for the 21 subregions, which are both inversely correlated with the median glacier elevations (Figure 2.12e).

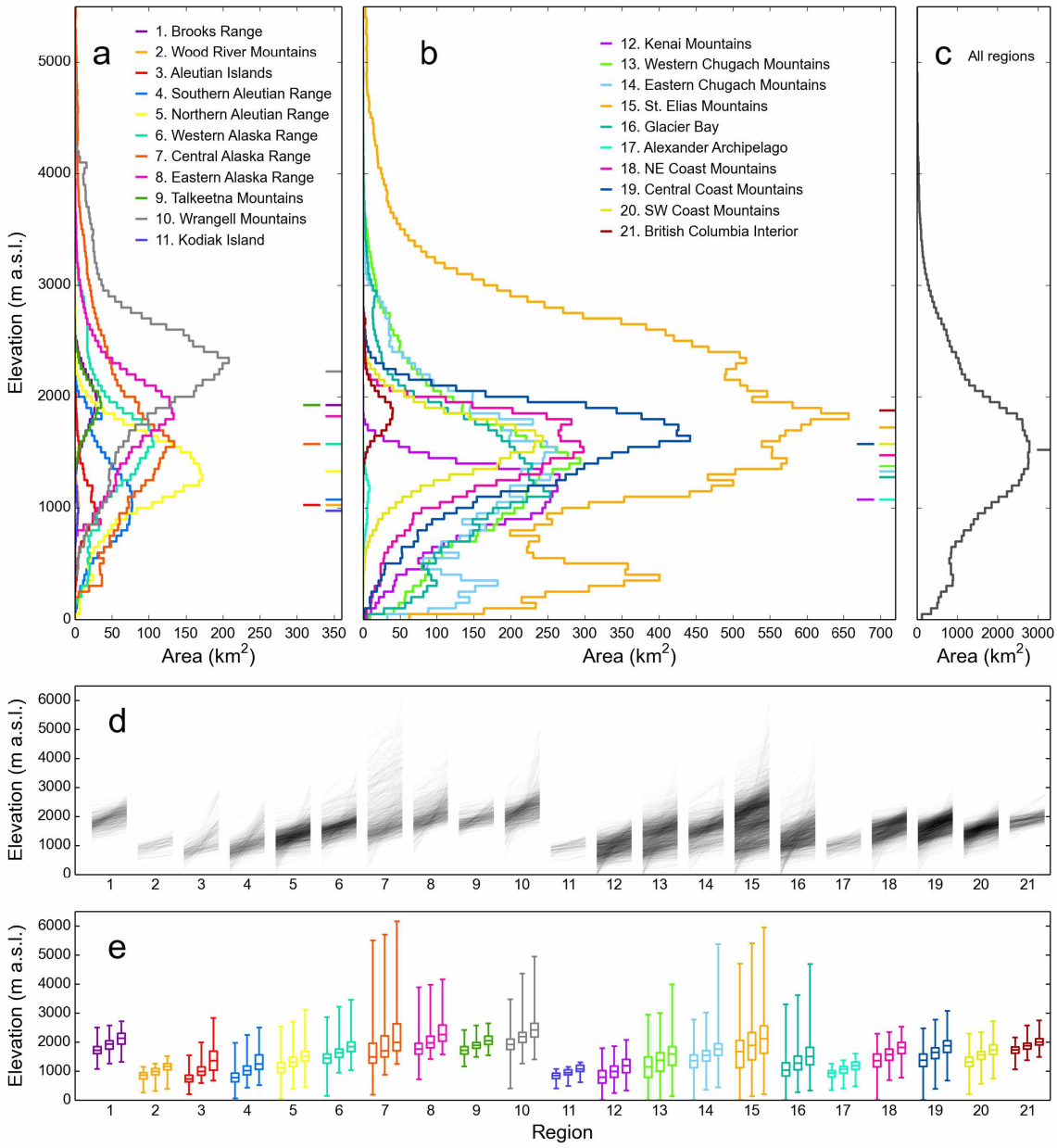

Figure 2.12: Hypsometries of the 21 regions. Glacier hypsometries in 50 m bins, per region (a,b) and for all regions combined (c). Horizontal ticks to the right side of the panel indicate the median elevations of each region. Note that the abscissae are the same in a) and b) but differ in c). d) Individual glacier hypsometries, with semi-transparent lines connecting the minimum (left), median (middle), and maximum elevations (right) for each glacier of the 21 regions. e) Summary of d) using three box plots per region, showing the distribution of minimum, median, and maximum glacier elevations. The whiskers represent the full elevation range.

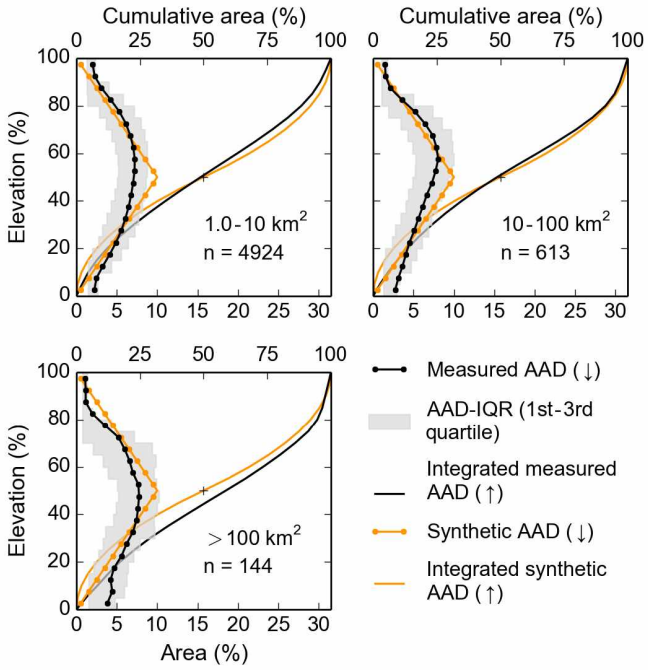

Figure 2.13: Normalized area-altitude distributions (AADs). Black dots reflect the average AAD per 5% elevation bin and gray shaded areas span between the first and third quartile of the corresponding distribution. The orange dots represent the synthetic mountain glacier AAD (s = 0, k = –0.6) according to Raper and Braithwaite (2006). Solid lines show the cumulative AAD for the two distributions. Arrows in the legend indicate whether the upper or lower axis is used.

2.7.3.1 Analysis of normalized hypsometries

Figure 2.13 illustrates the glacier hypsometries for three size classes, normalized by both area and elevation. The averaged hypsometries have parabolic shapes with area percentages increasing towards the midelevations before decreasing towards the termini. While the curve for the smallest size class (1–10 km^2) is symmetric, larger glaciers tend to have more area at their lowest elevations. At these low elevations, glaciers are flat (Figure 2.9b), indicating potentially high ice thicknesses and thus large ice volumes, which are vulnerable to loss given sustained glacier retreat.

Figure 2.B-7 illustrates the glacier hypsometries for 18 regions as well as the entire study region, including skewness and kurtosis to quantify the curves' shapes. Out of the 18 averaged curves, four have a skewness s close to zero (0 ± 0.05, indicating high symmetry), while seven curves each are top- ($s < -0.05$, i.e., median elevation > midelevation) and bottom-heavy ($s > 0.05$, median elevation < midelevation).

We investigate how Alaska's normalized hypsometries compare to the wedge-shaped synthetic hypsometry of Raper and Braithwaite (2006) previously used in mass balance

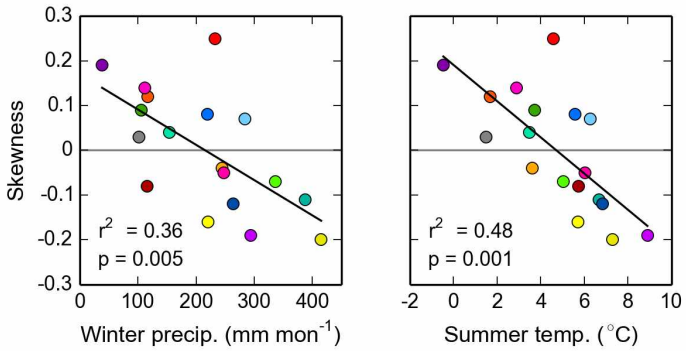

Figure 2.14: Linear fits between regionally averaged skewness, winter precipitation and summer temperature. The color-code is adopted from Figure 2.1. p indicates the significance level.

assessments, due to the lack of adequate glacier inventory data (e.g., Radić and Hock, 2011). Overall, we find that Alaska's glaciers match the wedge-shaped synthetic hypsometry well. Taken as input for mass balance assessments, our overall measured hypsometry would yield mass changes that are likely similar to the ones derived from the synthetic hypsometry, as the differences between the hypsometries even out: while the synthetic hypsometry underestimates the areas in both the lowest and highest reaches, it overestimates the areas above and below the midelevations. Having more area around the midelevations, however, glaciers with the synthetic hypsometry may be more susceptible to climatic changes. While the overall hypsometry matches the synthetic hypsometry of Raper and Braithwaite (2006) closely, this does not necessarily apply to individual regions or size classes. For the largest size class in Figure 2.13, the use of a synthetic hypsometry would bias the modeled mass balance results towards more positive values as it does not account for the excess area at the lowest elevations. We note that such comparisons always assume that the distributions use the same minimum and maximum elevations.

As the skewness of the normalized hypsometries varies across regions (Figure 2.B-7), we investigate how skewness compares to other regionally averaged glacier variables. We find that the symmetry of the averaged hypsometries correlates with the regionally averaged summer temperature at the median elevations as well as the corresponding winter precipitation (Figure 2.14), suggesting that glaciers in a more maritime setting might be more top-heavy than glaciers in a continental setting. Rather than indicating direct causation, these correlations may be a proxy for the predominant topography in these climates (steep mountainous topography in the continental parts vs. smoother ice field topography in more coastal areas). We note no significant correlations with other regionally averaged parameters (e.g., debris cover, glacier area).

2.7.4 Glacier type and glacier margin type

We identify 39 marine-terminating glaciers across five regions and 148 lake- and river-terminating glaciers across 13 regions (Figure 2.15a, Table 2.C-1). The actual number of glaciers with lake-/river-termini is higher (159), but 11 of these glaciers are considered land- or marine-terminating overall.

With a total area of 10,372 km^2, marine-terminating glaciers drain 12.0% of the total glacierized area while lake-terminating glaciers (16,720 km^2) drain 19.3% of the total glacierized area. The total length of the identified tidewater margins is 74 km, with 27 glaciers having tidewater margins longer than 1 km (Figure 2.15a). Lake- and river-calving margins have a total length of 420 km. The three glaciers of the Bering Glacier system contribute 75 km (18%) of lake-terminating margin (Table 2.C-2).

Table 2.5 summarizes selected statistical parameters for the distinguished glacier types. It indicates, for example, that the lake-terminating glaciers' average distance from the coast is 31 km, substantially less than the 67 km for land-terminating glaciers. This difference is likely related to the high precipitation amounts along the coast, which have allowed glaciers to reach low-lying flat terrain. Flat terrain is particularly susceptible to overdeepened channels and thus lakes upon glacier retreat (e.g., Trüssel et al., 2013).

As expected for their truncated geometries, marine-terminating glaciers have low area percentages at their lowest elevations (Figure 2.16), which would be atypical for land-terminating glaciers of the same size. Related to the former observation, marine-terminating glaciers are steep close to their termini, having higher slopes in the lowest 20% of the elevation range than the lake-terminating counterparts. As a controlling factor on ice velocities, surface slopes may have partial control on the glaciers' dynamic mass losses. In agreement with observations, this would suggest lower dynamic losses for lake-terminating glaciers compared to marine-terminating glaciers.

2.7.5 Debris

Debris covers ~11% of the glacierized terrain in Alaska, with percentages that vary substantially among regions (Figure 2.15b). With 28%, region 7 (Central Alaska Range) has the highest debris cover, followed by regions 6 and 8 (Western and Eastern Alaska Range) with 24 and 22% debris cover each. With only 1.4%, the Kenai Mountains (region 12) have the lowest debris cover. The distinct differences are attributable to varying geology and glacier types. Ice fields stand out with little debris as their relatively continuous ice cover with few nunataks effectively suppresses extraglacial debris sources.

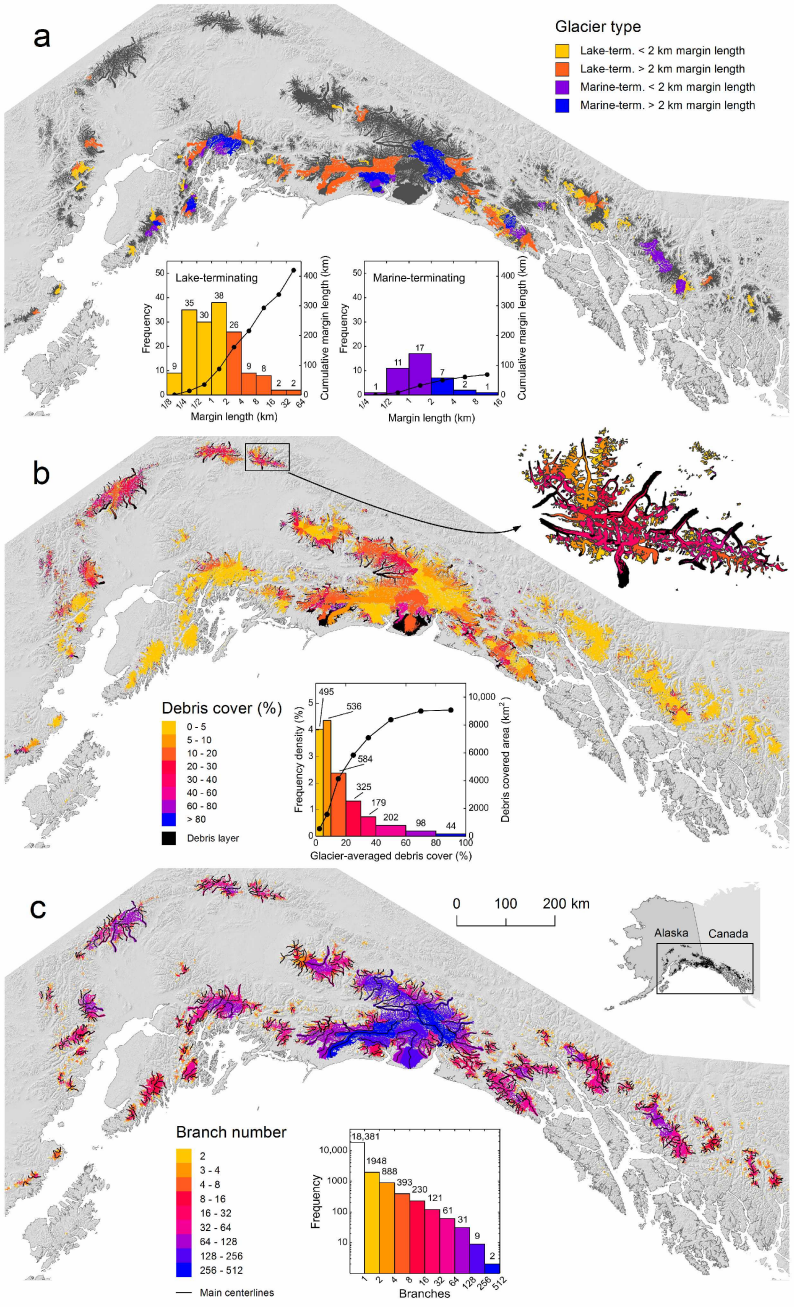

Figure 2.15: a) Marine- and lake-terminating glaciers, each separated in two length categories. The histograms give the numbers of glaciers per margin length bin (left axis) as well as the cumulative margin length (right axis). b) Glacier-averaged debris cover for southern Alaska, distinguishing eight classes of glacier-averaged debris cover. The inset map shows the glacier-averaged debris cover for the eastern part of the Eastern Alaska Range. The histogram gives the frequency density for each of the eight debris classes, with annotations of the actual numbers per debris class. c) Map and histogram with branch numbers. Centerlines are given for glaciers longer 10 km.

Table 2.5: Statistics for marine-, lake- and land-terminating glaciers. The given values are arithmetic means. Slope term refers to the slope of the lowest 10% of the glacier area.

Type	Area	Distance coast	Debris cover	Mean slope	Slope term	Min. elev.	Med. elev.	Max. elev.	Elev. range
	km^2	km	%	°	°	m a.s.l.	m a.s.l.	m a.s.l.	m a.s.l.
Marine	265.94	12	2	13.97	9.21	34	1319	2714	2680
Lake	112.98	31	12	14.21	8.50	346	1237	2193	1846
Land	2.17	67	17	24.09	22.99	1353	1575	1802	449

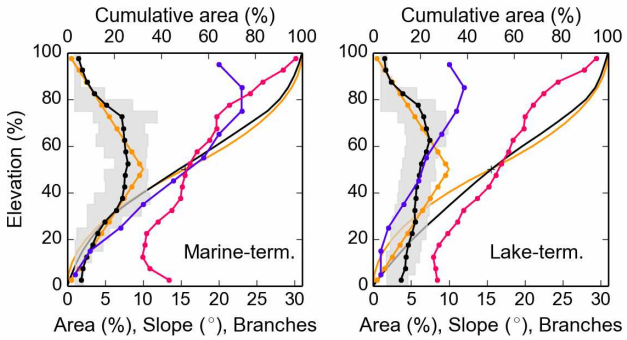

Figure 2.16: Normalized glacier area-altitude distributions (AADs) for marine- and lake-terminating glaciers. The black connected dots (lower abscissa) show the averaged AADs, distinguishing 5% elevation bins. The gray shaded area shows the interquartile range for each 5% bin. The orange dots represent the synthetic mountain glacier AAD (s = 0, k = –0.6) according to Raper and Braithwaite (2006). Solid lines (upper abscissa) show the cumulative AAD for the two distributions. The purple dots show the average slope per 5% elevation bin, while the blue dots show the branch number per 10% elevation bin.

The histogram in Figure 2.15b shows the number of glaciers for eight debris classes, considering the 2463 glaciers larger than 1 km^2 and with non-zero overall debris cover. Glaciers with little debris cover ($<$ 10%) are most abundant, while glaciers with higher debris cover are still common. We note that the decrease of glacier numbers from the 2.5–5% bin to the 0–2.5% bin is likely not real, but due to the applied filter (removal of debris patches $<$ 5000 m^2).

Debris shows a characteristic distribution along the glacier hypsometry, with shapes of the debris curves evolving from concave to convex as a function of the glacier-wide debris cover (Figure 2.17). As expected, the highest relative debris cover is found at lowest elevations, with a strong decrease towards higher elevations. Even in the case of $<$ 5% glacier-wide debris cover, the lowest 5% of the glacier area has a debris cover of 20%.

2.7.6 Branch numbers

Figure 2.15c shows the distribution of the branch numbers for the 22,064 glaciers $>$ 0.1 km^2 for which we calculated centerlines. 18,381 glaciers (83.3%) have one branch, while 3683 glaciers (16.7%) have at least two branches. The high branch numbers reached (up to 400, Hubbard Glacier) emphasize the high complexity of the glacier geometries found in our study area.

The number of branches correlates positively with glacier area. A linear fit explains up to 90% of the variability overall, if the largest glaciers ($>$ 1000 km^2) are omitted (Figure 2.18a), and ~80% of the variability if we include the largest glaciers. Our fits indicate differences in the area-branch

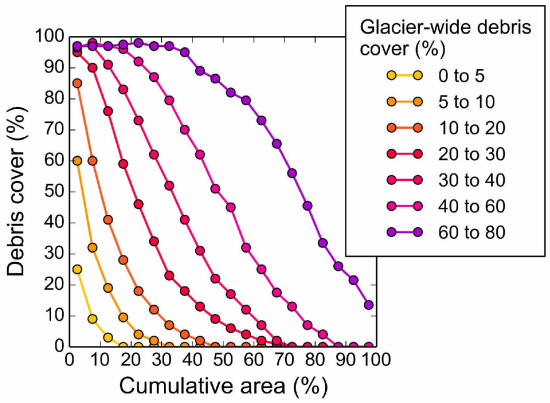

Figure 2.17: Percentage debris cover per 5% area bin for seven classes of glacier-wide debris cover. 0–5% of the cumulative area corresponds to the lowest 5% of the glacier.

relationship among the subregions: while glaciers in the Kenai Mountains (mostly icefield outlet glaciers) have ~14 branches at 100 km^2 size, glaciers (typically mountain glaciers) in the Eastern Alaska Range have 30.

Figure 2.18b illustrates the branch numbers as a function of the normalized elevation for four size classes. Small size classes contain only one branch throughout the elevation profile, while larger glaciers have multiple branches, with maximum numbers typically found at ~80 to 85% of the glacier elevation range (Figure 2.18b). Converging branches towards lower elevations leave one main branch left in the lowest elevation bin.

2.8 Conclusions

We have created a spatially complete, modern-date glacier inventory for Alaska and neighboring Canada, including > 50 derived variables across 17 main categories. Our new inventory contains 27,109 glaciers, covering 86,723 km^2 of ice (~12% of the global glacierized area, excluding ice sheets). Seward Glacier (3363 km^2 area and 137 km length, the main contributor to the Malaspina piedmont) and Bering Glacier (3025 km^2, 197 km) are the largest and longest glaciers. 39 marine-terminating glaciers make up 74 km of tidewater margin and drain 12.0% of the total glacierized area, while 148 lake- and river-terminating glaciers make up 420 km of lake-/river margin and drain 19.3% of the total glacierized area. For the first time, we have quantified both the length of tidewater and lake-/river margins in Alaska, providing useful input for quantifying mass losses at these margins in the future. Our new debris map shows an overall debris cover of 11%, with considerable differences among regions, ranging from 1.4% in the Kenai Mountains to 28% in the Central Alaska Range. Debris cover shows the expected distribution along glacier hypsometry, with highest relative debris cover at lower elevations and a strong decrease towards

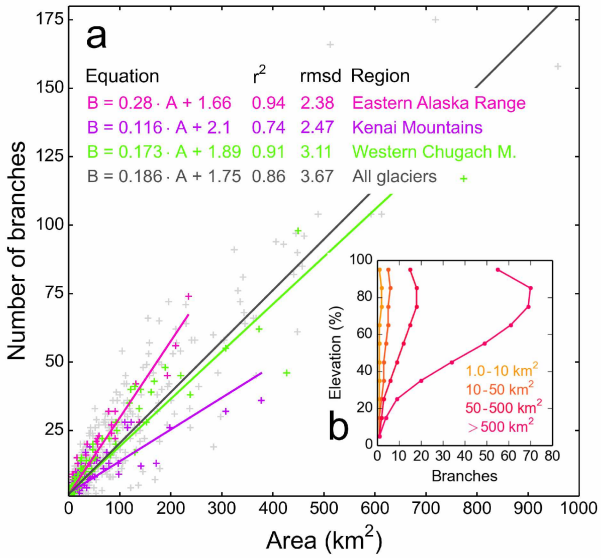

Figure 2.18: a) Correlation between glacier area and branch number. The colored lines show linear fits for selected regions. Only glaciers < 1000 km^2 are considered. All the fits are highly significant ($p < 0.001$). b) Average branch number per 10% elevation bin for four size classes.

higher elevations; the characteristic curve shapes vary as a function of the overall debris cover. The derived curves may aid future mass balance modelling applications.

Comparison between our area-altitude distributions and previously established synthetic hypsometries shows close agreement, corroborating results from previous mass balance studies; exceptions are larger glaciers (more bottom-heavy) and glaciers close to the coast (more top-heavy). A comparison of grid- and centerline-derived slopes and aspects shows that grid-derived slopes are higher, especially for large glaciers (> 10 km^2), where half of the grid-derived slopes are at least twice as steep as the line-derived slopes.

Deriving area-length scaling relations indicates that one single log-log fit tends to overestimate the length of the largest glaciers. The overestimation of length is reduced when using two fits, separated at 10 km^2 (resulting in a steeper fit for smaller glaciers and a flatter fit for larger glaciers). The fits are slightly variable for the 21 study regions with the Central Alaska Range (dominated by mountain glaciers) having the longest, and the Kenai Mountains (dominated by ice field outlet glaciers) having the shortest glaciers with respect to their area.

Comparing more than 1600 glacier outlines derived from IKONOS and Landsat imagery by different investigators yields a total area difference of $\sim$10%, emphasizing the great difficulties in accurately delineating debris-covered glaciers from optical satellite imagery. Our analysis suggests uncertainties of $\pm$10 m along clean ice and exceeding $\pm$150 m along debris covered margins, which is in approximate agreement with previous studies. Assuming fully correlated

errors yields errors of 6% for all Alaska glaciers, and up to 15% for individual subregions. These errors are larger than usually reported for regional scales, emphasizing the need for studies that quantify error correlation scales adequately. Applying a downscaling approach indicates that our inventory might miss a large number of glacierets ($>$ 40,000) due to the applied minimal area threshold of 0.025 km^2 and other omission errors. While the potential area contribution of these missed glacierets is small ($\sim$1% for all of Alaska), it could be substantial for individual regions (e.g., 11% for the Brooks Range).

The Alaska outline database is a major step forward, providing a spatially complete outline dataset including an large number of attributes that quantify a wide range of glacier properties. Several variables such as outline types, distance grids, and debris cover are new for a glacier inventory of this size. Further improvements to the inventory should focus on improved identification of debris covered glacier parts, for example aided by radar interferometry. Improved and temporally more consistent DEMs could further reduce uncertainties in the centerlines, the glacier divides, and the derived parameters. Additional attributes such as the classification of surge-type glaciers could make the database more complete in terms of variables. To accommodate future applications of the inventory, the glacier outlines are available from RGI version 4.0 onwards (http://www.glims.org/RGI/randolph.html).

2.9 Acknowledgements

Support for this work was provided by the National Aeronautics and Space Administration under the Cryosphere Sciences Program (grants NNH10Z1A001N, NNX11AF41G), by the National Science Foundation (grant EAR-0943742), and the National Park Service (grant H9911080028). The comments by B. Raup and R. Wheate improved the manuscript.

References

Anderson, B. and A. Mackintosh (2012). Controls on mass balance sensitivity of maritime glaciers in the Southern Alps, New Zealand: The role of debris cover. *Journal of Geophysical Research: Earth Surface 117*(F1).

Arendt, A., K. Echelmeyer, W. Harrison, C. Lingle, S. Zirnheld, V. Valentine, B. Ritchie, and M. Druckenmiller (2006). Updated estimates of glacier volume changes in the western Chugach Mountains, Alaska, and a comparison of regional extrapolation methods. *Journal of Geophysical Research 111*(F3), F03019.

Arendt, A. A., K. A. Echelmeyer, W. D. Harrison, C. S. Lingle, and V. B. Valentine (2002). Rapid wastage of Alaska glaciers and their contribution to rising sea level. *Science 297*(5580), 382–386.

Atwood, D. K., F. Meyer, and A. Arendt (2010). Using L-band SAR coherence to delineate glacier extent. *Canadian Journal of Remote Sensing 36*(sup1), 186–195.

Bahr, D. B., M. F. Meier, and S. D. Peckham (1997). The physical basis of glacier volume-area scaling. *Journal of Geophysical Research 102*(B9), 20355–20362.

Bahr, D. B. and V. Radić (2012). Significant contribution to total mass from very small glaciers. *The Cryosphere 6*(4), 763–770.

Barrand, N. E. and M. J. Sharp (2010). Sustained rapid shrinkage of Yukon glaciers since the 1957–1958 International Geophysical Year. *Geophysical Research Letters 37*(7).

Beedle, M. J., M. Dyurgerov, W. Tangborn, S. J. S. Khalsa, C. Helm, B. Raup, R. Armstrong, and R. Barry (2008). Improving estimation of glacier volume change: a GLIMS case study of Bering Glacier System, Alaska. *The Cryosphere 2*(1), 33–51.

Berthier, E., E. Schiefer, G. K. C. Clarke, B. Menounos, and F. Rémy (2010). Contribution of Alaskan glaciers to sea-level rise derived from satellite imagery. *Nature Geoscience 3*, 92–95.

Bieniek, P. A., U. S. Bhatt, R. L. Thoman, H. Angeloff, J. Partain, J. Papineau, F. Fritsch, E. Holloway, J. E. Walsh, C. Daly, M. Shulski, G. Hufford, D. Hill, S. Calos, and R. Gens (2012). Climate divisions for Alaska based on objective methods. *Journal of Applied Meteorology and Climatology 51*(7), 1276–1289.

Bliss, A., R. Hock, and V. Radić (2014). Global response of glacier runoff to twenty-first century climate change. *Journal of Geophysical Research: Earth Surface 119*(4), 717–730.

Bolch, T., B. Menounos, and R. Wheate (2010). Landsat-based inventory of glaciers in western canada, 1985-2005. *Remote Sensing of Environment 114*(1), 127–137.

Braithwaite, R. J. and S. C. B. Raper (2007). Glaciological conditions in seven contrasting regions estimated with the degree-day model. *Annals of Glaciology 46*, 297–302.

Braithwaite, R. J. and S. C. B. Raper (2010). Estimating equilibrium-line altitude (ELA) from glacier inventory data. *Annals of Glaciology 50*(53), 127–132.

Burgess, E. W., R. R. Forster, and C. F. Larsen (2013). Flow velocities of Alaskan glaciers. *Nature Communications 4*(2146).

Burgess, E. W., R. R. Forster, C. F. Larsen, and M. Braun (2012). Surge dynamics on Bering Glacier, Alaska, in 2008–2011. *The Cryosphere 6*(6), 1251–1262.

Cogley, J. G., R. Hock, L. A. Rasmussen, A. A. Arendt, R. J. Bauder, A.and Braithwaite, P. Jansson, G. Kaser, M. Möller, L. Nicholson, et al. (2011). Glossary of glacier mass balance and related terms. *IHP-VII Technical Documents in Hydrology 86*.

Daly, C., R. P. Neilson, and D. L. Phillips (1994). A Statistical-Topographic Model for Mapping Climatological Precipitation over Mountainous Terrain. *Journal of Applied Meteorology 33*(2), 140–158.

Farr, T. G., P. A. Rosen, E. Caro, R. Crippen, R. Duren, S. Hensley, M. Kobrick, M. Paller, E. Rodriguez, L. Roth, D. Seal, S. Shaffer, J. Shimada, J. Umland, M. Werner, M. Oskin, D. Burbank, and D. Alsdorf (2007). The Shuttle Radar Topography Mission. *Reviews of Geophysics 45*(2), 1–33.

Field, W. O. (Ed.) (1975). *Mountain Glaciers of the Northern Hemisphere*. Cold Regions Research and Engineering Laboratory, Hanover, 2 Vols & Atlas.

Franke, R. (1982). Smooth Interpolation of Scattered Data by Local Thin Plate Splines. *Computer and Mathematics with Applications 8*(4), 273–281.

Frey, H. and F. Paul (2012). On the suitability of the SRTM DEM and ASTER GDEM for the compilation of topographic parameters in glacier inventories. *International Journal of Applied Earth Observation and Geoinformation 18*, 480–490.

Frey, H., F. Paul, and T. Strozzi (2012). Compilation of a glacier inventory for the western Himalayas from satellite data: methods, challenges, and results. *Remote Sensing of Environment 124*, 832–843.

Geck, J., R. Hock, and M. Nolan (2013). Geodetic Mass Balance of Glaciers in the Central Brooks Range, Alaska, USA, from 1970 to 2001. *Arctic, Antarctic, and Alpine Research 45*(1), 29–38.

Harrison, W. D. (2013). How do glaciers respond to climate? Perspectives from the simplest models. *Journal of Glaciology 59*(217), 949–960.

Huss, M. (2012). Extrapolating glacier mass balance to the mountain-range scale: the European Alps 1900–2100. *The Cryosphere 6*, 713–727.

Kääb, A., E. Berthier, C. Nuth, J. Gardelle, and Y. Arnaud (2012). Contrasting patterns of early twenty-first-century glacier mass change in the Himalayas. *Nature 488*(7412), 495–498.

Kienholz, C., R. Hock, and A. A. Arendt (2013). A new semi-automatic approach for dividing glacier complexes into individual glaciers. *Journal of Glaciology 59*(217), 913–925.

Kienholz, C., J. L. Rich, A. A. Arendt, and R. Hock (2014). A new method for deriving glacier centerlines applied to glaciers in Alaska and northwest Canada. *The Cryosphere 8*(2), 503–519.

Korona, J., E. Berthier, M. Bernard, F. Rémy, and E. Thouvenot (2009). SPIRIT. SPOT 5 stereoscopic survey of Polar Ice: Reference Images and Topographies during the fourth International Polar Year (2007–2009). *ISPRS Journal of Photogrammetry and Remote Sensing 64*(2), 204–212.

Krumwiede, B. S., U. Kamp, G. J. Leonard, J. S. Kargel, A. Dashtseren, and M. Walther (2014). Recent glacier changes in the mongolian altai mountains: Case studies from munkh khairkhan and tavan bogd. In J. S. Kargel, G. J. Leonard, M. P. Bishop, A. Kääb, and B. H. Raup (Eds.), *Global Land Ice Measurements from Space*, Springer Praxis Books, pp. 481–508. Springer Berlin Heidelberg.

Larsen, C. F., R. J. Motyka, A. A. Arendt, K. A. Echelmeyer, and P. E. Geissler (2007). Glacier changes in southeast Alaska and northwest British Columbia and contribution to sea level rise. *Journal of Geophysical Research 112*, F01007.

Le Bris, R., F. Paul, H. Frey, and T. Bolch (2011). A new satellite-derived glacier inventory for Western Alaska. *Annals of Glaciology 52*(59), 135–143.

Loso, M., A. Arendt, C. F. Larsen, J. L. Rich, and N. Murphy (2014). Alaskan National Park Glaciers: Status and Trends. Technical report, National Park Service, Fort Collins, Colorado.

Machguth, H. and M. Huss (2014). The length of the world's glaciers–a new approach for the global calculation of center lines. *The Cryosphere 8*(5), 1741–1755.

Marzeion, B., A. H. Jarosch, and M. Hofer (2012). Past and future sea-level change from the surface mass balance of glaciers. *The Cryosphere 6*(6), 1295–1322.

McGrath, D., A. Gusmeroli, S. Oneel, L. C. Sass, A. A. Arendt, G. J. Wolken, C. Kienholz, and C. McNeil (2013). Comparison of annual accumulation rates derived from in situ and ground penetrating radar methods across Alaskan glaciers. *AGU Fall Meeting Abstracts*, B633.

McNabb, R. W. and R. Hock (2014). Alaska tidewater glacier terminus positions, 1948–2012. *Journal of Geophysical Research: Earth Surface 119*(2), 153–167.

Meier, M. F. and A. Post (1987). Fast tidewater glaciers. *Journal of Geophysical Research 92*(B9), 9051–9058.

Molnia, B. F. (2008). Glaciers of North America – Glaciers of Alaska. In R. S. William and J. G. Ferrigno (Eds.), *Satellite image atlas of glaciers of the world*. U.S. Geological Survey Professional Paper 1386-E, 525 pp.

Nuth, C., J. Kohler, M. König, A. von Deschwanden, J. O. Hagen, A. Kääb, G. Moholdt, and R. Pettersson (2013). Decadal changes from a multi-temporal glacier inventory of Svalbard. *The Cryosphere 7*(5), 1603–1621.

Paul, F., N. E. Barrand, S. Baumann, E. Berthier, T. Bolch, K. Casey, H. Frey, S. P. Joshi, V. Konovalov, R. Le Bris, N. Mölg, G. Nosenko, C. Nuth, A. Pope, A. Racoviteanu, P. Rastner, B. Raup, K. Scharrer, S. Steffen, and S. Winsvold (2013). On the accuracy of glacier outlines derived from remote-sensing data. *Annals of Glaciology 54*(63), 171–182.

Paul, F., R. G. Barry, J. G. Cogley, H. Frey, W. Haeberli, A. Ohmura, C. S. L. Ommanney, B. Raup, A. Rivera, and M. Zemp (2009). Recommendations for the compilation of glacier inventory data from digital sources. *Annals of Glaciology 50*(53), 119–126.

Paul, F., C. Huggel, and A. Kääb (2004). Combining satellite multispectral image data and a digital elevation model for mapping debris-covered glaciers. *Remote Sensing of Environment 89*(4), 510–518.

Pfeffer, W. T., A. A. Arendt, A. Bliss, T. Bolch, J. G. Cogley, A. S. Gardner, J. O. Hagen, R. Hock, G. Kaser, C. Kienholz, E. S. Miles, G. Moholdt, N. Mölg, F. Paul, V. Radić, P. Rastner, B. H. Raup, J. L. Rich, and M. J. Sharp (2014). The Randolph Glacier Inventory: a globally complete inventory of glaciers. *Journal of Glaciology 60*(221), 537–552.

Radić, V., A. Bliss, A. C. Beedlow, R. Hock, E. Miles, and J. G. Cogley (2014). Regional and global projections of twenty-first century glacier mass changes in response to climate scenarios from global climate models. *Climate Dynamics 42*(1), 37–58.

Radić, V. and R. Hock (2010). Regional and global volumes of glaciers derived from statistical upscaling of glacier inventory data. *Journal of Geophysical Research 115*, F01010.

Radić, V. and R. Hock (2011). Regionally differentiated contribution of mountain glaciers and ice caps to future sea-level rise. *Nature Geoscience 4*(2), 91–94.

Raper, S. C. B. and R. J. Braithwaite (2006). Low sea level rise projections from mountain glaciers and icecaps under global warming. *Nature 439*(7074), 311–313.

Raup, B., A. Kääb, J. S. Kargel, M. P. Bishop, G. Hamilton, E. Lee, F. Paul, F. Rau, D. Soltesz, S. J. S. Khalsa, M. Beedle, and C. Helm (2007). Remote sensing and GIS technology in the Global Land Ice Measurements from Space (GLIMS) Project. *Computers & Geosciences 33*(1), 104–125.

Raup, B. and S. J. S. Khalsa (2007). *GLIMS Analysis Tutorial*. GLIMS.

Reid, T. D. and B. W. Brock (2010). An energy-balance model for debris-covered glaciers including heat conduction through the debris layer. *Journal of Glaciology 56*(199), 903–916.

Rivera, A., T. Benham, G. Casassa, J. Bamber, and J. A. Dowdeswell (2007). Ice elevation and areal changes of glaciers from the Northern Patagonia Icefield, Chile. *Global and Planetary Change 59*(1), 126–137.

Schiefer, E., B. Menounos, and R. Wheate (2008). An inventory and morphometric analysis of British Columbia glaciers, Canada. *Journal of Glaciology 54*(186), 551–560.

Sevestre, H., D. Benn, and J. Hagen (2013). A Geodatabase on Surge-Type Glaciers: Behaviours, Trends and Clustering. *AGU Fall Meeting Abstracts*, A683.

Shulski, M. and G. Wendler (2007). *The climate of Alaska*. University of Alaska Press, Fairbanks, 216pp.

Tachikawa, T., M. Hato, M. Kaku, and A. Iwasaki (2011). Characteristics of aster gdem version 2. In *Geoscience and Remote Sensing Symposium (IGARSS), 2011 IEEE International*, pp. 3657–3660.

Trüssel, B. L., R. J. Motyka, M. Truffer, and C. F. Larsen (2013). Rapid thinning of lake-calving Yakutat Glacier and the collapse of the Yakutat Icefield, southeast Alaska, USA. *Journal of Glaciology 59*(213), 149–161.

Williams, R. S., D. K. Hall, O. Sigurdsson, and J. Y. L. Chien (1997). Comparison of satellite-derived with ground-based measurements of the fluctuations of the margins of Vatnajökull, Iceland, 1973-92. *Annals of Glaciology 24*, 72–80.

Winsvold, S. H., L. M. Andreassen, and C. Kienholz (2014). Glacier area and length changes in Norway from repeat inventories. *The Cryosphere 8*(5), 1885–1903.

Appendix 2.A Slopes and aspects along the centerlines

The average slope α along the centerlines is calculated by,

$$\alpha = \arctan\left(\frac{z_{\text{head}} - z_{\text{term}}}{l}\right), \tag{2.A-1}$$

where $z_{\text{head}} - z_{\text{term}}$ corresponds to the elevation range of the longest centerline and l to its length. The average centerline aspect θ is calculated by,

$$\theta = \arctan\left(\frac{y_{\text{term}} - y_{\text{head}}}{x_{\text{term}} - x_{\text{head}}}\right), \tag{2.A-2}$$

where $x_{\text{term}} - x_{\text{head}}$ and $y_{\text{term}} - y_{\text{head}}$ correspond to the x- and y-components of the vector between terminus and head of the longest glacier centerline. The arctan function accounts for the correct quadrant.

Besides the values along the entire centerline, we calculate slopes and aspects for sub-segments that make up 10% of the total length. Here, the head and term components in Equations 2.A-1 and 2.A-2 correspond to the start and end points of the segments.

Appendix 2.B Additional figures

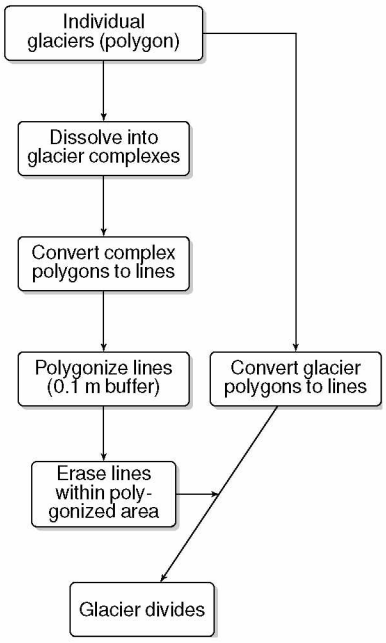

Figure 2.B-1: Fully automated five-step workflow for the automated extraction of glacier divides.

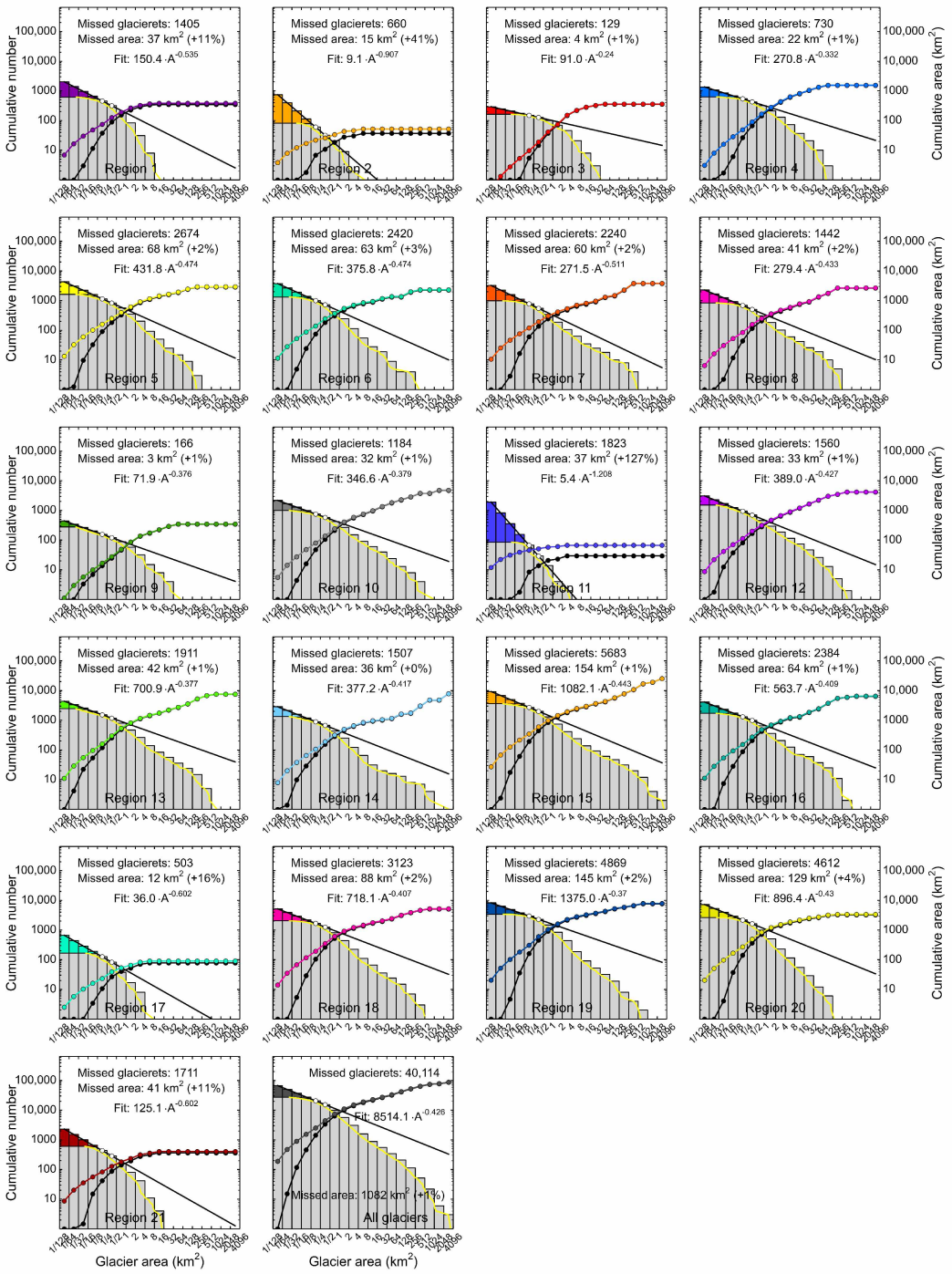

Figure 2.B-2: Uncertainties due to omission errors for all 21 regions. Number of missed glacierets as a function of area, assuming the power law size distribution between the 0.125-0.25 and the 0.25-0.5km^2 size classes down to the smallest size class. The light gray histogram/yellow line shows the cumulative frequency distribution of glacier size while the color-coded histogram indicates potentially missed glacierets. The black line shows the used power-law fit. Dotted lines show the cumulative glacier area with and without the potentially missed glacierets included.

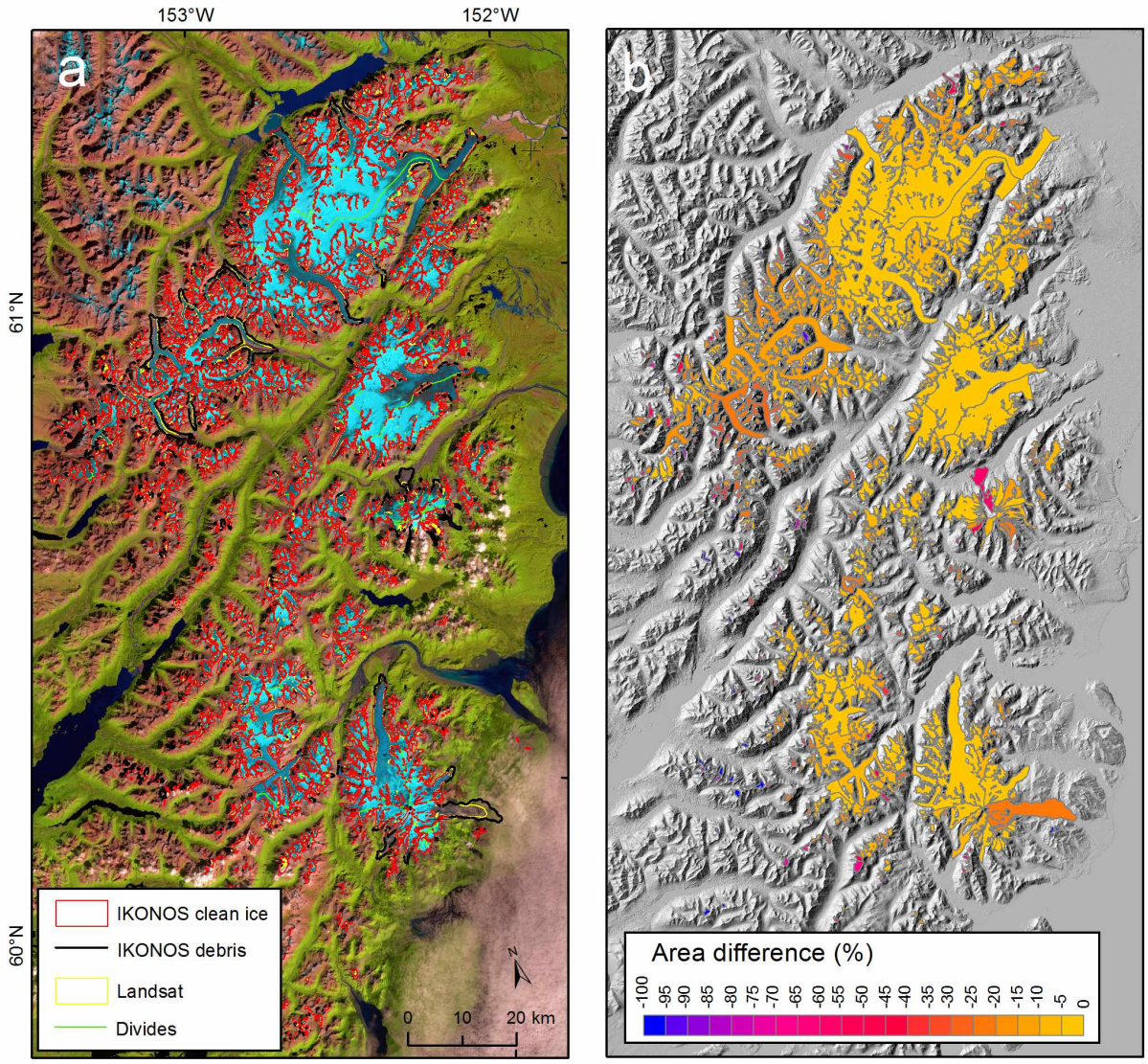

Figure 2.B-3: a) The Northern Aleutian Range region with outlines derived semi-automatically from 2007 Landsat-TM scenes (Le Bris et al., 2011) and corresponding outlines manually adapted to match IKONOS imagery from 2006 to 2010. The base map corresponds to the 2007 Landsat image. b) Relative area differences ($100 \cdot (\text{Area}_{\text{Landsat}} - \text{Area}_{\text{IKONOS}}) / \text{Area}_{\text{IKONOS}}$) for each glacier.

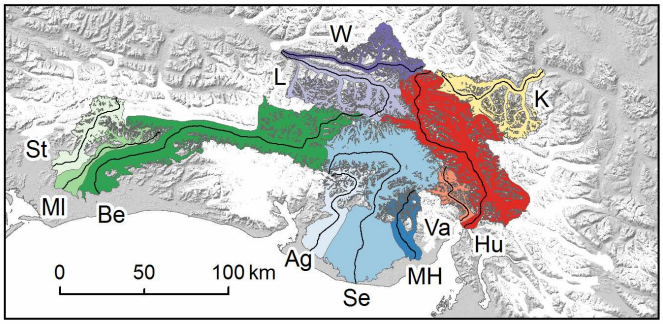

	Glacier	Area (km^2)	Length (km)	Glacier system
1	Seward (Se)	3363	137	Malaspina
2	Bering (Be)	3025	197	Bering
3	Hubbard (Hu)	2834	131	Hubbard
4	Logan (L)	1177	91	Logan-Walsh
5	Kaskawulsh (K)	1054	81	
10	Agassiz (Ag)	832	76	Malaspina
12	Steller (St)	744	67	Bering
13	Walsh (W)	718	91	Logan-Walsh
18	Bering Middle Lobe (Ml)	534	73	Bering
30	Marvine/Hayden (MH)	445	49	Malaspina
40	Valerie (Va)	345	45	Hubbard

Figure 2.B-4: The largest glaciers/glacier systems. Glaciers with similar colors make up a glacier system. Black lines show the main glacier centerline. The glaciers are ordered by area, with numbers indicating their rank.

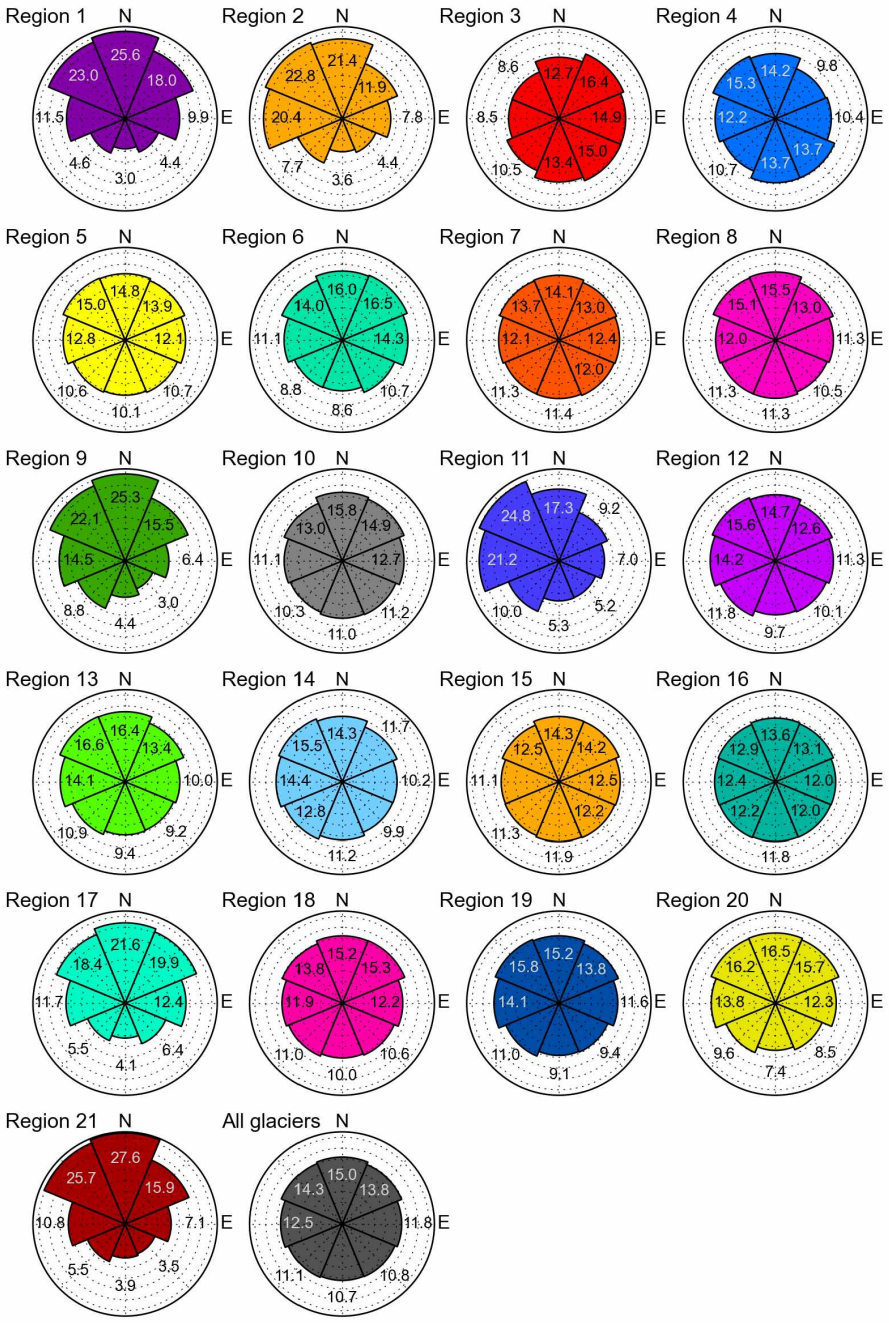

Figure 2.B-5: Area-aspect distributions for the 21 subregions.

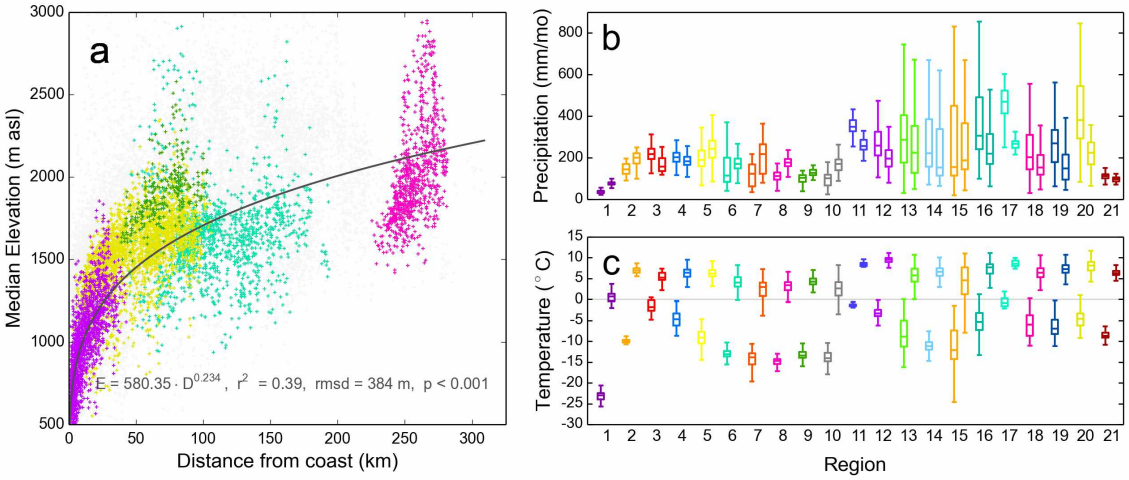

Figure 2.B-6: a) Correlation between median glacier elevation and distance from coast. A power law fit (highly significant, $p < 0.001$) is given for the entire study area, including r^2, rmsds and significane levels. Gray crosses represent the elevation-distance pairs. The colored crosses represent the distribution of five selected regions (Kenai Mountains, SW Coast Mountains, Talkeetna Mountains, Western and Eastern Alaska Range). Mean monthly precipitation (b) and mean temperature (c) of the inventoried glaciers per region. Box plots describe the distribution of the individual glacier values, measured at the median elevation. The histograms on the left reflect the months October-April (winter), the histograms on the right May-September (summer). The whiskers represent 1.5 times the interquartile range (IQR). Outliers are not shown for improved readability.

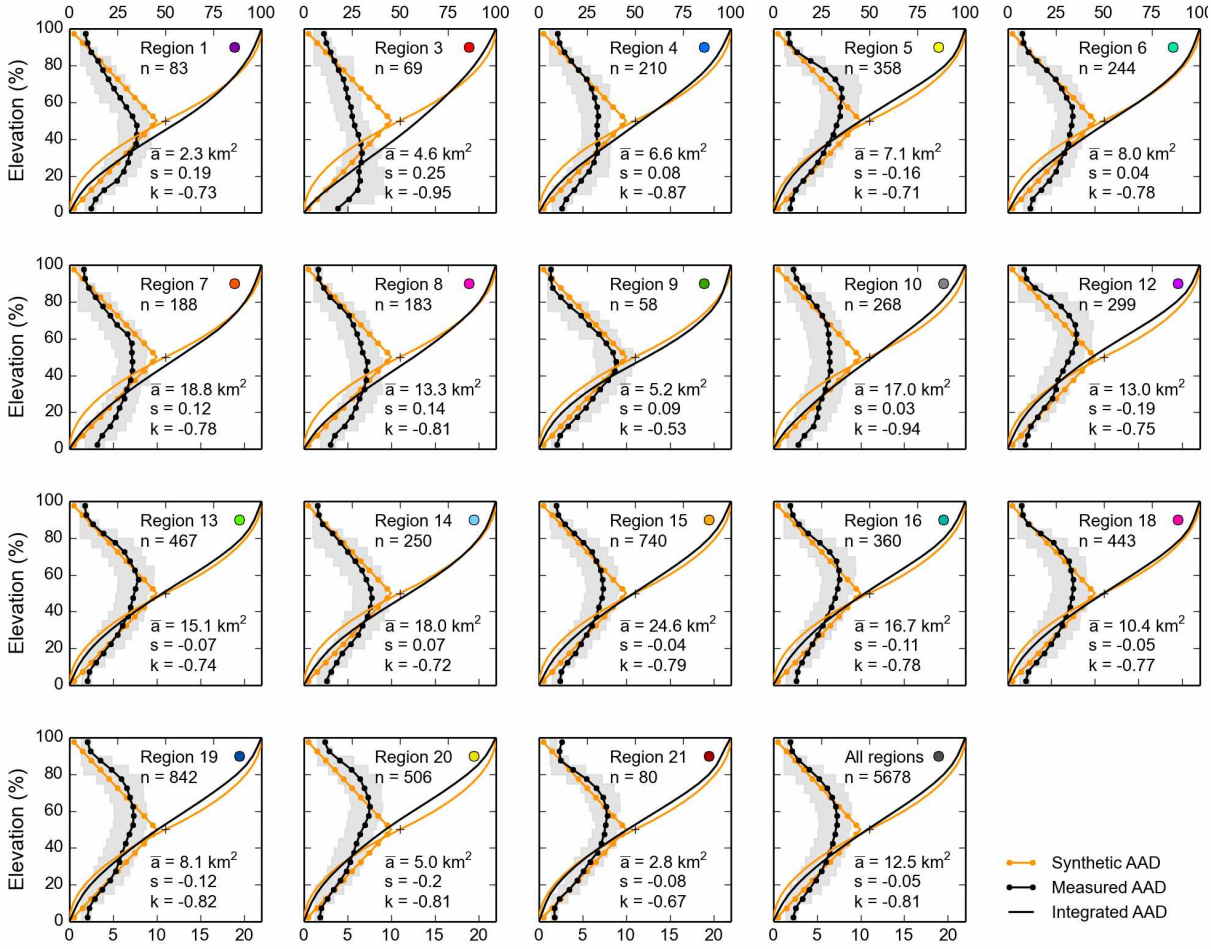

Figure 2.B-7: Normalized area-altitude distributions (AADs) for 18 selected glacier regions and the entire study area. The black connected dots show the regionally averaged AADs in 5% elevation bins. The gray shaded area shows the interquartile range (i.e., the area between the first and third quartile of the distribution) for each 5% bin. The orange dots represent the synthetic mountain glacier AAD (s = 0, k = -0.6) according to Raper and Braithwaite (2006). Solid lines (upper abscissa) show the cumulative AAD for the two distributions. n reflects the number of sampled glaciers, $\bar{a}$ the average sampled glacier size, s the skewness of the distribution (negative = top-heavy), and k the excess kurtosis (more positive = more peaked). Regions with low sample numbers (regions 2, 11, 17) are not shown. Only glaciers > 1 km^2 are included to mitigate different treatment of small glaciers in the subinventories.

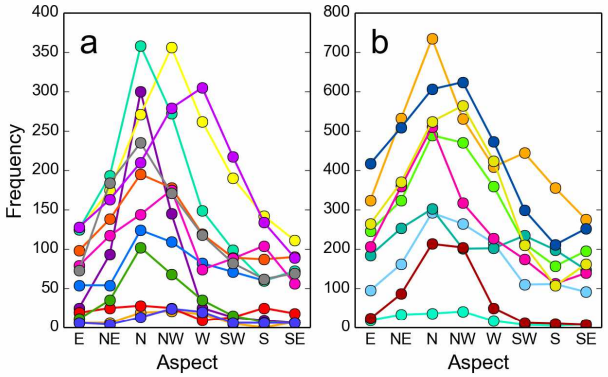

Figure 2.B-8: Number of glaciers per aspect category and region. The color-code is similar to Figure 2.B-5.

Appendix 2.C Additional tables

Table 2.C-1: Statistics for the three glacier types. Length reflects the total length of the marine- and lake-terminating margins.

Region		Land-terminating		Marine-terminating			Lake-terminating		
		Number	Area km^2	Number	Area km^2	Length km	Number	Area km^2	Length km
01	Brooks Range	616	345.6	-	-	-	-	-	-
02	Wood River Mtns	81	36.9	-	-	-	-	-	-
03	Aleutian Islands	162	354.5	-	-	-	-	-	-
04	Southern Aleutian R.	618	1341.1	-	-	-	7	187.3	7.9
05	Northern Aleutian R.	1625	2146.7	-	-	-	7	731.7	8.7
06	Western Alaska Range	1327	1922.6	-	-	-	1	341.5	3.3
07	Central Alaska Range	992	3735.6	-	-	-	2	45.7	2.5
08	Eastern Alaska Range	837	2650.9	-	-	-	-	-	-
09	Talkeetna Mountains	279	346.6	-	-	-	-	-	-
10	Wrangell Mountains	993	4670.3	-	-	-	1	97.0	4.9
11	Kodiak Island	85	29.5	-	-	-	-	-	-
12	Kenai Mountains	1500	2259.3	11	947.6	15.5	14	967.6	24.9
13	W Chugach Mtns	2430	3682.3	9	1835.3	17.4	15	2013.1	52.6
14	E Chugach Mtns	1331	3058.1	-	-	-	9	4748.1	111.9
15	St.Elias Mountains	3582	17792.3	9	5003.5	26.4	14	2470.8	98.7
16	Glacier Bay	1691	3508.4	6	804.2	10.1	24	2137.6	55.6
17	Alexander Archipelago	166	78.0	-	-	-	-	-	-
18	NE Coast Mtns	2021	3259.7	-	-	-	23	1856.7	25.9
19	Central Coast Mtns	3367	5073.9	4	1781.2	4.5	20	861.8	21.7
20	SW Coast Mtns	2614	2973.6	-	-	-	11	261.7	6.2
21	BC Interior	605	364.3	-	-	-	-	-	-
	Total	26922	59630.2	39	10371.8	73.9	148	16720.6	424.8

Table 2.C-2: List of glaciers with the longest lake-terminating boundaries. Class reflects the overall classification (2 = lake-terminating, 0 = land-terminating). Slope reflects the slope of the glacier tongue.

Glimsid	Glacier name	Terminus length m	Class	Area km^2	Slope °	Min. elev. m
G217928E60461N	Bering	41669	2	3025.117	6	3
G219572E60177N	Seward	40332	0	3362.666	5	6
G216487E60497N	Steller	28093	2	743.599	9	2
G216935E60607N	-	17257	2	488.363	7	469
G223175E58567N	Brady	13586	2	549.286	4	13
G219865E59948N	Marvine/Hayden	12093	0	445.33	5	7
G215853E60631N	Miles	10068	2	421.012	3	44
G213388E61486N	Tazlina	9219	2	373.04	3	541
G221355E60283N	Lowell	8510	2	582.829	5	475
G214720E60563N	Sheridan	8335	2	92.229	3	49
G221445E59807N	Vern Ritchie	8172	2	200.393	4	226
G221349E59562N	East Yakutat	8011	2	238.307	2	28
G210235E60050N	Bear	8000	2	198.091	4	3
G225796E59001N	Llewellyn	7746	2	297.757	4	685
G222265E59003N	Grand Plateau	6611	2	237.25	4	89
G215094E60780N	Allen	6109	2	189.244	4	66
G216395E60259N	-	5609	0	534.227	9	3
G222258E58826N	Fairweather	5599	2	165.674	4	9
G211861E61338N	Knik	5433	2	427.281	4	40
G228692E56932N	-	5421	2	103.945	6	100
G211611E61174N	Colony	4868	2	219.444	6	61
G221646E59667N	Battle	3694	2	178.165	5	203
G221954E59298N	-	3447	2	40.235	8	92
G211270E60113N	Excelsior	3429	2	122.352	7	0
G205667E58421N	Hallo	3421	2	71.633	6	55

Table 2.C-3: Selected statistical parameters for Alaska's main ice fields. The areas include disconnected glaciers within the perimeter of the main ice field.

Name	Region	Total area	Maximum length (Glacier name)
		km^2	km
Stikine IF	Central Coast M.	4500	57 (Baird)
Juneau IF	Northeastern Coast M.	3741	60 (Taku)
Harding IF	Kenai M.	1831	37 (Bear)
Sargent IF	Kenai M.	1093	31 (Chenega)

Chapter 3

Geodetic mass balance of surge-type Black Rapids Glacier, Alaska, 1980–2001–2010, including role of rockslide deposition and earthquake displacement[1]

3.1 Abstract

We determine the geodetic mass balance of surge-type Black Rapids Glacier, Alaska, for the time periods 1980–2001 and 2001–2010 by combining modern InSAR-derived DEMs, DEMs derived from archival aerial imagery, laser altimetry data and in-situ surface elevation measurements. Our analysis accounts for both the large rockslides and terrain displacements caused by the 2002 M 7.9 earthquake on the Denali fault, which runs through Black Rapids Glacier. To estimate uncertainties we apply Monte Carlo simulations. For the earthquake-triggered rockslides we find a volume of $56.62 \pm 2.86 \times 10^6$ m^3, equivalent to an average debris thickness of 4.44 ± 0.24 m across the 11.7 km^2 deposit area on the glacier. Terrain displacement due to the earthquake corresponds to an apparent glacier volume change of -53.1×10^6 m^3, which would cause an apparent specific mass balance of –0.19 m w.e. if not taken into account. The geodetic mass balance of Black Rapids Glacier is -0.48 ± 0.07 m w.e. a^{-1} for the entire 30 year period, but more negative for the period 2001–2010 (-0.64 ± 0.11 m w.e. a^{-1}) than the period 1980–2001 (-0.42 ± 0.11 m w.e. a^{-1}), in agreement with trends indicated by in-situ mass balance measurements. Elevation data indicate no net thickening of the surge reservoir between 1980 and 2010, in contrast to what is expected during the quiescent phase. A surge of Black Rapids Glacier in the near future is thus considered unlikely.

3.2 Introduction

The ice flow dynamics of surge-type glaciers oscillate between long quiescent phases and short active (surge) phases (Raymond, 1987). During the quiescent phase, low ice flux leads to elevation gain in the reservoir area and elevation lowering in the receiving area, while during the surge phase, high ice flux reverses this pattern. Given their oscillating dynamic behavior, the geometric evolution of surge-type glaciers is not easily linked to atmospheric forcing. However, like normal glaciers, surge-type glaciers are ultimately controlled by climate variables such as temperature and precipitation (Harrison and Post, 2003), which have changed considerably over the last decades (Hartmann et al., 2013). With climate warming projected to continue, glaciers will adapt their dynamics in response to negative surface mass balances, as observed in the region already (Heid and Kääb, 2012). In the case of surge-type glaciers, dynamic changes may affect their surge recurrence intervals and/or magnitudes (e.g., Eisen et al., 2001; Frappé and Clarke, 2007;

[1]Published as Kienholz, C., R. Hock, M. Truffer, A. A. Arendt, and S. Arko (2016), Geodetic mass balance of surge-type Black Rapids Glacier, Alaska, 1980–2001–2010, including role of rockslide deposition and earthquake displacement, *Journal of Geophysical Research: Earth Surface 121*, 1–24.

Flowers et al., 2011; Bevington and Copland, 2014). Glaciers might cease surging entirely, due to insufficient mass accumulation in their reservoir area, for example, as documented for several Svalbard glaciers (Dowdeswell et al., 1995) and Vernagtferner in the Ötztal Alps (Hoinkes, 1969).

Alaska and neighboring Canada host more than 300 surge-type glaciers (Sevestre and Benn, 2015), but their response to past and future climate change is not currently well understood. To further our understanding, we use surge-type Black Rapids Glacier, one of Alaska's best studied glaciers, as a case study. Black Rapids Glacier is located in interior Alaska and last surged in 1936/37 (Hance, 1937). According to the 50–75 year surge periodicity estimated by Heinrichs et al. (1996), a surge is overdue, but field observations show no indication of an imminent surge (Truffer et al., 2005). To better understand Black Rapids' current behavior and hypothesize about its future, we derive and analyze geodetic mass balances, point and centerline elevation changes, and surface mass balances for the periods 1980–2001–2010. In our analysis, we account for the rockslide deposits and the displacements caused by the M 7.9 Denali earthquake in 2002. While the rockslide deposits add a volume not controlled by the glacier's mass balance processes, the terrain displacements both invalidate the assumption of negligible elevation changes at the glacier bed and complicate the coregistration of the elevation models.

3.3 Study site

Black Rapids Glacier is a surge-type valley glacier located in the Eastern Alaska Range of interior Alaska (63.46°N, 146.53°W). In 2010, the glacier was 41.3 km long and occupied an area of 241.5 km^2, 44.5 km^2 of which was covered by moraine debris and rockslide deposits (Figure 3.1a–b). The elevation of the glacier ranged from 720 m to 3640 m a.s.l., with a median elevation of 1850 m (Figure 3.1c). While Black Rapids' main branch flows to the northwest for the first ~12 km, it drains through an east-trending valley thereafter. Three tributaries (S1, S2, Loket) currently enter the main branch from the south, of which the Loket tributary is largest (Figure 3.1b). A fourth tributary to the east was still in contact with the main branch in 1949 (approximate date of the first U.S. Geological Survey (USGS) map), but by 1980 and 2010 it had retreated ~1 km and 2 km, respectively. Six smaller tributaries (N1–N5, Melville), partially fed by hanging glaciers, enter the main branch from the north. Melville tributary, the westernmost of these six tributaries, currently flows into both Susitna and Black Rapids Glaciers, creating a divide along the center of the tributary (Fatland et al., 2003; Nolan, 2003). Black Rapids shares another major divide with the East Fork Glacier.

The geologic setting of Black Rapids Glacier is unique, as the Denali Fault runs through the valley occupied by the main trunk of the glacier (Figure 3.1a). This right-lateral strike-slip fault separates weak sedimentary rocks to the north from somewhat more stable metamorphic

and intrusive igneous rocks to the south (Wilson et al., 1998). The M 7.9 Denali earthquake on November 3, 2002 triggered three large rockslides (Jibson et al., 2006; Shugar et al., 2012), which in 2010 covered 11.7 km^2 (4.9%) of Black Rapids' area.

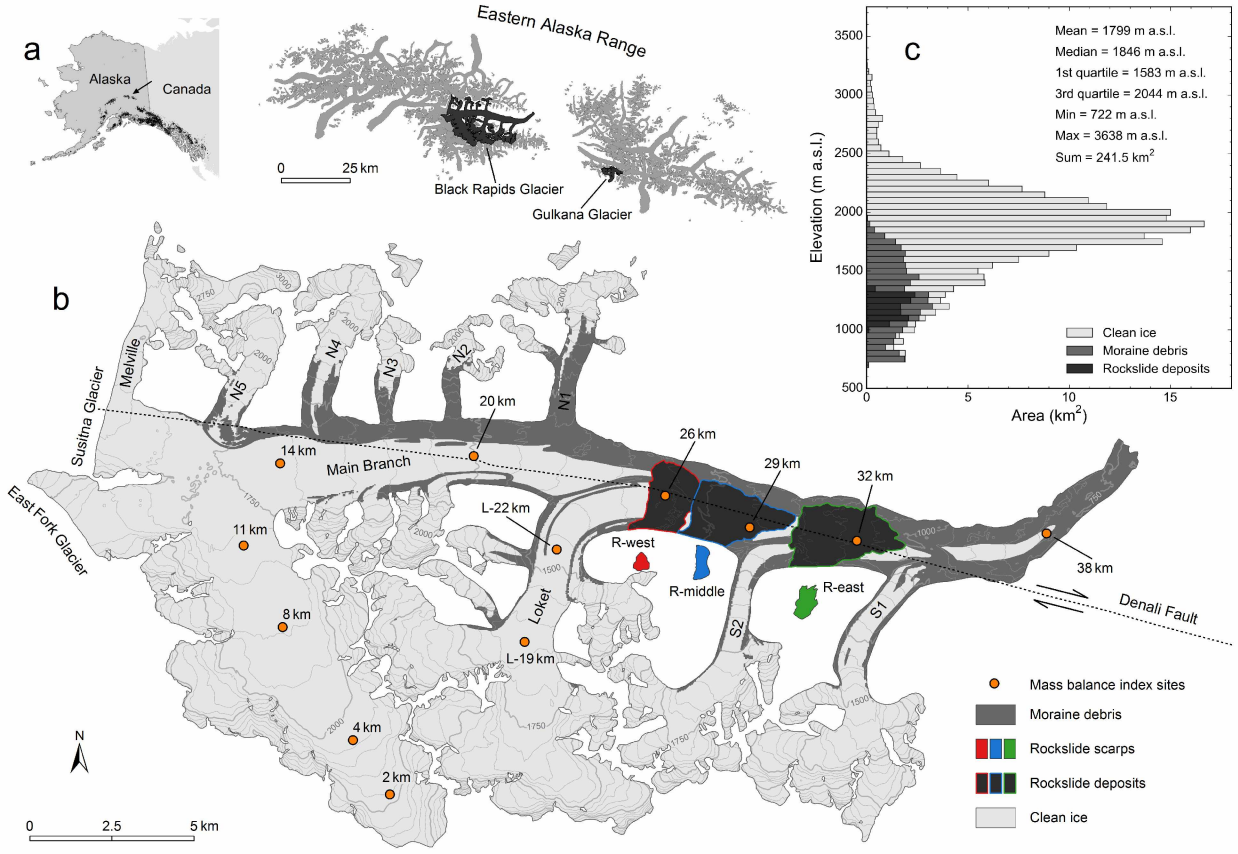

Figure 3.1: (a) Overview maps showing the location of the Eastern Alaska Range, Black Rapids Glacier and Gulkana Glacier (one of two USGS benchmark glaciers in Alaska). (b) Map of Black Rapids Glacier with glacier extent, surface topography, debris cover and rockslide deposits for the year 2010. The locations of the mass balance index sites are shown with names indicating distances along the centerlines. The approximate location of the Denali Fault is also shown along with the 2002 rockslide scarps. The naming convention for the rockslides (R-west, R-middle, R-east) is adapted from Jibson et al. (2006). (c) Area-altitude distribution in 50 m bins based on the outlines shown in (b) and the 2010 InSAR DEM. The statistics parameters refer to the entire glacier.

3.4 Previous work

From 1972 to 1987, the USGS led an extended monitoring program on Black Rapids Glacier, related to the construction of the Trans-Alaska oil pipeline close to its terminus. The planning prompted the question whether the surging glacier could interfere with the pipeline by damming

the Delta River. As part of the monitoring program, surface mass balances, elevations, and ice flow velocities were measured at up to ten index sites (Heinrichs et al., 1995). Since 1987, glaciologists mostly from the University of Alaska Fairbanks (UAF) have maintained a downsized monitoring program, consisting of two to six index sites. Glacier-wide surface mass balances have never been calculated from the collected point mass balances (Heinrichs et al., 1995; Truffer et al., 2005), but our estimates indicate they were negative for most years since the initiation of the program.

Aside from monitoring, several studies investigated Black Rapids' ice flow dynamics. Some workers focused on glacier-wide velocity fields and the temporal changes thereof by remote sensing (e.g., Rabus and Fatland, 2000; Fatland et al., 2003; Shugar et al., 2012). Others investigated the underlying processes using in-situ observations and/or modeling (e.g., Truffer et al., 2001; Amundson et al., 2006). The observed velocity oscillations from subseasonal to decadal timescales have been attributed to variations in basal motion, which in turn depend largely on subglacial hydrology (Truffer et al., 2005). Local velocity changes in the ablation area after 2002 may also be related to the rockslide deposits, in particular the rockslide-induced melt suppression (Shugar et al., 2012). See Gades et al. (2012) and references therein for an extended summary of the flow dynamics-related research.

Relatively few studies have focused on Black Rapids' mass balance explicitly. Shugar et al. (2010) investigated the glacier's elevation changes based on a ~1949 DEM (derived from USGS aerial photographs taken between 1948 and 1956) and a partial 1995 DEM (derived from European Remote Sensing satellite data), but without calculating glacier-wide volume and mass changes. As part of an Alaska-wide study, Arendt et al. (2002) determined geodetic mass balances between the same ~1949 USGS DEM and 1995 laser altimetry profiles (+0.31 $\pm$ 0.13 m w.e. a^{-1}), as well as 1995 and 2000 laser altimetry profiles (–0.64 $\pm$ 0.04 m w.e. a^{-1}). The follow-up study of Larsen et al. (2015) derived geodetic mass balances based on 1995 and 2013 laser altimetry data (–0.57 $\pm$ 0.11 m w.e. a^{-1}). Berthier et al. (2010) compiled modern SPOT- and ASTER-derived DEMs (typically from the early 2000s) across Alaska and neighboring Canada to determine regional mass changes. While these have been used to derive glacier-specific geodetic mass balances for many Alaska glaciers (Das et al., 2014; Le Bris and Paul, 2015), large portions of Black Rapids Glacier lack spatial coverage (Figure S1a in Berthier et al. (2010)).

3.5 Data

We used a range of elevation data (Table 3.1) and in-situ mass balance observations to assess Black Rapids' elevation changes and geodetic mass balances. Remotely sensed imagery was used to derive glacier outlines, rockslide scarps and deposit areas, as well as ground control points for

the derivation of DEMs and orthoimagery from legacy Alaska High Altitude Aerial Photography (AHAP).

3.5.1 IKONOS, QuickBird, and WorldView-2 imagery

High-resolution spaceborne imagery from the IKONOS, QuickBird, and WorldView-2 satellites was provided by the Polar Geospatial Center (www.pgc.umn.edu). We used 17 summer scenes (July to September) taken between 2001 and 2010, the limited swath widths (~11–17 km) of which covered only parts of the glacier. With ten scenes over the nine year period, the terminus area received most frequent coverage. In contrast, the highest glacier reaches received coverage by only one usable IKONOS scene.

Most of our high-resolution imagery was taken in non-stereo mode, so we provided our 2010 InSAR DEM (Section 3.5.3) to the Polar Geospatial Center for image orthorectifcation. Based on their orthorectified products, we created pansharpened color composites with meter (IKONOS) and sub-meter (QuickBird, WorldView-2) spatial resolution. The stated horizontal positional accuracy of the imagery ranges between ~3.5 m CE90 (WorldView-2) and ~9 m CE90 (IKONOS).

3.5.2 Alaska High Altitude Aerial Photography (AHAP)

The AHAP collection, available through the USGS EarthExplorer website (http://earthexplorer.usgs.gov), comprises aerial stereo imagery taken at 20 km altitude aboard NASA U-2 high-altitude aircraft. The panchromatic photographs used in this project were acquired on 5 August 1980. 12 scenes taken by conventional photogrammetric film cameras (Wild RC10, 153.2 mm focal length) encompass the study area, covering an area of ~25 × 25 km per scene at a ground resolution of ~3.2 m. The scenes' along- and cross-track overlap is ~60% and 20%, respectively.

3.5.3 InSAR DEMs

An Interferometric SAR (InSAR)-derived DEM covering Black Rapids Glacier in full was acquired in summer 2010 with an Intermap STAR-3 X-/P-band radar system, deployed aboard an aircraft flying at ~8500 m altitude. Multiple campaigns took place between 10 June and 1 July 2010, so the final DEM (obtained from ifsar.gina.alaska.edu) is not tied to a single day. The glacier topography was derived entirely from X-band data, which is preferred for the calculation of elevation changes given the limited penetration depth of the X-band radar signal into snow and ice (e.g., Gardelle et al., 2012). For moderately sloped terrain, the metadata states a nominal vertical precision of 1 m. From its native 5 m spatial resolution, we resampled the DEM bilinearly to 10 m, the default resolution for our processing.

Table 3.1: Elevation data overview

Name	Technique	Date	Glacier coverage	Resolution	Precision[a]	Source
				m	m	
2010 InSAR DEM	Radar interferometry	06/10–07/01/2010	Full glacier	5	~1	Intermap
2010 altimetry data	Laser scanning	05/21/2010	Centerline[b]	~1[c]	0.2	UAF
2005 altimetry data	Laser profiling	05/24/2005	Centerline[b]	~1.2[c]	0.2	UAF
2001 InSAR DEM	Radar interferometry	08/08/2001	Terminus area (~15%)	5	~3	Intermap
2000 altimetry data	Laser profiling	05/31/2000	Centerline[b]	~1.2[c]	0.2	UAF
1995 altimetry data	Laser profiling	05/18/1995	Centerline[b]	~1.2[c]	0.2	UAF
1980 AHAP DEM	Photogrammetry	08/05/1980	Lower part (~30%)	10	~7	NASA
In-situ elevation data	Theodolite/GPS surveying	1973 to date	Index sites	–[d]	0.3	USGS/UAF

[a] Error component in the vertical direction, excluding potential biases.

[b] Main branch and Loket tributary centerlines.

[c] Laser shot point spacing.

[d] Point survey.

A precursor STAR-3 airborne radar (X-band only) was deployed along the Alaska Range corridor of the Richardson Highway on 8 August 2001 (ifsar.gina.alaska.edu). The acquired DEM covers the terminus area of Black Rapids Glacier (~15% of the total area) with a spatial resolution of 5 m and a nominal vertical precision of 3 m. Some steeper portions of this DEM contain blunders (interpolated missing data), caused mainly by radar shadow and layover. We manually masked out these flawed areas based on the shaded relief DEM.

3.5.4 Laser altimetry data

We used elevation data from four airborne laser campaigns conducted by the UAF laser altimetry group in 1995, 2000, 2005, and 2010. The 2010 data are available from the National Snow and Ice Data Center (Larsen, 2010) and the 1995–2005 data from the UAF laser altimetry group (upon request). Prior to 2010, the acquired data consisted of elevation profiles along the centerlines of Black Rapids' main branch and the Loket tributary. Starting in 2010, a scanner system provided a DEM swath (~500 m wide) along the centerlines. See Johnson et al. (2013) for more information on the laser systems.

3.5.5 In-situ elevation data

As part of the Black Rapids monitoring program, in-situ glacier elevations were measured at up to ten index sites, eight along the centerline of the main branch and two along the centerline of the Loket tributary (Figure 3.1). Theodolite space resection was used initially (Heinrichs et al., 1995) and GPS surveying later in the program (Truffer et al., 2005). In the pre-GPS era, several points were surveyed around the index sites and subsequently used to interpolate the elevation of the actual index sites. This approach has been maintained to date, mostly to reduce sensitivity to small-scale topographic features.

3.5.6 In-situ surface mass balance data

During the extensive USGS monitoring program from 1972 to 1987, surface mass balances were measured at the index sites at least twice a year in spring and fall. Since 1987, the downsized UAF mass balance program has consisted of two to six sites visited once per year in spring (Truffer et al., 2005). Together, both datasets comprise more than 200 annual point balance observations for the period 1972 to 2013. Two index sites located in the main branch (8 km and 14 km, Figure 3.1) have a nearly complete record of annual surface mass balances.

3.6 Methods

Our processing workflow was initiated with the derivation of the AHAP DEM and the preparation of the laser altimetry data. Upon matching the vertical datums and horizontal coordinate systems, and correcting for the earthquake-related displacements, we coregistered the DEM products. We then extended the partial DEMs to the entire glacier, which allowed for calculation of glacier-wide geodetic mass balance. We also quantified the rockslide volumes to take them into account during calculation of geodetic mass balance terms. The applied processing steps came with a range of uncertainties, which we addressed in a Monte Carlo error analysis (Section 3.7).

3.6.1 Derivation of the 1980 AHAP DEM

Structure from motion photogrammetric processing (using Agisoft Photoscan software) was applied to derive a DEM from the AHAP collection. With no ground control points surveyed at the time of the airborne campaign, we derived them post-hoc using our collection of remotely sensed data. We identified persistent features on both the AHAP imagery and the high-resolution satellite orthoimagery, which provided the control points' horizontal coordinates. These were complemented with elevations derived from the 2010 InSAR DEM. 12 control points spread around the glacier were used for the final DEM. Derivation of additional points was hampered mostly in the higher terrain, where the AHAP imagery lacked well identifiable features.

The DEM derivation failed in snow covered areas due to poor contrast in the original imagery. Based on the shaded relief of the resulting DEM, we excluded the flawed areas manually. Ultimately, the lowest ~30% of Black Rapids Glacier was covered by the AHAP DEM.

3.6.2 Processing of the laser altimetry data

Our processing of the laser altimetry data was adapted from the workflow detailed in Johnson et al. (2013). For the 10 m DEM cells covered by the laser profiles/swaths, we calculated the mean of all point elevation observations and subtracted them from the corresponding 2010 InSAR DEM elevations. Upon application of a moving median, we assigned the cell-specific elevation differences to 30 m elevation bins and calculated measures of center (means, medians) and spread (standard deviation, quartiles) for each bin. Connecting the parameters of the individual bins resulted in elevation change (Δz) vs. elevation curves. Gaps due to missing laser data in the corresponding bins were filled by linear interpolation. We implemented an additional smoothing function, which computes convolution on the Δz vs. elevation curves using a Kaiser window (http://docs.scipy.org/doc/numpy-1.10.0/reference/generated/numpy.kaiser.

html). This function generates a slightly smoothed Δz vs. elevation curve at a higher resolution (one Δz value per 15 m elevation bin).

3.6.3 Matching of vertical datums and horizontal coordinate systems

Our elevation products covered the full range of possible vertical reference systems in Alaska: NAVD88 (2010 InSAR, 1980 AHAP), EGM96 (2001 InSAR), WGS84 (altimetry data), and NGVD29 (index site elevations). Sampling the appropriate geoid models (http://earth-info.nga.mil/GandG/wgs84/gravitymod/egm96/egm96.html, http://www.ngs.noaa.gov/GEOID/GEOID09) and consulting National Geodetic Survey benchmarks around Black Rapids Glacier (http://www.ngs.noaa.gov/cgi-bin/datasheet.prl), we brought our datasets to the common vertical datum NAVD88. We matched the vertical datums prior to the DEM coregistration (Section 3.6.5) because the coregistration eliminates only spatially constant offsets between two DEMs, while offsets between vertical datums can vary even over short distances (e.g., >0.5 m when comparing NAVD88 (Geoid09) and EGM96 across our study area). For the horizontal coordinate system, we chose Alaska Albers (EPSG:3338), the coordinate system of the 2010 InSAR DEM.

3.6.4 Accounting for earthquake-related displacements

The 2002 rupture of the right-lateral strike-slip Denali Fault caused terrain displacements up to several meters in magnitude around Black Rapids Glacier (Jibson et al., 2006; Elliott et al., 2007). Since the fault lies beneath the glacier, the ice and the underlying bedrock ruptured. Due to the elevation changes at the glacier bed, the earthquake-related displacements had to be accounted for not only during DEM coregistration, but also in calculations of geodetic mass balances. Most of our elevation data were taken before 2002, so we adjusted the 2010 InSAR DEM to its pre-earthquake state.

Elliott et al. (2007) estimated the 2002 terrain displacements based on RADARSAT-1-derived range offsets, terrain offsets measured in the field, GPS observations, and 3-D modeling. They provided model-derived horizontal and vertical shift vectors on a 250 $\times$ 250 m grid, which matched their SAR-derived equivalents closely along a profile close to the glacier (0.33 m RMSE). Unlike their UTM projection, Alaska Albers deviates $\sim$6.5° from true north in our study area, which obliged us to convert their shift components (east, north, up) into the corresponding Alaska Albers x, y and z shift components. Using inverse distance weighting with a breakline along the fault, we then interpolated the x, y and z components to the 10 m resolution of the 2010 InSAR DEM, and applied these shifts to the center of each DEM cell, which resulted in a new DEM

with irregular spacing. To obtain the final displacement-corrected DEM with regular spacing, we bilinearly interpolated the irregular grid back to the original 10 m spacing.

3.6.5 DEM coregistration

To correct for remaining DEM geolocation errors, we followed the coregistration approach outlined in Nuth and Kääb (2011). By comparing the 1980 and 2001 DEMs to the earthquake-corrected 2010 DEM, we determined spatially constant shift vectors in the x, y and z directions, which we then applied to the 1980 and 2001 DEMs. We compared elevations over ice- and vegetation-free grid cells that had no signs of creep or slides and lacked any obvious blunders.

For the 1980 AHAP DEM, shifts of –7.96 m in the x, –10.10 m in the y and –1.38 m in the z direction were obtained. After coregistration, the mean (μ) and standard deviation (σ) of the elevation difference (Δz) distribution were zero and 7.06 m, respectively (Figure 3.2a). Prior to the coregistration, σ was 9.17 m. While μ quantifies the remaining elevation bias, σ describes the elevation error that is partly correlated (i.e., subject to some degree of spatial autocorrelation). The coregistration eliminated the distinct sinusoidal Δz variation with terrain aspect (Figure 3.2b–c), suggesting an improved match of the two DEMs over the terrain used for coregistration. Based on visual inspection of the Δz grids, we suspect some remaining higher-order shifts in the AHAP DEM, most likely as a consequence of the sparse ground control used during the photogrammetric processing. Such higher-order shifts were not correctable by the DEM coregistration used here, which provided global shifts only.

In the case of the 2001 InSAR DEM, the derived shifts were 1.16, 1.20 and 0.25 m in the x, y and z directions, respectively. μ improved to zero and σ from 2.41 to 2.26 m, leaving no sinusoidal Δz variation with terrain aspect. Limited higher-order shifts remained, potentially as a result of an imperfect earthquake displacement correction. Compared to the 3.16 m derived from propagating nominal vertical precisions (1 and 3 m, Table 3.1), our σ value is 0.9 m lower, suggesting the InSAR DEMs have slightly better quality than specified in the metadata. Smaller shifts in all three directions and a considerably smaller final σ value suggest higher accuracy and precision for the 2001 InSAR than the 1980 AHAP DEM.

To quantify potential remaining biases in the vertical direction (the effect of which is greatest for elevation change calculations), we differenced the independently coregistered 1980 and 2001 DEMs over low-angle terrain unused for the coregistration, which revealed a remaining systematic offset of 1.2 m. Although the μ values above were both zero, this prompted us to take into account potential remaining biases in the error analysis (Section 3.7), especially in the case of the 1980 AHAP DEM.

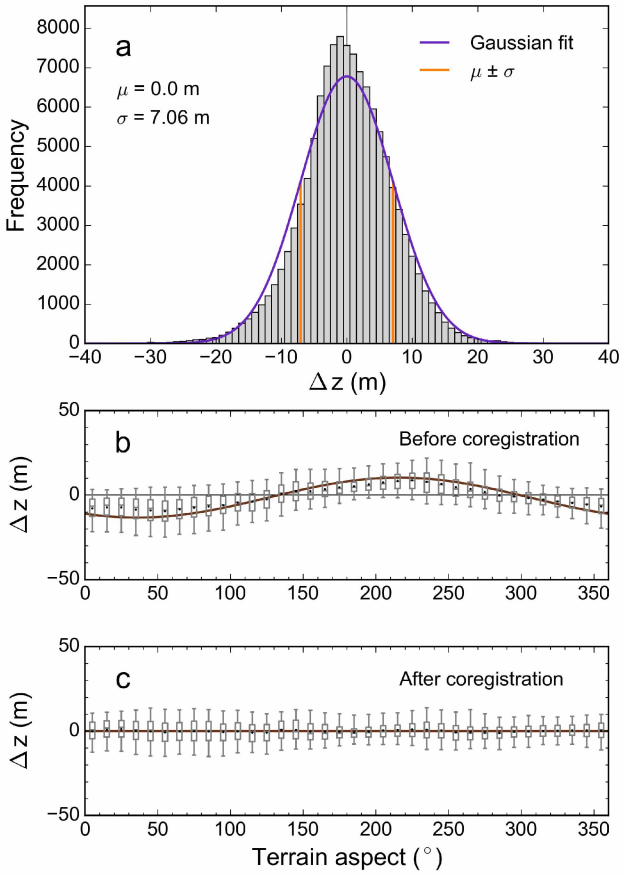

Figure 3.2: (a) Elevation differences (1980 AHAP – 2010 InSAR) over stable terrain, with frequencies indicating the number of grid cells per 1 m bin. (b–c) Elevation differences as a function of the terrain aspect before (b) and after coregistration (c). Brown lines indicate the curves $a\ \cos(b - \psi)\ \tan(\alpha) + c$, fitted to the Δz values by least squares minimization. a, b and c are the parameters fitted, α and ψ correspond to the terrain slope and aspect, respectively (Nuth and Kääb, 2011). The box-and-whisker plots describe the original Δz values per 10° aspect bin. In addition to the standard box plot (25, 50 and 75 percentiles), black dots show the means and whiskers the 5 and 95 percentiles of the distributions, respectively.

We note that the coregistration occurred in terrain that, on average, was twice as steep as the glacierized area of Black Rapids (~25° vs. 12.5°). The performance of photogrammetric and radar techniques tends to decline with increasing terrain slope, so the derived elevation errors likely reflect conservative error estimates for the relatively flat glacierized areas.

3.6.6 Calculation of rockslide volumes

Previous work (Jibson et al., 2006) inferred the rockslide volumes by integrating an estimated uniform debris thickness across the deposit areas. The thickness (3 m) was estimated from reconnaissance flights without measurements on the ground. No DEMs are available immediately before and after the rockslides' occurrence, so the deposit thickness cannot be quantified by DEM differencing directly. DEMs further apart in time are impractical as they include considerable elevation changes due to surface mass balance and ice flow, which are difficult to isolate.

We here took an alternative approach by analyzing the rockslide source areas. We differenced our pre-slide (1980 AHAP, 2001 InSAR) and post-slide DEMs (2010 InSAR) across the rockslide scarps, followed by integrating the derived elevation changes within the scarp boundaries, which we digitized from satellite imagery. Two of the scarp areas hosted glacierets that vanished with the rockslides. Their thinning prior to the rockslides was taken into account, which was especially important when using the 1980 AHAP DEM, given the 22 year difference between the DEM and rockslide dates. We did this by applying thinning rates from neighboring glacierets not affected by the rockslides. The release volume obtained from the DEM differencing included both rock debris and ice from the glacierets. To obtain a rough estimate for the ice fraction in the volumes released, we applied volume-area scaling (Bahr et al., 1997) to the 2001 glacieret areas using coefficients of $c = 0.31$ and $\gamma = 0.335$ found for Alaska (Huss and Farinotti, 2012).

3.6.7 Extending partial DEMs to the entire glacier

To compute glacier-wide volume changes, we extended the partial 1980 AHAP and 2001 InSAR DEMs to the entire glacier, based on laser altimetry and index site elevation data. These data were taken along the centerlines and thus needed extrapolation to the remaining glacier parts. The processed laser altimetry data (Section 3.6.2) provided Δz vs. elevation curves for both the Loket and the main branch. Applying similar processing steps to the index site elevations, we quantified the thinning between 1980 and 2010 at the index site locations. To derive the complete glacier topographies for 1980 and 2001, we applied the Δz curves in the negative direction to the 2010 DEM portion of each branch. This retained the overall shape of the 2010 topography while moving it vertically as prescribed by the curve. Combining these adapted DEMs with the available

partial DEMs of 1980 and 2001 yielded the final glacier-wide DEMs. See Appendix 3.A for details on the DEM extension.

Our approach resembles that taken in laser altimetry studies to quantify glacier-wide volume changes from centerline profiles. Unlike Johnson et al. (2013), we treated individual branches separately, accounting for variable thinning rates among different branches of the glacier. Additionally, our workflow generated actual glacier-wide DEMs based on the centerline data, usable for applications besides volume change calculations (e.g., for mass balance modeling).

3.6.8 Calculation of geodetic mass balances

Using our extended DEMs from 1980 and 2001 together with the 2010 DEM, we obtained glacier-wide geodetic mass balances for the periods 1980–2001–2010. We first calculated the glacier volume changes by differencing the newer from the older DEMs, followed by integrating the Δz values over the larger of the two glacier areas. Upon correcting for rockslide volume, we converted the volume change into mass changes. We used a conversion factor (bulk density) of 850 $\pm$ 60 kg m^{-3} as suggested by Huss (2013). For glacier-wide specific mass balance rates, we divided mass change by the time between the surveys and the average of the old and new glacier areas (Finsterwalder, 1954). We refrained from conducting seasonal corrections (e.g., Cox and March, 2004; Cogley et al., 2011), so our results reflect the mass changes between the surveys rather than the actual balance years. Our mass balance calculations relied on glacier outlines compiled for each DEM specifically (1980, 2001, 2010). We obtained the 2001 outlines by adapting the Black Rapids outlines from the Alaska glacier inventory (Kienholz et al., 2015) based on our IKONOS color composites. Using the AHAP orthomosaic and a set of WorldView-2 imagery, we adapted the 2001 outlines to obtain outlines for 1980 and 2010.

Using the earthquake-corrected rather than the original 2010 DEM resulted in glacier bed elevations canceling out during the volume change calculation, which we show below for the 2001–2010 period. The volume change ΔV, neglecting the rockslide volume, is given by:

$$\Delta V = \iint (h_{\text{surf},2010}(x,y) - h_{\text{bed},2010}(x,y))\, dxdy \; - \iint (h_{\text{surf},2001}(x,y) - h_{\text{bed},2001}(x,y))\, dxdy, \qquad (3.1)$$

where $h_{\text{surf},2010}$ and $h_{\text{surf},2001}$ correspond to the surface elevations, and $h_{\text{bed},2010}$ and $h_{\text{bed},2001}$ to the bed elevations from 2010 and 2001, respectively. Assuming negligible glacier volume change during the earthquake (i.e., zero net divergence of the displacement field across the glacier body), the integrated earthquake displacements across the glacier surface must equal those across the glacier bed (Gauss's theorem). Accordingly, Equation 3.1 corresponds to:

$$\Delta V = \iint (h_{\text{surf},2010,\text{corr}}(x,y) - h_{\text{bed},2010,\text{corr}}(x,y))\, dxdy \; - \iint (h_{\text{surf},2001}(x,y) - h_{\text{bed},2001}(x,y))\, dxdy, \quad (3.2)$$

where $h_{\text{surf,2010,corr}}$ and $h_{\text{bed,2010,corr}}(x,y)$ denote the earthquake-corrected surface and bed elevations from 2010. Assuming negligible bed erosion between 2001 and 2010, $h_{\text{bed,2010,corr}}$ cancels out $h_{\text{bed,2001}}$, which leaves:

$$\Delta V = \iint (h_{\text{surf,2010,corr}}(x,y) - h_{\text{surf,2001}}(x,y))\, dxdy. \tag{3.3}$$

The total glacier mass change ΔM is then computed by:

$$\Delta M = (\Delta V - V_{\text{slide}})\,\rho, \tag{3.4}$$

where V_{slide} denotes the rockslide deposit volume and ρ the bulk density.

3.7 Uncertainties and error analysis

The ultimate goal of the error analysis was to determine the total uncertainties in the glacier-wide geodetic mass balances. We here also emphasize the uncertainties in the rockslide volume estimates, which are important for both glaciological and geological applications.

The large number of error sources, and the fact that some of these errors could not be considered by standard error propagation, prompted us to apply a Monte Carlo analysis. While computationally intense, Monte Carlo methods are less restricted than error propagation methods. For example, Gaussian distribution of individual errors is not required. Moreover, Monte Carlo approaches can sample physical datasets, for example, different versions of glacier outlines to capture the effects of outline uncertainties. They can also provide output (e.g., DEMs) for each run, which can serve follow-up applications such as error assessments in mass balance modeling.

3.7.1 Uncertainties in rockslide volumes

Uncertainties in rockslide volume resulted from: 1) residual elevation errors in the DEMs, including partially correlated errors and biases; 2) uncertainties in the delineation of the rockslide scarp areas; 3) errors in estimates of glacier thinning in the scarp areas between DEM date and rockslide occurrence; 4) errors caused by deposition of rockslide material outside the glacier perimeter; 5) uncertainties in the derived deposit areas used to compute the average deposit thicknesses.

To address error source 1, we perturbed the original Δz grids with the residual elevation errors from the DEM coregistration (Section 3.6.5). We accounted for the elevation errors' spatial autocorrelation by semivariogram analysis of the original Δz grids over unglacierized terrain (e.g., Rolstad et al., 2009; Motyka et al., 2010). Rather than a single range value r, the empirical semivariograms suggested plausible r values somewhere between 250 and 1000 m. These numbers bracketed a uniform distribution that we sampled once per Monte Carlo run to arrive at a specific

r value for that run. We then calculated the correlation area $A = \pi r^2$ (Motyka et al., 2010), inside/outside which we assumed elevation errors to be fully correlated/uncorrelated. Upon dividing the Δz raster into subregions with area A, we sampled elevation errors and assigned them to the subregions. The sampling occurred from Gaussian error distributions with σ values of 2.26 m (2010 – 2001 InSAR) and 7.06 m (2010 InSAR – 1980 AHAP), as derived in Section 3.6.5. To account for potentially remaining biases (the magnitude of which was somewhat uncertain), we defined the μ values of these error Gaussians by Gaussians themselves (0 ± 0.75 m for the 2010–2001 InSAR comparison, 0 ± 1.5 m for the 2010 InSAR–1980 AHAP comparison). We sampled these Gaussians once per Monte Carlo run, which provided the specific μ value to define the error Gaussians fully.

We treated the error sources 2 and 5 similarly. Each Monte Carlo run, we sampled one outline from a pool containing multiple digitized outline versions (see Appendix 3.B for details on the derivation of the outline versions). To account for glacier thinning inside the scarps (error source 3), we delineated the glacierized portions within the scarps for 1980 and 2001. We then calculated the thinning of neighboring glacierets not affected by the rockslides, yielding annual thinning rates of 0.43 ± 0.25 m for the period 1980–2010, which we applied to the glacierets in the scarps. Each Monte Carlo run, we sampled one specific thinning rate from the distribution, and in the case of the AHAP DEMs, multiplied this rate by 22 (the year difference) and the average glacier area of 1980 and 2001 (to account for the retreat of the glacierets over the 22 years). In the case of the 2001 InSAR DEM (taken approximately one year before the rockslides occurred), we multiplied the sampled thinning rate by the glacierized area in 2001. Regarding error source 4, imagery indicated almost all released material reached the glacier. We prescribed a uniform distribution of reduction factors ranging from 0.925 to 0.975, meaning that between 92.5 and 97.5% of the material actually reached the glacier.

We calculated the rockslide volumes 25,000 times, resulting in Gaussian volume distributions. Figure 3.3 shows the resulting distributions for the actual volumes released (i.e., before applying the reduction factor of error source 4), with standard deviations corresponding to the final error estimates.

3.7.2 Uncertainties in geodetic mass balances

The combined uncertainties in the geodetic mass balances are due to: 1) residual elevation errors in the DEMs; 2) errors in the glacier outlines; 3) uncertainties in the rockslide volumes; 4) uncertainties in the bulk densities and 5) uncertainties in the date of the 2010 InSAR DEM.

Error source 1 was treated as described in the previous section. In the glacier areas outside the partial 1980 and 2001 DEMs, additional uncertainties had to be taken into account, as detailed in

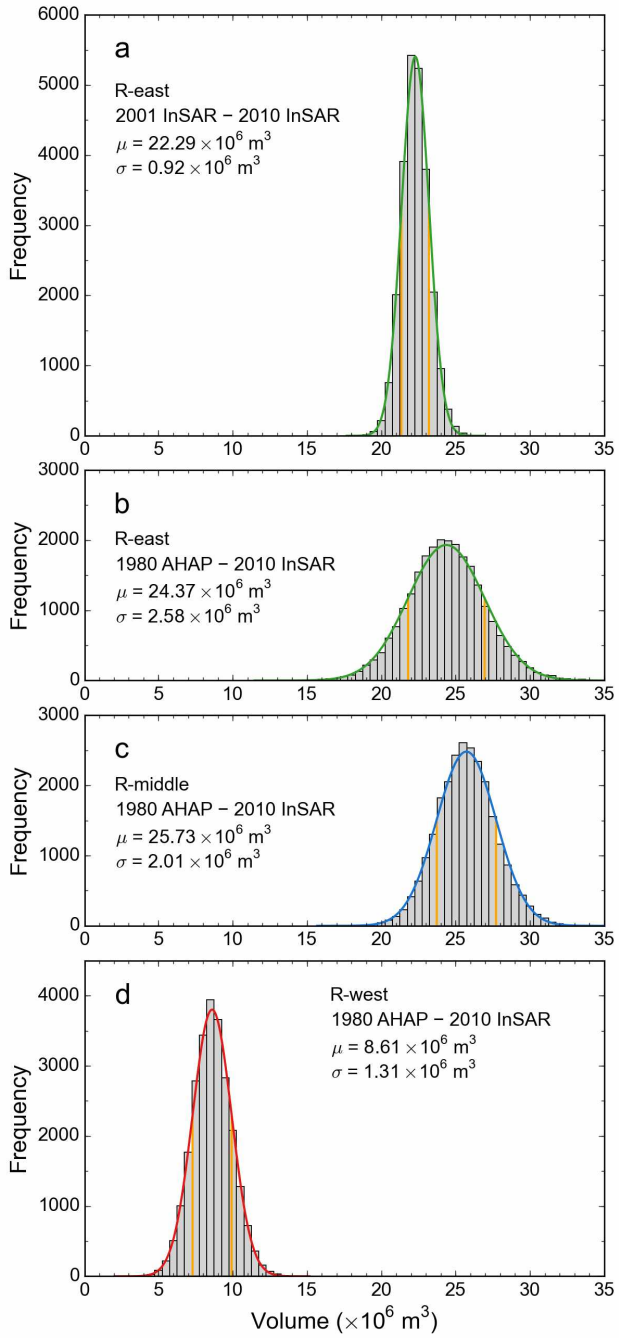

Figure 3.3: Frequency distribution of released rockslide volumes per $5\times10^5 m^3$ bin for rockslides R-east (a, b), R-middle (c) and R-west (d), as derived from 25,000 Monte Carlo runs. Solid curves mark the Gaussian fits to the data. The orange vertical lines bracket $\mu \pm \sigma$ (68.2% of the Gaussians' areas), which served as error estimates during subsequent calculations.

Appendix 3.A. Regarding error source 2, we sampled outlines from a pool with multiple glacier outline versions (Appendix 3.B). For error source 3, we used the rockslide volumes derived in the previous section (a Gaussian distribution), and for 4, we sampled from the Gaussian distribution 850 ± 60 kg m^{-3} suggested by Huss (2013). Error source 5, which affects the calculation of the specific mass balances, was accounted for by sampling from the date range in the 2010 InSAR DEM metadata (a uniform distribution). Potential errors in the earthquake displacement correction and errors due to X-band radar penetration were not taken into account separately. We assumed them to be included in error source 1.

We calculated the geodetic volume changes 10,000 times, again yielding Gaussian distributions. Tests indicated 10,000 runs were sufficient to obtain stable results; in fact, experiments with only a few hundred runs yielded almost identical error estimates.

3.8 Results and discussion

3.8.1 Elevation and area changes

3.8.1.1 Multi-year to decadal changes

Between 1980 and 2010, Black Rapids Glacier underwent substantial thinning. The thinning was most pronounced in its lower reaches (up to 200 m from 1980–2010, Figures 3.4, 3.5) and accompanied by glacier retreat, which reduced Black Rapids' length and area by ~1.4 km (42.7 vs. 41.3 km) and ~7.3 km^2 (248.8 vs. 241.5 km^2), respectively. While the retreat clearly shows in the elevation change maps (Figure 3.4a–b), it is less visible in the satellite imagery, due to extensive debris cover in the terminus area (Figure 3.4f–g).

The highest thinning rates of up to 200 m over the 30 year period (>6.5 m a^{-1}) occurred along a drainage channel that eroded into lateral, debris-covered ice (Figure 3.4a). The thinning of the lowest debris-free ice reached up to 170 m over the 30 year period (Figure 3.4d). This exceeds the thinning rate of neighboring debris covered glacier portions (~120–170 m), suggesting debris is sufficiently thick in this area to suppress ice melt. The differences in specific melt rates are likely to be even larger than the differences in elevation changes, as the debris-covered ice is higher than the neighboring clean ice (~40 m), which promotes local ice flow from the debris-covered to the clean glacier portions. Unfortunately, this effect is difficult to quantify without corresponding in-situ measurements.

The rockslide deposits stand out in the elevation change maps, especially over the 2001–2010 period. Across the deposits, elevation gain dominates over the nine years, with large areas gaining more than 5 m in elevation (Figure 3.4b,d). There are areas of negative elevation change at the same time, especially along the northern portion of the R-east deposit. Local deposit thickness,

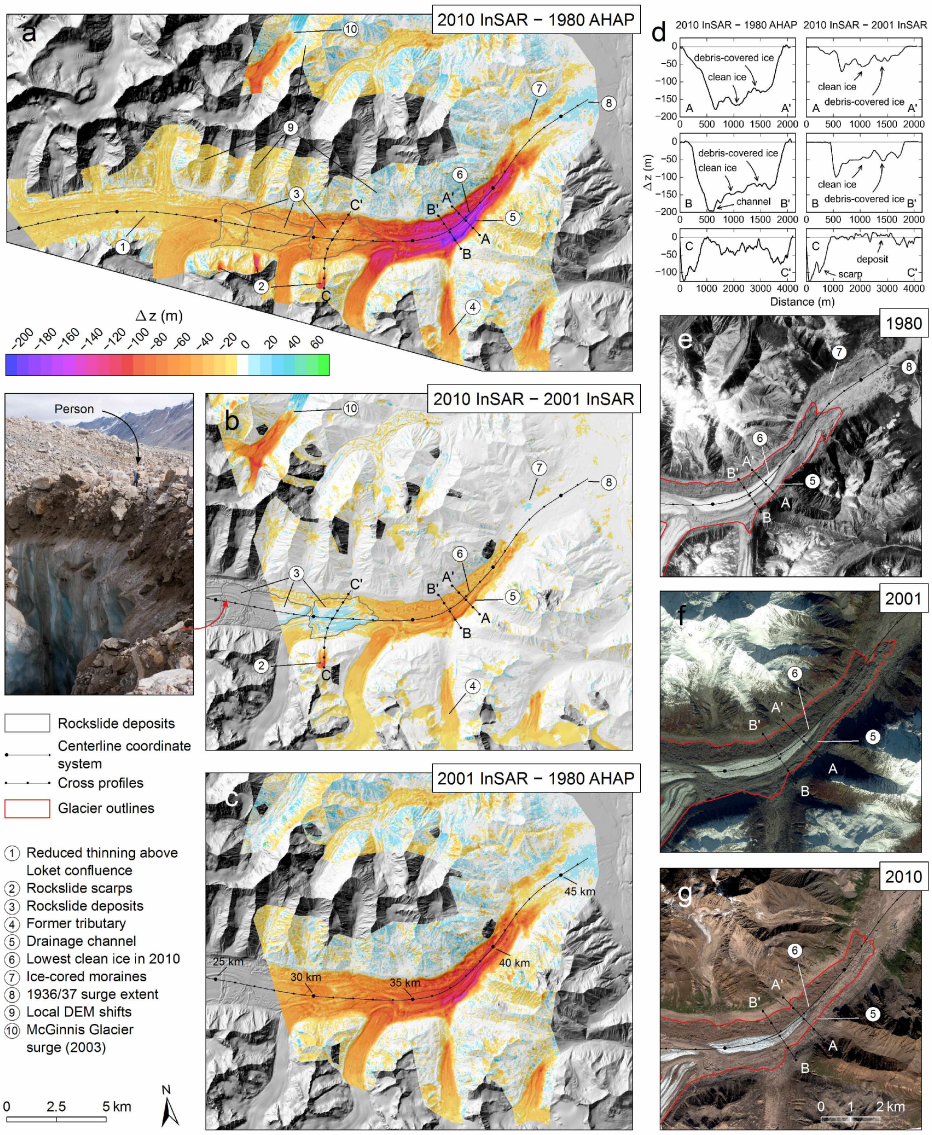

Figure 3.4: (a–c) Maps of elevation changes for the three periods 1980–2010, 2001–2010, and 1980–2001. Several features of interest are annotated. The centerline coordinate system is given and has kilometer annotations in (c). The shaded relief DEM in the background is derived from the 2010 InSAR DEM. The photograph to the left of (b) shows the deposit thickness next to a large moulin (photo courtesy of Dan Shugar, University of Washington Tacoma). (d) Elevation changes sampled along three cross profiles located in the terminus area (A, B) and the path of rockslide R-east (C). The periods 1980–2010 and 2001–2010 are represented by the left and right panels, respectively. The profile locations are given in (a) and (b) including 500 m markers. (e) AHAP orthoimage of the terminus area at the same scale as the elevation change maps. The 1936/37 surge extent is visible at 46.5 km. (f) IKONOS and (g) WorldView-2 orthoimages (© 2011, DigitalGlobe, Inc.) with glacier outlines for the corresponding years. Note the larger scale in (f) and (g).

surface mass balance and ice flow divergence are the controlling factors for the elevation changes. They are closely intertwined and virtually impossible to quantify based on remotely sensed data alone. In-situ measurements of debris thicknesses and temperatures (allowing for the calibration of a melt model at the ice-debris interface) could mark a first step towards a better understanding of these controlling factors.

Over the study period, particularly pronounced thinning occurred along the confluence areas of the southern tributaries. This indicates tributaries markedly out of balance, with limited mass supply by ice flow in their lowest reaches. The difference between thinning of the lower Loket tributary and the main branch at the same elevation is particularly distinctive (Figures 3.4a, 3.5a) and likely related to the unique quiescent phase dynamics of Black Rapids Glacier. As hypothesized in previous work (Heinrichs et al., 1996), the entering Loket tributary may modify ("dam") the ice flow in the main branch above the confluence, such that the elevation changes in the main branch are more positive than in the Loket tributary (this pattern would be reversed during the surge).

The different thinning rates of the Loket tributary and main branch are also reflected in the altimetry-derived elevation changes, with differences most pronounced over the 15 year period 1995–2010 (Figure 3.6a). Over the course of the time series, the thinning of the main branch just above the Loket confluence (around ~1400–1500 m a.s.l., Figure 3.6e) increased, which may be related to changes in both surface mass balance and ice flow dynamics. While it is difficult to delineate the boundary between the surge reservoir and receiving area, the main branch above the Loket tributary (above ~1400 m a.s.l.) is likely part of the reservoir area (Heinrichs et al., 1996). The laser-derived elevation changes (Figure 3.6e) thus indicate depletion of the surge reservoir rather than the dynamic thickening expected of a healthy surge-type glacier. This contrasts with the thickening observed over the preceding time period 1949–1995 (Shugar et al., 2010). Although we lack elevation change information for the highest reaches of the main branch, these observations question whether Black Rapids Glacier is accumulating sufficient mass to surge in the near future.

3.8.1.2 Sub-seasonal changes

Figure 3.6d gives insights into the short-term elevation changes of Black Rapids Glacier, with the two elevation datasets compared taken approximately one month apart (May vs. June, Table 3.1). Thinning due to melt, partly offset by flow emergence, is evident in the lowest clean-ice glacier reaches. Across the rockslides, the elevation changes are negligible. Towards the higher glacier reaches, the thinning increases again, likely due to the increasing submergence velocities, which offset the decreasing thinning due to melt. The latter interpretation assumes negligible penetration of the X-band radar, which is plausible, given the prevalent ice and wet snow surface in late June.

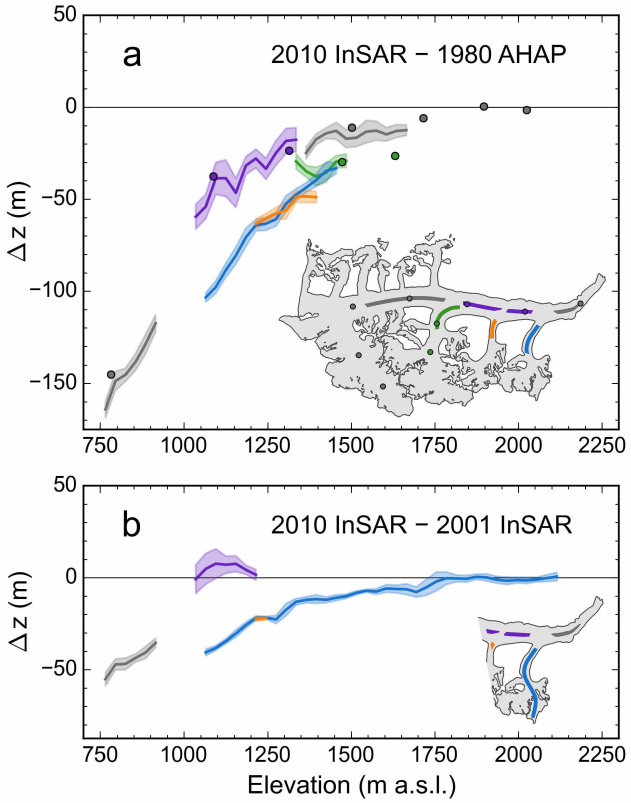

Figure 3.5: Δz vs. elevation (year 2010) sampled from the elevation change maps shown in Figure 3.4a–b. Bold lines show the mean thinning per 30 m elevation bin (without Kaiser filter application), while semi-transparent areas indicate the corresponding standard deviations. The color-coded dots in (a) show the differences between the 1980 index site elevations and the 2010 InSAR DEM. Their location is given in the inset map, along with the sampling areas used to derive the Δz vs. elevation curves. The sampling areas are different between (a) and (b) due to the different extents of the Δz grids. Note that we excluded areas with translated features (looped moraines, start/end of slide deposits), which introduced noise into the Δz curves.

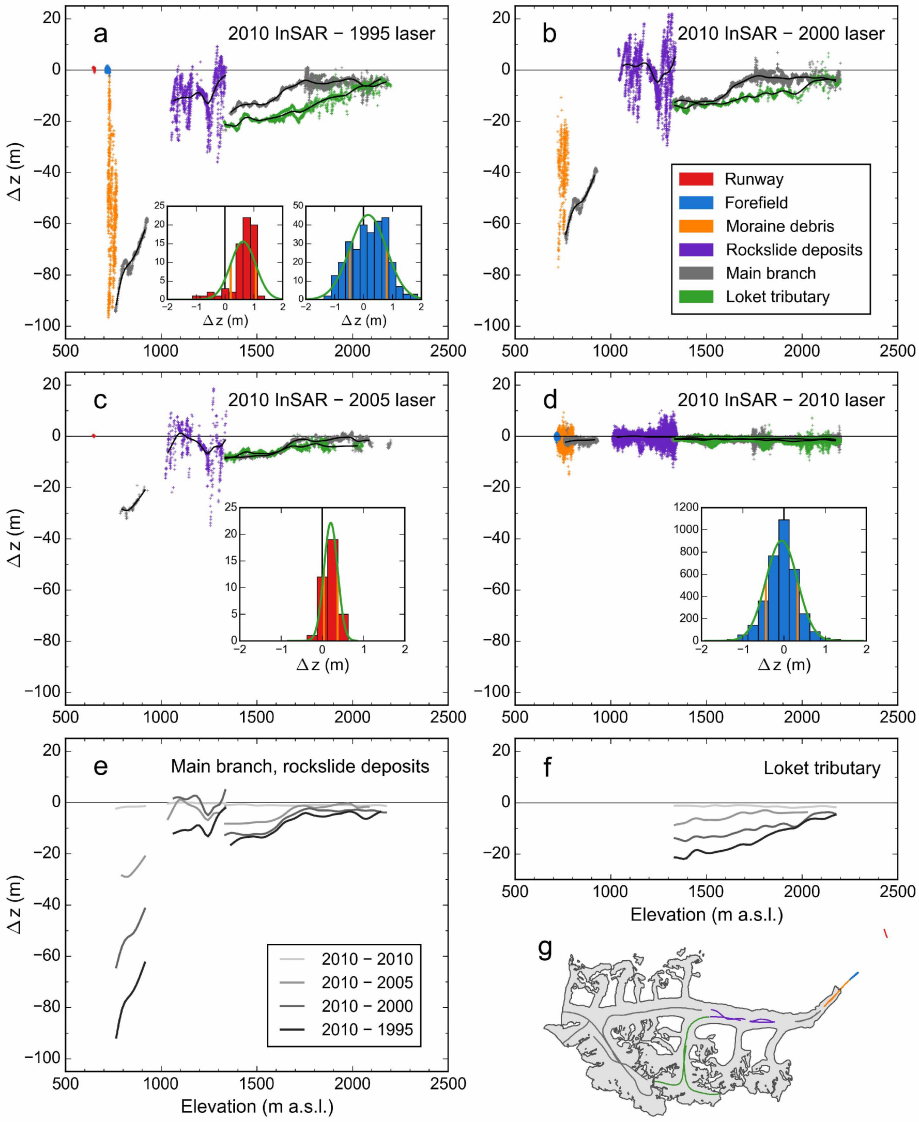

Figure 3.6: (a–d) Elevation differences along the laser altimetry profiles, between date of the survey and date of the 2010 InSAR DEM. In the case where the laser altimetry data was taken pre-earthquake (a–b), we used the earthquake-corrected 2010 InSAR DEM for reference. Black lines indicate the smoothed mean elevation changes per 15 m elevation bin (after Kaiser filter application), while the point clouds show the Δz values per 10 m grid cell covered by altimetry (color-code is given in (b)). The inset histograms show elevation differences over stable terrain, indicating a very good match between the two 2010 datasets (d). In the case of the 1995 data (a), differences are small in the glacier forefield, but slightly larger at the runway, possibly because of an imperfect earthquake displacement correction. (e) Smoothed Δz curves along the main branch and (f) the Loket branch for the four 5-year periods between 1995 and 2010. (g) Laser altimetry profiles surveyed in 1995, color-coded to match the point cloud colors.

3.8.2 Rockslide volumes

The three slides investigated released a total volume of 56.62 $\pm$ 2.86 $\times 10^6$ m^3, with the largest slide R-middle (25.73 $\pm$ 2.01$\times 10^6$ m^3) nearly three times as large as R-west (8.61 $\pm$ 1.31$\times 10^6$ m^3, Figure 3.7a). The mean elevation changes at scarp level range between 51.4 $\pm$ 3.1 m (R-east), 54.3 $\pm$ 8.2 m (R-west) and 75.8 $\pm$ 6.3 m (R-middle), with maximum changes up to 140 m at R-east and R-middle (Figure 3.8a). The crowns of all three scarps reach beyond the former ridgelines. The slides R-east and R-west removed the glacierets in the scarp areas completely (Figure 3.8c–d). Volume-area scaling-derived ice fractions correspond to ~5% (R-east), 0% (R-middle) and 17% (R-west) of the triggered slide volumes. Across the three slides, the computed ice fraction is ~5%. Because scaling coefficients vary considerably among glaciers, these ice fractions are approximate only. The mean deposit thicknesses (derived from dividing each rockslide release volume by its deposit area on the glacier) range between 2.82 $\pm$ 0.43 m at R-west and 5.82 $\pm$ 0.47 m at R-middle (Figure 3.7b). The debris would be 4.44 $\pm$ 0.24 m thick if spread evenly across the three deposit areas. The presence of voids in the rockslide deposits would further increase deposit thickness, while melting of ice within the deposits would decrease thickness.

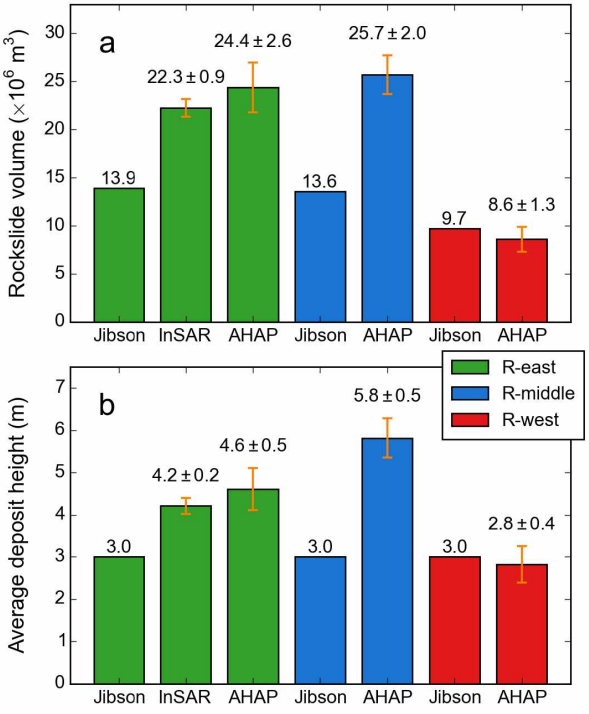

Figure 3.7: Bar plots showing our 1980 AHAP- and 2001 InSAR-derived estimates of Black Rapids' rockslide volumes and mean deposit heights, along with the estimates of Jibson et al. (2006). Error bars indicate the 1-σ uncertainties.

We find a total rockslide volume that is ~50% higher than the 37.2×10^6 m^3 estimated by Jibson et al. (2006). While their volume estimate for R-west is close to ours (within error bounds), our volumes are considerably larger for R-middle and R-east, with our 1-σ error bounds outside their estimates (Figure 3.7a). This suggests their average thickness estimate (3 m across all three deposits) was too conservative. Differencing our highest-quality InSAR DEMs across R-east resulted in an average deposit thickness of 4.22 $\pm$ 0.19 m, lending support to this assumption. Even if we subtracted the ice fraction (~5%) from our total rockslide volume estimate, our estimate would exceed that of Jibson et al. (2006). Shugar and Clague (2011) conducted fieldwork on deposit R-west in 2007, estimating its mean debris thickness to be 2–3 m, which agrees with our estimate of 2.82 $\pm$ 0.43 m. They adopted these numbers for the two remaining slides without ground-truthing (D. Shugar, personal communication, 2015), so our higher estimates are not unexpected.

The three rockslides are the largest of a series of rockslides, rockfalls and ice avalanches that occurred around Black Rapids as a result of the earthquake (Jibson et al., 2006). Given their much smaller volumes, these other events are difficult to locate and quantify based on the AHAP-derived elevation change grid. Interestingly, for the glacieret next to R-west, the AHAP-derived elevation change grid indicated an atypical thinning pattern with greatest thinning in the upper reaches (Figure 3.8a). Visual inspection of the satellite imagery (Figure 3.8c–d) suggests this glacieret was subject to a large ice avalanche that sheared off most of its upper reaches, leaving the terminus intact.

3.8.3 Earthquake-related displacements

The 2002 earthquake along the Denali Fault separated Black Rapids Glacier into a northern block with movement predominantly to the east and a southern block with movement predominantly to the west (Figure 3.9a). The northern block (including Black Rapids' terminus area) also gained in elevation, while the southern block (including large parts of Black Rapids' accumulation area) dropped (Figure 3.9c). Figure 3.9d visualizes the net elevation changes based on the elevation differences (Δz) between the original and the displacement-corrected 2010 InSAR DEM. Across the relatively flat glacierized area, the Δz values ranged between approximately –2.5 and +2.5 m, with a glacier-wide median and mean of –0.31 and –0.22 m, respectively (Figure 3.9e). This corresponds to a glacier-wide apparent volume change of -53.1×10^6 m^3 due to the earthquake, which, if not accounted for, would cause overestimation of the actual volume loss.

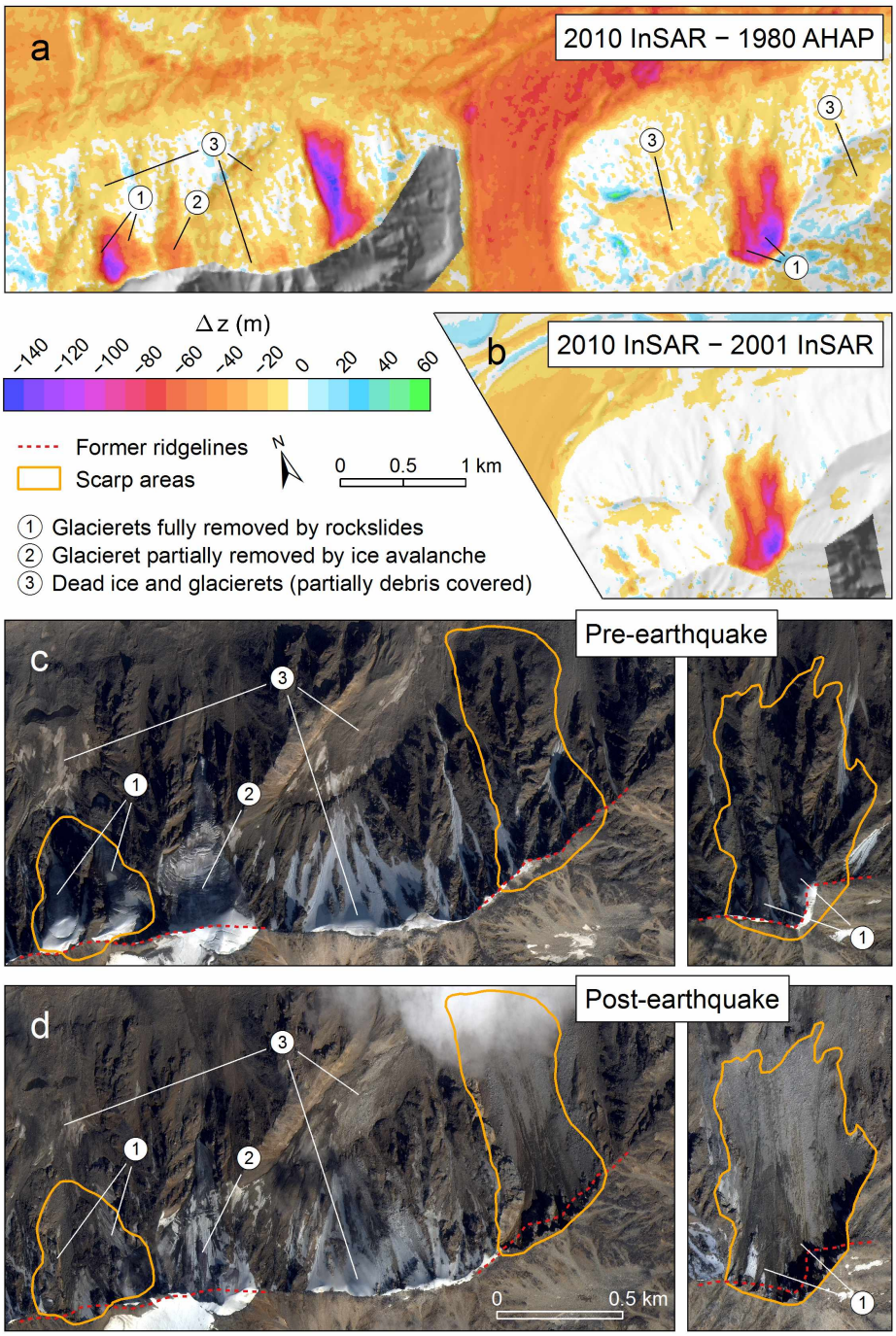

Figure 3.8: (a–b) Elevation change maps of the rockslide areas. The 2001 InSAR DEM covers only R-east, hence map (b) is incomplete. (c–d) IKONOS orthoimagery taken four months before and ~eight years after the rockslides (© 2011, DigitalGlobe, Inc.). Glacierets were present in R-west and R-east before the rockslides occurred, but vanished completely during the earthquake. The glacier annotated with 2 was likely subject to an ice avalanche. Note the backward movement of the ridgelines, particularly for sites R-east and R-middle.

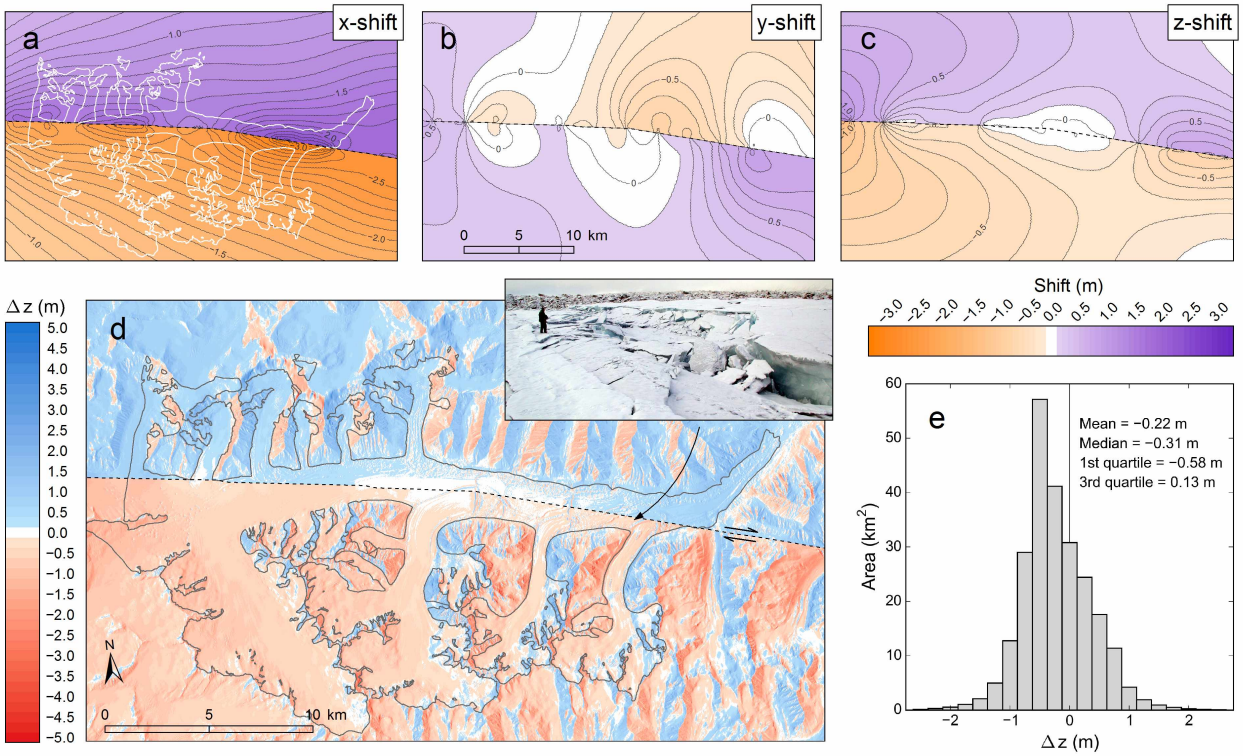

Figure 3.9: (a–c) Earthquake displacements (Elliott et al., 2007) converted to Alaska Albers x, y and z-shifts. 0.1 m contours and fault line are given for reference. Map (a) also contains the 2010 outlines of Black Rapids Glacier. (d) Net elevation changes due to the earthquake, visualized by differencing the original 2010 InSAR DEM and the displacement-corrected 2010 InSAR DEM. The corrected DEM had the shifts shown in (a–c) applied in the negative direction. For better readability, the color bar is bracketed between –5 and 5 m, although the Δz values lie outside this range in steep terrain. The shaded-relief-like appearance of the Δz grid is due to the large horizontal displacements, which alter the Δz signal as a function of slope angle and aspect. The inset photograph shows the ruptured glacier surface a few days after the earthquake. Note the person for scale, and the rockslide deposits of R-west in the background. Photo courtesy of USGS (http://earthquake.usgs.gov/earthquakes/eqinthenews/2002/uslbbl/photos/pr071102/new/PB090052.JPG). (e) Histogram of elevation changes across the glacier perimeter using a 0.25 m bin size. On average, the glacier surface dropped 0.22 m during the earthquake.

3.8.4 Geodetic mass balance

3.8.4.1 Volume and mass changes

Black Rapids' ice volume decreased by 4.15 ± 0.52×10^9 m^3 over the period 1980–2010, which corresponds to a mass loss of 3.53 ± 0.50 Gt (Figure 3.10a). The specific mass balance is –0.57 ± 0.07 m a^{-1} (ice equivalent) or –0.48 ± 0.07 m w.e. a^{-1} (Figure 3.10b). It is more negative for the 2001–2010 period (–0.64 ± 0.11 m w.e. a^{-1}) than for the 1980–2001 period (–0.42 ± 0.11 m w.e. a^{-1}), likely due to the record warm summer of 2004 (Truffer et al., 2005). The increased thinning in the more recent period occurred despite the 2002 rockslides, which reduced ice melt considerably across 11.7 km^2 (4.9%) of Black Rapids' lowest-lying area.

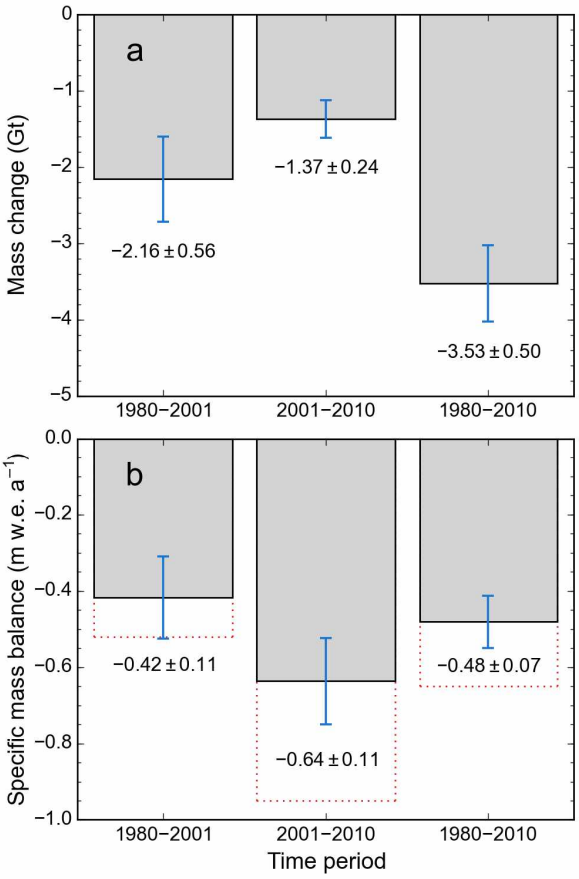

Figure 3.10: (a) Glacier-wide geodetic mass balances and (b) corresponding specific mass balances for the periods 1980–2001, 2001–2010 and the full period 1980–2010. Error bars show the 1-σ uncertainties. The red dotted bars in (b) indicate the more negative specific mass balances of nearby Gulkana Glacier (O'Neel et al., 2014).

Compared to the positive mass balance rate (+0.31 ± 0.13 m w.e. a^{-1}) for the period ~1949 to 1995 found by Arendt et al. (2002), our recent thinning rates are markedly negative, adding doubts

to whether Black Rapids will reach the required pre-surge geometry under the current climate. In-situ surface mass balance observations are in line with this interpretation (Figure 3.11). The annual balances at the index sites 8 and 14 km have exhibited increasingly negative trends over recent years, which in the case of site 8 km initiated the shift from the accumulation to the ablation area. The corresponding surface elevations, switching from elevation gain to loss around the year 1995, indicate the build up of the surge reservoir had ceased, in line with our laser altimetry-derived conclusions.

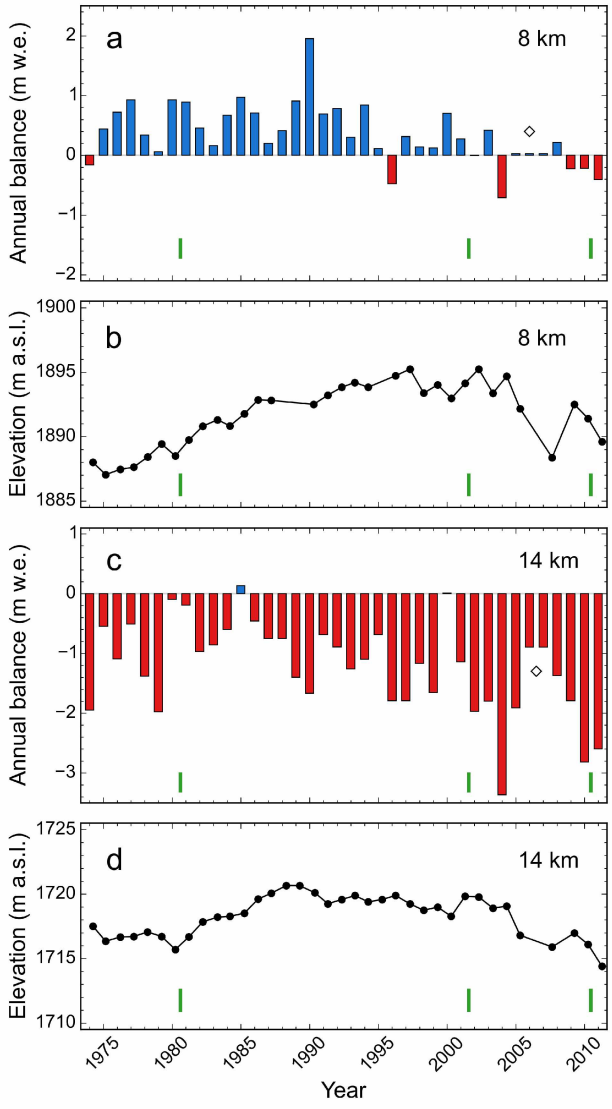

Figure 3.11: Annual surface mass balances and elevation changes measured at the index sites 8 km (a–b) and 14 km (c–d). Diamond shapes in (a) and (c) indicate where the annual balances correspond to multiyear averages (2005–2007 in the case of 8 km and 2006–2007 in the case of 14 km). Green bars show the dates of the DEMs (1980, 2001 and 2010).

3.8.4.2 Effect of rockslide deposits and earthquake displacements

The apparent glacier volume changes due to the earthquake shifts (-53.1×10^6 m^3) and rockslide deposits (56.6×10^6 m^3) are equivalent to specific mass balances of approximately –0.19 and +0.20 m w.e., which in turn are ~38 and 41% of Black Rapids' long-term (1980–2010) annual specific mass balance. The effects of these onetime processes decrease as the period of interest becomes longer. For example, in the case of Black Rapids Glacier, they would bias the long-term (30 year) geodetic mass balance by only 1.3 and 1.4% if not taken into account. Coincidentally, the two processes have similar volumes but opposite signs, so neglecting both processes would have yielded nearly identical geodetic mass balances in this specific case.

3.8.5 Comparison to nearby Gulkana Glacier

Gulkana Glacier is a non-surge-type USGS benchmark glacier located ~40 km to the southeast of Black Rapids Glacier (Figure 3.1). Ideally, benchmark glaciers represent an entire glacierized region (e.g., Mayo and Trabant, 1986; Echelmeyer et al., 1996), which motivates a comparison between Black Rapids' and Gulkana Glacier's mass balances. Similar to Black Rapids, Gulkana Glacier has shown increasingly negative mass balances since 1980 (O'Neel et al., 2014). However, its specific mass balances are more negative than those of Black Rapids, with a greater difference over the period 2001–2010 than 1980–2001 (Figure 3.10b). We examined potential geometric and climatic controls for the different thinning rates of the two glaciers (Table 3.2). Gulkana Glacier is much smaller (by factor 14) and covers a more limited elevation range (by factor 2.3) than Black Rapids Glacier. The two glaciers have identical median elevations, but Gulkana Glacier has a slightly more compact hypsometry with a larger area fraction around the median elevation. The orientation of the two glaciers is nearly opposite, with Gulkana Glacier facing to the south. The climatology-derived summer temperatures at Gulkana Glacier exceed those at Black Rapids by 1.7°C (Table 3.2), while the precipitation at the two glaciers is similar (~6% higher at Gulkana Glacier). Finally, Gulkana Glacier's fractional debris cover is only half that of Black Rapids. Except for the slightly increased winter precipitation at Gulkana Glacier, our parameters controlling mass balance (summer temperature, debris cover, aspect) favor more negative balances at Gulkana Glacier, in agreement with observations (Figure 3.10b). The fact that the discrepancies between the glaciers' specific mass balances increased over time (Figure 3.10b) is most likely related to the 2002 rockslide deposits, which increased Black Rapids' debris cover (and thus decreased its melt) abruptly.

Table 3.2: Characteristics of Gulkana and Black Rapids Glaciers derived from the Alaska-wide inventory (Kienholz et al., 2015) and partially updated with results from this study

Glacier	**Area**	**Elevation range**	**Median elevation**	**Debris cover**	**Aspect**	**Temperature**[a]	**Precipitation**[b]
	km^2	**m a.s.l.**	**m a.s.l.**	**%**		**°C**	**mm**
Gulkana	17.6	1160–2430	1860	9	S	+3.8	139
Black Rapids	241.5	720–3640	1850	18[c]	NE	+2.1	131

[a] Temperatures at 1850 m a.s.l., averaged over the summer months (May–September). Derived from the PRISM climatology (Daly et al., 1994).

[b] Monthly precipitation sums at 1850 m a.s.l., averaged over the winter months (October–April). Derived from the PRISM climatology (Daly et al., 1994).

[c] Including 2002 rockslide deposits.

3.9 Conclusions

We used DEMs, laser altimetry data and in-situ observations to quantify the geodetic mass balances of Black Rapids Glacier for the periods 1980–2001–2010. We found a mass loss of 3.53 ± 0.50 Gt over the entire 30 year period, with increased thinning rates over the period 2001–2010 (–0.64 ± 0.11 m w.e. a^{-1}) compared to 1980–2001 (–0.42 ± 0.11 m w.e. a^{-1}). The glacier currently fails to thicken its reservoir area, likely due to the warming climate. Given prevailing climate trends, a future surge appears unlikely.

Differencing pre- and post-slide DEMs over the scarp areas, we derived the volumes of the three large rockslides triggered by the 2002 M 7.9 Denali earthquake. We obtained a total volume of 56.62 ± 2.86×10^6 m^3, which exceeds previous estimates by ~50%. Our results indicate that the mean debris thicknesses differ considerably among the three deposits, ranging from ~2.8 to 5.8 m. The rockslide deposits caused an apparent thickening of ~0.20 m w.e. across the entire glacier, which highlights that rockslides can bias geodetic mass balances considerably, especially if the period of interest is short and/or the glacier change small. In addition to the rockslides, we accounted for the terrain displacements caused by the 2002 Denali earthquake. This earthquake caused an apparent thinning of ~0.19 m w.e. across the entire glacier. With the Denali fault running through the glacier, positive Δz values to the north of the fault compensated partly for their negative equivalents to the south. Such compensation did not occur for all the glaciers along the fault, so biases may be more severe on other glaciers. Pending availability of 3-D displacement fields, the correction method used in this study is applicable to earthquake displacements elsewhere. Given increasingly accurate terrain surveys pre- and post-earthquake, sophisticated algorithms for displacement detection (e.g., scale-invariant feature transform), and 3-D modeling, such displacement fields may become more commonly available in the future.

Difficulties in deriving suitable ground control points had previously hampered the use of the 1980 AHAP collection. We derived these points from modern orthorectified satellite imagery and corresponding DEMs, yielding useful DEMs and orthomosaics where the imagery had sufficient contrast. Using the simultaneously obtained near-infrared rather than the panchromatic AHAP imagery (1.6 vs. 3.2 m spatial resolution) could further improve the quality of the derived products, in particular by facilitating the derivation of additional ground control points. Using only satellite orthoimagery from the most recent generation (e.g., WorldView-3 rather than IKONOS) would improve the positional accuracy of the ground control points, contributing to higher quality products as well. Lack of contrast in snow-covered areas remains problematic, and will continue to impede derivation of glacier-wide mass balances from AHAP imagery alone. Combination with auxiliary elevation data, as done in this study, will thus remain required to obtain glacier-wide mass balances.

With its many spatially variable error sources, this mass balance project was well suited for the application of a Monte Carlo error analysis. Monte Carlo simulations allow for taking into account all the error sources systematically, including those that cannot be covered by error propagation equations (e.g., errors in the glacier outlines). Our Monte Carlo workflow still has potential for improvement. For example, the elevation errors' spatial correlation is implemented in a simplified manner currently. Also, our project did not investigate the individual error sources' contributions to the final error (e.g., bulk density uncertainty vs. outline uncertainty), which could be an interesting aspect of future work.

The present observation-based study should be complemented by glacier modeling to ascertain our conclusions regarding surge likelihood. A combined mass balance-ice flow model would allow for projecting Black Rapids' evolution in response to future climate scenarios. It could also shed light on the glacier's past evolution at better temporal and spatial resolution than is possible based on observations alone. Targeted sensitivity experiments could be designed to quantify the effects of rockslide deposition on glacier mass balance. For proper model calibration, field observations are crucial. The current monitoring program should thus be continued, and ideally expanded, for example, with air temperature and precipitation measurements at the glacier, and measurements of debris thicknesses and temperatures, which would allow for a sophisticated melt model calibration.

3.10 Acknowledgements

We thank J. Freymueller for running the earthquake displacement model in our domain specifically, A. Gardner for providing DEM coregistration code, and D. Shugar for sharing photographs from the field. C. Reim is acknowledged for support regarding the satellite imagery, C. Larsen for the laser altimetry data, and A. Aschwanden for helpful discussions throughout the project. K. Echelmeyer, M. Stuefer, and R. Flanders were instrumental in maintaining the mass balance program on Black Rapids Glacier. Detailed reviews by D. Shugar, D. Alexander and B. Rabus strengthened the paper. Except for the high-resolution spaceborne imagery (available for purchase from DigitalGlobe), all data for this paper is available for free, with references provided in Sections 3.5 and 3.6. This work was funded by grants from the National Science Foundation (NSF, OPP-1107491), the National Aeronautics and Space Administration (NASA, NNX11AF41G) and the U.S. Department of the Interior Climate Science Center. C. Kienholz was also funded by a fellowship from the University of Alaska Fairbanks Graduate School. A. Arendt acknowledges funding from NASA Cryospheric Sciences (grant NNX13AD52A), the Washington Research Foundation Fund for Innovation in Data-Intensive Discovery and the Moore/Sloan Data Science Environments Project at the University of Washington.

References

Amundson, J. M., M. Truffer, and M. P. Lüthi (2006). Time-dependent basal stress conditions beneath Black Rapids Glacier, Alaska, USA, inferred from measurements of ice deformation and surface motion. *Journal of Glaciology 52*(178), 347–357.

Arendt, A. A., K. A. Echelmeyer, W. D. Harrison, C. S. Lingle, and V. B. Valentine (2002). Rapid wastage of Alaska glaciers and their contribution to rising sea level. *Science 297*(5580), 382–386.

Bahr, D. B., M. F. Meier, and S. D. Peckham (1997). The physical basis of glacier volume-area scaling. *Journal of Geophysical Research 102*(B9), 20355–20362.

Berthier, E., E. Schiefer, G. K. C. Clarke, B. Menounos, and F. Rémy (2010). Contribution of Alaskan glaciers to sea-level rise derived from satellite imagery. *Nature Geoscience 3*, 92–95.

Bevington, A. and L. Copland (2014). Characteristics of the last five surges of Lowell Glacier, Yukon, Canada, since 1948. *Journal of Glaciology 60*(219), 113–123.

Cogley, J. G., R. Hock, L. A. Rasmussen, A. A. Arendt, R. J. Bauder, A.and Braithwaite, P. Jansson, G. Kaser, M. Möller, L. Nicholson, et al. (2011). Glossary of glacier mass balance and related terms. *IHP-VII Technical Documents in Hydrology 86*.

Cox, L. H. and R. S. March (2004). Comparison of geodetic and glaciological mass-balance techniques, Gulkana Glacier, Alaska, USA. *Journal of Glaciology 50*(170), 363–370.

Daly, C., R. P. Neilson, and D. L. Phillips (1994). A Statistical-Topographic Model for Mapping Climatological Precipitation over Mountainous Terrain. *Journal of Applied Meteorology 33*(2), 140–158.

Das, I., R. Hock, E. Berthier, and C. S. Lingle (2014). 21st-century increase in glacier mass loss in the Wrangell Mountains, Alaska, USA, from airborne laser altimetry and satellite stereo imagery. *Journal of Glaciology 60*(220), 283–293.

Dowdeswell, J., R. Hodgkins, A. Nuttall, J. Hagen, and G. Hamilton (1995). Mass balance change as a control on the frequency and occurrence of glacier surges in Svalbard, Norwegian High Arctic. *Geophysical Research Letters 22*(21), 2909–2912.

Echelmeyer, K., W. Harrison, C. Larsen, J. Sapiano, J. Mitchell, J. DeMallie, B. Rabus, G. Adalgeirsdottir, and L. Sombardier (1996). Airborne surface profiling of glaciers: a case-study in Alaska. *Journal of Glaciology 42*(142), 538–547.

Eisen, O., W. Harrison, and C. Raymond (2001). The surges of Variegated Glacier, Alaska, USA, and their connection to climate and mass balance. *Journal of Glaciology 47*(158), 351–358.

Elliott, J. L., J. T. Freymueller, and B. Rabus (2007). Coseismic deformation of the 2002 Denali fault earthquake: contributions from synthetic aperture radar range offsets. *Journal of Geophysical Research: Solid Earth (1978–2012) 112*(B6), B06421.

Fatland, D. R., C. S. Lingle, and M. Truffer (2003). A surface motion survey of Black Rapids Glacier, Alaska, U.S.A. *Annals of Glaciology 36*(1), 29–36.

Finsterwalder, R. (1954). Photogrammetry and glacier research with special reference to glacier retreat in the eastern Alps. *Journal of Glaciology 2*, 306–315.

Flowers, G., N. Roux, S. Pimentel, and C. Schoof (2011). Present dynamics and future prognosis of a slowly surging glacier. *The Cryosphere 5*(1), 299–313.

Frappé, T.-P. and G. K. C. Clarke (2007). Slow surge of Trapridge Glacier, Yukon Territory, Canada. *Journal of Geophysical Research 112*(F3), F03S32.

Gades, A. M., C. F. Raymond, and H. Conway (2012). Radio-echo probing of Black Rapids Glacier, Alaska, USA, during onset of melting and spring speed-up. *Journal of Glaciology 58*(210), 713–724.

Gardelle, J., E. Berthier, and Y. Arnaud (2012). Impact of resolution and radar penetration on glacier elevation changes computed from DEM differencing. *Journal of Glaciology 58*(208), 419–422.

Hance, J. H. (1937). The recent advance of Black Rapids Glacier, Alaska. *The Journal of Geology*, 775–783.

Harrison, W. D. and A. S. Post (2003). How much do we really know about glacier surging? *Annals of Glaciology 36*, 1–6.

Hartmann, D., A. Klein Tank, M. Rusicucci, L. Alexander, B. Broenniman, Y. Charabi, F. Dentener, E. Dlugokencky, D. Easterling, A. Kaplan, et al. (2013). *Climate Change 2013: The Physical Science Basis*, Chapter Observations: Atmosphere and Surface. Cambridge University Press.

Heid, T. and A. Kääb (2012). Repeat optical satellite images reveal widespread and long term decrease in land-terminating glacier speeds. *The Cryosphere 6*(2), 467–478.

Heinrichs, T., L. Mayo, D. Trabant, and R. March (1995). Observations of the surge-type Black Rapids Glacier, Alaska, during a quiescent period, 1970–92. Open-file report 94-512, U.S. Geological Survey.

Heinrichs, T. A., L. Mayo, K. Echelmeyer, and W. Harrison (1996). Quiescent-phase evolution of a surge-type glacier: Black Rapids Glacier, Alaska, USA. *Journal of Glaciology 42*(140), 110–122.

Hoinkes, H. C. (1969). Surges of the Vernagtferner in the Ötztal Alps since 1599. *Canadian Journal of Earth Sciences 6*(4), 853–861.

Huss, M. (2013). Density assumptions for converting geodetic glacier volume change to mass change. *The Cryosphere 7*(3), 877–887.

Huss, M. and D. Farinotti (2012). Distributed ice thickness and volume of all glaciers around the globe. *Journal of Geophysical Research 117*(F4), F04010.

Jibson, R. W., E. L. Harp, W. Schulz, and D. K. Keefer (2006). Large rock avalanches triggered by the M 7.9 Denali Fault, Alaska, earthquake of 3 November 2002. *Engineering Geology 83*(1), 144–160.

Johnson, A. J., C. F. Larsen, N. Murphy, A. A. Arendt, and S. L. Zirnheld (2013). Mass balance in the Glacier Bay area of Alaska, USA, and British Columbia, Canada, 1995–2011, using airborne laser altimetry. *Journal of Glaciology 59*(216), 632–648.

Kienholz, C., S. Herreid, J. Rich, A. Arendt, R. Hock, and E. Burgess (2015). Derivation and analysis of a complete modern-date glacier inventory for Alaska and northwest Canada. *Journal of Glaciology 61*(227), 403–420.

Larsen, C. (2010). IceBridge UAF Lidar Scanner L1B Geolocated Surface Elevation Triplets, NASA National Snow and Ice Data Center Distributed Active Archive Center, Boulder, Colorado.

Larsen, C., E. Burgess, A. Arendt, S. O'Neel, A. Johnson, and C. Kienholz (2015). Surface melt dominates Alaska glacier mass balance. *Geophysical Research Letters 42*(14), 5902–5908.

Le Bris, R. and F. Paul (2015). Glacier-specific elevation changes in parts of western Alaska. *Annals of Glaciology 56*(70), 184–192.

Mayo, L. and D. Trabant (1986). Recent growth of Gulkana Glacier, Alaska Range, and its relation to glacier-fed river runoff. *U.S. Geological Survey Bulletin*, 91–99.

Motyka, R. J., M. Fahnestock, and M. Truffer (2010). Volume change of Jakobshavn Isbræ, West Greenland: 1985–1997–2007. *Journal of Glaciology, 56*(198), 635–646.

Nolan, M. (2003). The "Galloping Glacier" trots: decadal-scale speed oscillations within the quiescent phase. *Annals of Glaciology 36*, 7–13.

Nuth, C. and A. Kääb (2011). Co-registration and bias corrections of satellite elevation data sets for quantifying glacier thickness change. *The Cryosphere 5*(1), 271–290.

O'Neel, S., E. Hood, A. Arendt, and L. Sass (2014). Assessing streamflow sensitivity to variations in glacier mass balance. *Climatic Change 123*(2), 329–341.

Paul, F., N. E. Barrand, S. Baumann, E. Berthier, T. Bolch, K. Casey, H. Frey, S. P. Joshi, V. Konovalov, R. Le Bris, N. Mölg, G. Nosenko, C. Nuth, A. Pope, A. Racoviteanu, P. Rastner, B. Raup, K. Scharrer, S. Steffen, and S. Winsvold (2013). On the accuracy of glacier outlines derived from remote-sensing data. *Annals of Glaciology 54*(63), 171–182.

Rabus, B. and D. Fatland (2000). Comparison of SAR-interferometric and surveyed velocities on a mountain glacier: Black Rapids Glacier, Alaska, USA. *Journal of Glaciology 46*(152), 119–128.

Raymond, C. (1987). How do glaciers surge? A review. *Journal of Geophysical Research 92*(B9), 9121–9134.

Rolstad, C., T. Haug, and B. Denby (2009). Spatially integrated geodetic glacier mass balance and its uncertainty based on geostatistical analysis: application to the western Svartisen ice cap, Norway. *Journal of Glaciology 55*(192), 666–680.

Sevestre, H. and D. I. Benn (2015). Climatic and geometric controls on the global distribution of surge-type glaciers: implications for a unifying model of surging. *Journal of Glaciology 61*(228), 646–662.

Shugar, D. H. and J. J. Clague (2011). The sedimentology and geomorphology of rock avalanche deposits on glaciers. *Sedimentology 58*(7), 1762–1783.

Shugar, D. H., B. T. Rabus, and J. J. Clague (2010). Elevation changes (1949–1995) of Black Rapids Glacier, Alaska, derived from a multi-baseline InSAR DEM and historical maps. *Journal of Glaciology 56*(198), 625–634.

Shugar, D. H., B. T. Rabus, J. J. Clague, and D. M. Capps (2012). The response of Black Rapids Glacier, Alaska, to the Denali earthquake rock avalanches. *Journal of Geophysical Research: Earth Surface 117*(F1), F01006.

Truffer, M., K. A. Echelmeyer, and W. D. Harrison (2001). Implications of till deformation on glacier dynamics. *Journal of Glaciology 47*(156), 123–134.

Truffer, M., W. D. Harrison, and R. S. March (2005). Record negative glacier balances and low velocities during the 2004 heatwave in Alaska, USA: implications for the interpretation of observations by Zwally and others in Greenland. *Journal of Glaciology 51*(175), 663–664.

Wilson, F. H., J. H. Dover, D. C. Bradley, F. R. Weber, T. K. Bundtzen, and P. J. Haeussler (1998). *Geologic Map of Central (Interior) Alaska*. US Geological Survey.

Appendix 3.A Extension of the partial DEMs

For the extension of the partial DEMs, we distinguished the S1, S2 and Loket tributaries, as well as the main branch (Figure 3.1). We assumed the small northern tributaries (N1–N5, Melville) had the same elevation change as the main branch, due to lack of elevation change information for these tributaries.

Appendix 3.A.A 2001 InSAR DEM

The 2001 InSAR DEM has complete coverage of the terminus area and nearly complete coverage of branch S1 (Figure 3.4b). To extend the partial DEM, we applied the Δz vs. elevation curve of tributary S1 to tributary S2, assuming the two branches followed the same elevation change pattern. In the lower portions of S2 (where 2001 DEM coverage is available), the Δz values are very close to those of S1 at the same elevation (Figure 3.5b), lending support to this assumption.

The Loket tributary and the main branch were surveyed in 2000 by laser altimetry, so we used the corresponding 2000–2010 Δz vs. elevation curves (Figure 3.6b), corrected to account for the elevation change within the ~14 months' time difference. With the Loket tributary and the main branch having unique elevation changes, this approach appeared more appropriate than applying the Δz vs. elevation curve from S1.

Appendix 3.A.B 1980 AHAP DEM

Our approach largely followed the one for the 2001 DEM, however, to extend the partial DEM (~30% coverage) to the higher glacier reaches, we relied on sparse surface elevations surveyed in 1980. For the main branch, we used three elevations surveyed at the mass balance sites at 8, 11 and 14 km, from which we differenced the 2010 elevations to obtain the corresponding Δz values (Figure 3.5a). For the Loket tributary, we used one Δz value beyond the known Δz vs. elevation curve (at the mass balance site L-22 km). For the branches S1 and S2, no surveyed elevations were available. Assuming the shape of the 2001–2010 Δz vs. elevation curve of branch S1 represented the full period 1980–2010, we applied this curve to both branches S1 and S2, after accounting for the elevation changes within the ~21 years.

Appendix 3.A.C Uncertainties

Extending the partial DEMs introduced additional uncertainties, which we addressed as part of our Monte Carlo analysis (Section 3.7.2). The main uncertainties arose from: 1) applying centerline-derived elevation changes to the full width of the branch; 2) applying centerline elevation changes derived at one branch to another branch (or to the same branch but another time

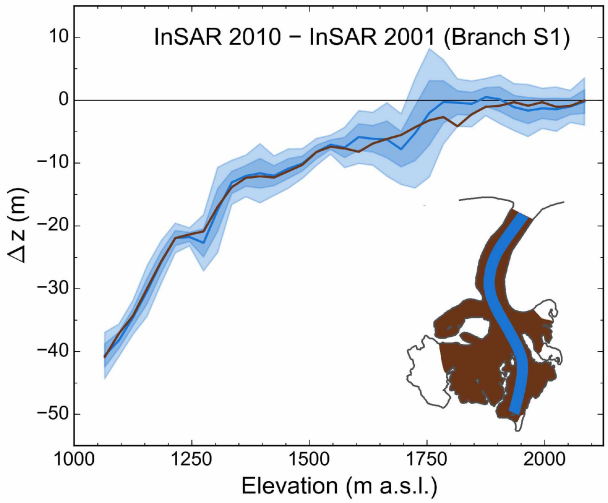

Figure 3.A.B-1: Mean elevation changes (2001–2010) for branch S1, derived from the two sampling areas (full-width and centerline) shown in the inset map. Bold lines indicate the mean Δz values per 30 m elevation bin, while semi-transparent areas show the corresponding spread for the centerline-derived elevation changes (mean ± 1 and ± 2 standard deviations).

period) and 3) applying Δz curves that did not cover the highest glacier reaches (i.e., no coverage $>$2250 m). Some residual bias between the compared elevation datasets (laser altimetry data vs. 2010 InSAR DEM, index site elevations vs. 2010 InSAR DEM), in addition to the non-systematic components listed in Table 3.1, cannot be ruled out, making up error source 4.

To address error source 1, we compared full-width to centerline elevation changes at branch S1, using the distributed 2001–2010 Δz grid (Figure 3.4b) as input. This comparison indicated full-width elevation changes (the reference values) mostly within one standard deviation of the centerline-derived Δz vs. elevation curves (Figure 3.A.B-1). We found no systematic elevation differences between the two curves, but differences that had some spatial autocorrelation across the elevation bins (i.e., if for one elevation bin the centerline-derived Δz value was higher than the corresponding full-width value, this was likely the same for the neighboring elevation bin). We transferred these observations to our workflow as follows. Once per Monte Carlo run, we sampled spatial correlation values (reflecting the numbers of spatially correlated elevation bins) from a uniform distribution bracketed between 3 and 30. Values for perturbing the original Δz values (e.g., +0.5 σ) were sampled at the lowest elevation bin initially and subsequently when the number of consecutive bins without sampling reached the spatial correlation value; otherwise, the value of the previous bin was applied.

Regarding source 2, we exploited the fact that the employed Δz vs. elevation curves overlapped with the partial DEM-derived Δz grids, which allowed computation of correction

factors by comparing the Δz values across the overlapping portions. Multiplying the Δz vs. elevation curve with the resulting factor moved the curve vertically to match the Δz values from the Δz grid. Note that we calculated the factors for each overlapping 30 m elevation bin separately, which provided an estimation of their variance. Every Monte Carlo run, we sampled one factor from this distribution to simulate the corresponding uncertainty.

For 3, we set Δz to approach zero between 2250 and 2750 m, sampling one elevation value per Monte Carlo run from this range. To obtain the final Δz curve, we linearly interpolated between the last Δz vs. elevation pair from the known Δz vs. elevation curve and zero at the elevation sampled. Above the elevation sampled, we assumed zero elevation changes. In their extended portions, the Δz vs. elevation curves had no standard deviations, which were required for further processing. For each bin, we sampled the standard deviations from a 0 ± 5 m Gaussian distribution.

Regarding error source 4, we allowed for a bias of 0 ± 0.5 m when differencing laser altimetry data from the 2010 InSAR DEM (based on the inset histograms of Figure 3.6) and 0 ± 2.5 m when differencing the 1980 index site elevations from the 2010 InSAR DEM. The potential bias for the index site elevations was chosen conservatively, as we had no means to check reliably for biases in this case.

Appendix 3.B Derivation of multiple outline versions

Manual digitization yielded outlines of the glacier for the years 1980, 2001 and 2010, as well as the three rockslide scarps R-east, R-middle and R-west. To estimate the uncertainty caused by digitizing errors, several realizations of each outline are required (e.g., Paul et al., 2013), however, in our case, it was impractical to derive more than 1 (glacier extents) and 5 (scarp extents) outline realizations by hand. To increase the number of outlines, we applied the following two-step procedure. First, we created a set of several hundred intermediate outlines by expanding or contracting (by distances up to 25 m), then simplifying and smoothing the original outlines. All the changes were applied along the entire outline length. In a second step, we modified these intermediate outlines further to allow for variable changes along the outlines. We initiated this step by dividing the domain of Black Rapids Glacier into a number of square subareas. For each subarea, we randomly chose one outline from the set of intermediate outlines derived in step 1 and extracted the portion covered by the subarea. The outline segments of each subarea were then combined to form a new glacier or scarp outline with variable changes along the outline. We ran this second step 500 times, randomly varying the number of the subareas (and thus their size) within a range of 1 and 400, thus simulating different degrees of spatial correlation of the outline changes. The resulting 500 outline versions went into the outline pool, which was later sampled during the Monte Carlo simulations.

Chapter 4

Mass balance evolution of Black Rapids Glacier, Alaska, 1980–2015–2100, and its implications for surge recurrence[1]

4.1 Abstract

Surge-type Black Rapids Glacier, Alaska, has undergone strong retreat since it last surged in 1936–37. To assess its evolution during the late 20th and 21st centuries, we run a coupled surface mass balance-glacier dynamics model over the periods 1980–2015 (hindcasting) and 2015–2100 (forecasting). The model is forced by daily temperature and precipitation fields, with downscaled reanalysis data used for the hindcasting. A constant climate scenario and an RCP 8.5 scenario based on the GFDL-CM3 climate model are employed for the forecasting. The debris evolution is accounted for through a debris layer time series derived from satellite imagery (hindcasting) and a simplified debris evolution model (forecasting). Model calibration and validation rely on geodetic and in situ mass balance observations as well as remotely sensed snowline elevations. Our results for the hindcasting period indicate a negative mass balance trend, both due to less positive winter and more negative summer balances. The net mass loss is caused by atmospheric warming and surface elevation lowering (climate-elevation feedback), which exceed the moderating effects from increasing debris cover and glacier retreat. Despite its retreat, Black Rapids Glacier is substantially out of balance with today's climate. By 2100, ~10 and 80% of Black Rapids' 2010 area are projected to vanish under the constant climate and RCP 8.5 scenarios, respectively. For both scenarios, the remaining glacier portions are out of balance, suggesting continued retreat after 2100. Due to mass starvation, a surge within the 21st century is unlikely, even for the constant climate scenario. The projected retreat will affect the glacier's runoff and change the landscape in the Black Rapids area markedly.

4.2 Introduction

Of the ~200,000 glaciers worldwide (Pfeffer et al., 2014), >2300 have been identified as surge-type glaciers (Sevestre and Benn, 2015). A large fraction thereof, >300 surge-type glaciers, lie in Alaska and neighboring Canada. Over the last decades, this region has been subject to strong warming (e.g., Bieniek et al., 2014), which is the main driver for the dramatic observed glacier mass losses (Arendt et al., 2009). Due to their unique dynamic behavior, surge-type glaciers complicate both observational (e.g., Larsen et al., 2015) and modeling studies (e.g., Radić et al., 2014) that aim to constrain their response to warming. This provides an incentive for improved observation and modeling of surge-type glaciers.

[1] A version of this chapter is in preparation for submission to Frontiers in Earth Science.

In this paper, we focus on Black Rapids Glacier, a surge-type glacier in interior Alaska that last surged in 1936–37. While Black Rapids' surge reservoir experienced a net elevation gain from ~1950–1995 (Shugar et al., 2010), no net gain was observed over the period 1980–2010 (Kienholz et al., 2016), likely due to the warming atmosphere. Workers on other surge-type glaciers in the Alaska-Yukon region found that climate change prolonged surge recurrence intervals and/or attenuated surge magnitudes (Eisen et al., 2001; Flowers et al., 2011; Bevington and Copland, 2014). In the case of Black Rapids Glacier, Kienholz et al. (2016) hypothesized that a surge in the near future is unlikely.

Here we employ a surface mass balance model to reconstruct Black Rapids' mass balance for the period 1980–2015 and to project it for the period 2015–2100. Our goal is to assess the evolution of Black Rapids Glacier with a special focus on its surge likelihood. To model the surface mass balance, we use a distributed enhanced temperature index melt model forced with temperature and precipitation fields downscaled from the ERA-Interim reanalysis and calibrated with an extensive set of field measurements. A parametrized glacier dynamics model and a simple debris model are applied to incorporate the effects of ice flow and debris evolution, respectively.

4.3 Study site

Black Rapids Glacier is a surge-type valley glacier located in the western portion of the Eastern Alaska Range known as the Hayes Range (Figure 4.1a). In 2010, Black Rapids was 41.3 km long and occupied an area of 241.5 km^2, 44.5 km^2 of which were covered by moraine and rockslide debris (Figure 4.1b). The extensive rockslide debris (~11 km^2) was deposited during the M 7.9 Denali Fault earthquake in November 2002.

Black Rapids Glacier currently ranges from ~700–3650 m a.s.l., with its median elevation at ~1850 m. It has three southern and six smaller northern tributaries, and shares two major divides with the Susitna and East Fork Glaciers. Black Rapids is part of Alaska's Southeast Interior climate zone (Bieniek et al., 2012), where high latitude and marked continentality cause long cold accumulation and short warm ablation seasons. Only three months per year have glacier wide mean temperatures above freezing (Figure 4.1c). Monthly mean precipitation is typically ~100 mm, but reaches ~250 mm during the fall months (August–October).

During its last surge in 1936–37, Black Rapids reached a length of ~46.5 km. Over the recent decades, the glacier has been subject to considerable thinning and retreat. From 1980 to 2010, its length and area decreased from 42.7 to 41.3 km (–1.4 km) and 248.8 to 241.5 km^2 (–7.3 km^2), respectively (Kienholz et al., 2016). The corresponding specific mass balance was -0.48 ± 0.07 m w.e. a^{-1} for the entire period, and more negative for the period 2001–2010 (-0.64 ± 0.11 m w.e. a^{-1}) than the period 1980–2001 (-0.42 ± 0.11 m w.e. a^{-1}).

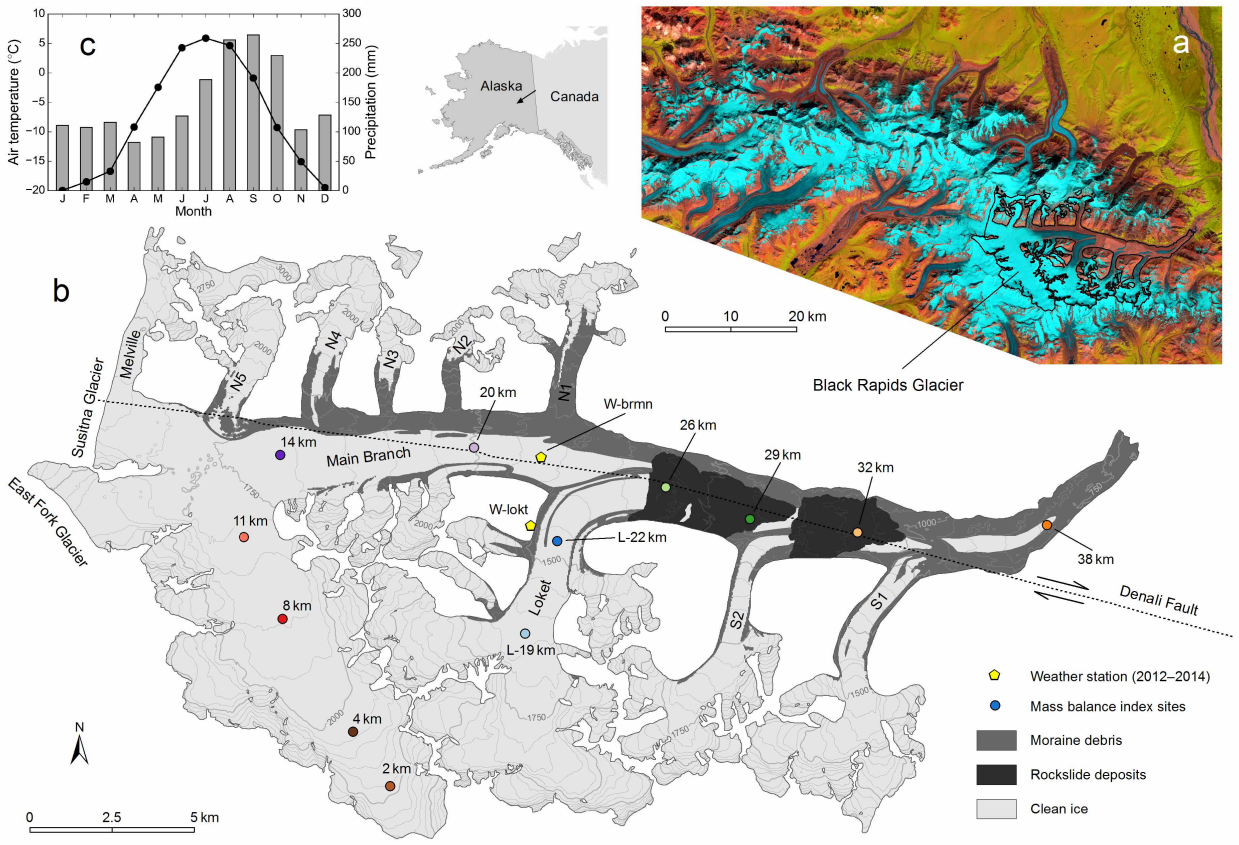

Figure 4.1: (a) Landsat Operational Land Imager (OLI) false color composite from July 13, 2013, showing Black Rapids Glacier along with the glaciers of the Hayes Range (western part of the Eastern Alaska Range). (b) Map of Black Rapids Glacier with glacier extent, surface topography, debris cover and rockslide deposits for the year 2010. The locations of the mass balance index sites are labeled with stake names. The approximate location of the Denali Fault is also shown. (c) Monthly mean temperatures (dotted line) and total precipitation (bars) based on the Parameter-elevation Relationships on Independent Slopes Model (PRISM) climatology (Daly et al., 1994). The diagram was derived by averaging temperature and precipitation from all the PRISM grid points within Black Rapids' perimeter (62 points).

Black Rapids Glacier has been studied extensively over the past decades (see Kienholz et al. (2016) for a summary of the previous work). A surface mass balance monitoring program was initiated in 1972 by the U.S. Geological Survey (USGS), the University of Alaska Fairbanks and the University of Washington (Heinrichs et al., 1995). This ongoing program has resulted in extensive point observations (Heinrichs et al., 1995; Truffer et al., 2005), placing Black Rapids Glacier among Alaska's glaciers with most surface mass balance measurements. So far, however,

these point observations have not been used to estimate glacier wide mass balances or for mass balance modeling applications.

4.4 Data

For the forcing of the mass balance model, we used dynamically downscaled daily ERA-interim temperature and precipitation fields for the hindcasting period 1980–2015. Quantile mapped versions of these fields matching the GFDL-CM3 RCP 8.5 climate scenario, as well as a constant climate scenario, were used for the forecasting period 2015–2100. For calibration and validation of the surface mass balance model, we used in situ surface mass balance observations (point balances), geodetic mass balances and snowline elevations derived from satellite imagery. Glacier topography and ice thickness were taken from digital elevation models (DEMs) and a global ice thickness dataset, respectively. The glacier extent and debris cover input for the model were mapped from aerial and satellite imagery.

4.4.1 Outlines and DEMs

Outlines derived from high resolution aerial imagery (Alaska High Altitude Aerial Photography (AHAP), Brooks, 1988) and satellite imagery (IKONOS and Worldview-2, © 2011, DigitalGlobe, Inc.) were available for the years 1980, 2001 and 2010, enclosing glacier areas of 248.8, 243.1 and 241.5 km^2, respectively (Kienholz et al., 2016). For the same years, we had DEMs available. Most applications in this study relied on the 2010 DEM, which was derived from airborne InSAR (X-band) through interferometry (ifsar.gina.alaska.edu). This DEM has a native resolution and vertical precision of 5 and $\sim$1 m, respectively.

While the free running version of our glacier model required only initial glacier topography and extent, its calibration required annually updated outlines and DEMs. We prepared the DEM time series by linearly interpolating elevation changes between the DEMs available. For the outlines we chose a similar approach and linearly interpolated horizontal rates of change between the outlines available. Though this approach oversimplifies the true signal, it is closest to reality in the absence of additional observations. Note that Black Rapids' terminus is heavily debris covered, making frequent outline updates based on satellite imagery challenging.

4.4.2 Ice thicknesses/glacier bed

Ice thicknesses were extracted from a global dataset computed by Huss and Farinotti (2012). Their approach employs a parametrized surface mass balance gradient (adjusted for surface elevation change) to determine the volumetric balance flux along a glacier's elevation profile. Employing

Glen's flow law and a sliding parametrization, they solve the balance flux for an average ice thickness at each elevation band. Finally, using slope and distance to the glacier margin (derived from DEM and glacier outlines), they compute spatially distributed ice thicknesses from the longitudinal thickness profile.

For Black Rapids Glacier, Huss and Farinotti (2012) used a DEM from 2010 (identical to the 2010 InSAR DEM used in this study) and outlines compiled by Kienholz et al. (2015). To match the improved outlines used here, we adapted the ice thicknesses manually along the glacier margins. The results modeled (for the year 2010) suggest mean and maximum ice thicknesses of 210 m and 650 m, respectively. The corresponding volume is 49.9 km^3, equivalent to ~44.9 Gt of ice (assuming an ice density of 900 kg m^{-3}).

We used in situ ice thickness observations (Heinrichs et al., 1995; Gades, 1998) to assess the uncertainties of the ice thickness map. Gades (1998) obtained ice thicknesses in 1993 by ground-based low-frequency radio echo sounding (5 MHz), covering 12 profiles in the upper glacier area (Figure 4.2a). The thickness observations compiled in Heinrichs et al. (1995) were obtained by radio echo sounding also, however, they were taken mostly in spring 1990 and cover the lower part of the glacier. The uncertainties of the radar-derived thicknesses arise from uncertainties in the wave speed (±0.5%) and the selection of the migrated bed reflection (±15 m, Gades, 1998). The uncertainties in the ice thicknesses from Heinrichs et al. (1995) are larger (±10%), as the radar data was not migrated (Heinrichs et al., 1995, 1996). To account for the glacier thinning between the dates of the radar surveys and 2010 (date of the DEM), we subtracted the measured ice thicknesses from the ice surface elevations recorded during the surveys. This yielded bed elevations, which we then subtracted from the 2010 ice surface elevations to obtain adjusted ice thicknesses. Erosional or tectonic changes to bed elevation were neglected due to lack of data.

Comparison of the modeled and measured thicknesses indicated a small bias of 11.6 m (modeled ice too thick), but considerable scatter reflected by the mean absolute error (mae) of 99.7 m (Figure 4.2b). Investigating individual profiles indicated that ice depths at the profile center were typically underestimated (Figure 4.2b inset map) while the ice depths closer to the margins were overestimated by the model. In the lowest glacier reaches, the modeled glacier bed is systematically too shallow.

4.4.3 Debris cover and transient snow lines

We derived time series of debris cover and snowline elevations from medium-resolution Landsat spaceborne imagery (Thematic Mapper (TM), Enhanced Thematic Mapper (ETM+), Operational Land Imager (OLI)). While Landsat imagery has a limited spatial resolution of 30 (TM) and 15 m (pansharpened ETM+, OLI), one scene captures ~185 × 185 km in area, and thus Black Rapids

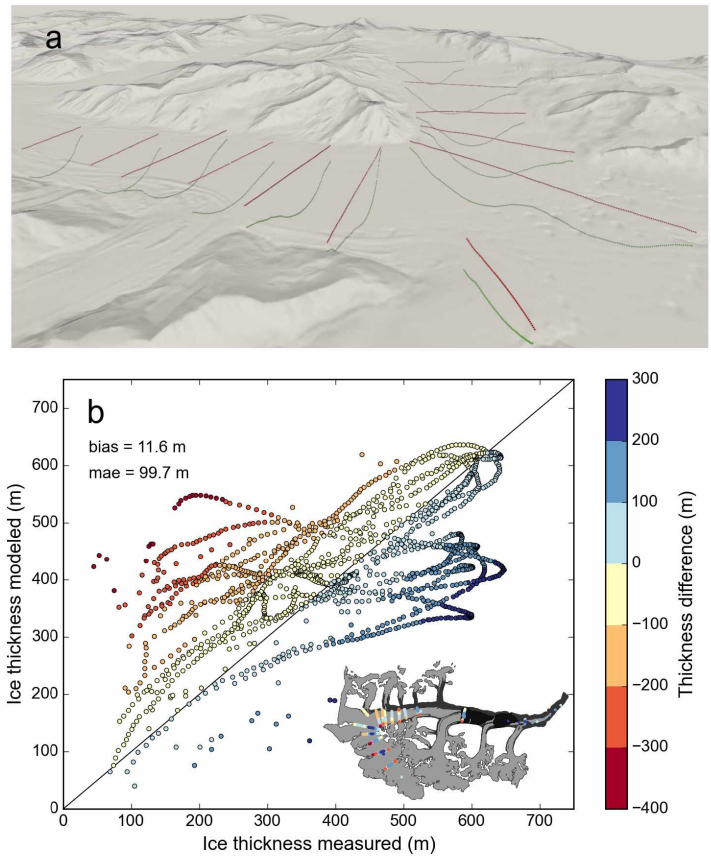

Figure 4.2: Surface (red) and bed elevations (green) surveyed in 1993 (Gades, 1998) superimposed on a shaded relief DEM from 2010. Viewing direction in the three-dimensional map is south towards the upper part of the main branch. (b) Measured vs. modeled ice thickness with colors showing the elevation difference. Blue colors indicate that the modeled bed is too shallow. The inset map shows the elevation differences at their actual locations. The measured thicknesses are adjusted for the 2010 surface.

Glacier in full (at the pass/row combinations 68/15, 68/16, and 67/16). The Landsat data was downloaded from the USGS EarthExplorer website (http://earthexplorer.usgs.gov).

4.4.3.1 Debris cover

Using 12 Landsat summer images and one aerial orthomosaic (Table 4.1), we obtained a series of debris layers in a semi-automated fashion. With the band ratio of red and shortwave infrared thresholded at 1.6, we derived an initial debris layer from a 1987 Landsat TM image. We then adapted this layer manually to arrive at the debris mask of the remaining scenes. This allowed us to classify the debris into rockslide debris and moraine debris, two categories with different

thicknesses on Black Rapids Glacier (Kienholz et al., 2016). The manual adaptation also allowed us to account for transient snowlines that fluctuated among images, sometimes obscuring debris portions at higher elevations. From 1980 to 2015, Black Rapids' debris cover increased by ~10 km^2 (from 35.4 to 45.4 km^2, Table 4.1), with a step change following the 2002 rockslides. The three 2002 rockslides buried ~11 km^2 of the glacier, of which ~5 km^2 were clean ice prior to the rockslides and ~6 km^2 covered by moraine debris.

For the mass balance model, we converted the 13 debris layers (spaced one to seven years apart, Table 4.1) into an annual debris time series. Linear interpolation, as implemented for glacier outlines and DEMs, proved impractical for debris. For each year without a derived debris layer, we thus adopted the debris layer closest in time.

Table 4.1: Remotely sensed imagery used to derive the debris time series. Debris cover is given in km^2 and percent of the total glacier area in 2010 (241.5 km^2).

Date	**Sensor**	**Path**	**Row**	**Debris cover**	**Debris cover**
				km^2	%
August 5, 1980	AHAP Wild RC10	–	–	35.4	14.7
August 23, 1987	Landsat TM	68	15	37.1	15.4
July 14, 1993	Landsat TM	68	15	36.6	15.2
September 14, 1995	Landsat TM	68	15	36.6	15.2
July 31, 1999	Landsat ETM+	68	15	37.3	15.4
August 1, 2002	Landsat ETM+	67	16	37.8	15.7
July 18, 2003	Landsat ETM+	68	15	43.2	17.9
August 8, 2005	Landsat TM	68	16	43.6	18.1
June 20, 2007	Landsat TM	67	16	43.7	18.1
August 3, 2009	Landsat TM	68	15	44.4	18.4
September 16, 2010	Landsat TM	67	16	44.5	18.4
July 13, 2013	Landsat OLI	68	15	45.3	18.8
August 4, 2015	Landsat OLI	68	15	45.4	18.8

4.4.3.2 Snow lines

Our transient snow line time series is based on 59 Landsat images taken between 1986 and 2015, but predominantly (50 scenes) after the year 2000. Tests indicated challenging conditions on Black Rapids Glacier for the automatic delineation of snow lines through band thresholding, for example, due to the steep, rough topography. To achieve the most accurate snow line elevations,

we thus opted for a workflow that automated all the processing steps except for the actual snow line delineation (Appendix 4.A). To estimate the accuracy of the derived snow lines, two operators derived two separate snow line datasets from the 59 Landsat scenes.

Rather than deriving one glacier wide snow line elevation per Landsat scene, we treated the nine largest glacier branches individually. This resulted in more than 300 snow line elevations for the main branch, Loket branch, and branches S1–S2 and N1–N5 (Figure 4.1). The branch-specific snow line elevations allowed us to validate the model output on smaller spatial scales, which is desirable given that Black Rapids Glacier covers branches with opposing aspects and potentially different microclimates. Treating the branches individually also allowed us to take advantage of partly cloudy satellite scenes.

4.4.4 Mass balance data

4.4.4.1 Geodetic mass balances

Kienholz et al. (2016) calculated geodetic mass balances including uncertainties for the periods 1980–2001 and 2001–2010 based on a range of elevation products. For the present study, we also used a third, laser altimetry-derived geodetic mass balance, covering the period 1995–2000 (Larsen et al., 2015).

4.4.4.2 In situ point mass balances

The mass balance monitoring program on Black Rapids Glacier focused on the main branch and the Loket tributary (Figure 4.1). The frequency of the visits, as well as number and location of the index sites, varied over the course of the program. From the mid 1970s to the mid 1980s, surface mass balances were measured at up to ten index sites covering most of Black Rapids' elevation range (Heinrichs et al., 1995, 1996). Up to eight index sites (all the sites in Figure 4.1, except for 11 and 29 km) were maintained along the centerline of the main glacier branch (between ~900 and 2200 m a.s.l.) and two along the centerline of the Loket tributary (at ~1500 and 1650 m a.s.l.). They were visited at least twice a year in spring and fall, allowing for the derivation of seasonal mass balances.

The mass balance program was downsized in the latter half of the 1980s. Maintenance of several work-intensive index sites located very high and very low on the glacier (2, 4, 26, 32, 38, L-19 km) was suspended and the number of visits restricted to one spring visit typically. During the mid-1990s, two new index sites (11 and 29 km) were established, however, site 29 km was buried by the 2002 rockslide deposits and not reestablished thereafter. Over the last decade, the mass balance program has consisted of two to four sites (8 km, 14 km, 20 km, L-22 km) visited once per

year in spring (Truffer et al., 2005). Two index sites, 8 and 14 km, have a nearly continuous record of annual mass balances over the length of the mass balance program (see Figure 11 in Kienholz et al. (2016)).

For each index site, we derived mass balances from measured stake heights and snow depths along with densities of the material (ice, snow, firn) gained or lost. For the early period with at least two visits per index site per year (spring and fall, with intermittent summer visits), we derived the seasonal balances in the floating time system (Cogley et al., 2011). Winter balances for the later period (one spring visit only) were obtained in the combined time system (i.e., the accumulation from the stratigraphic surface of the previous year to the surface at the time of the spring visit), while the corresponding annual balances refer to the stratigraphic time system.

Table 4.2: Independent error sources used to calculate uncertainties in the point mass balances (adapted from Heinrichs et al. (1995)).

Quantity	**Uncertainty**
Snow surface stake reading	± 0.02 m
Ice surface stake reading	± 0.10 m
Snow depth probing	± 0.03 m
Vertical stake movement in firn	± 0.15 m a^{-1}
Snow density estimate	± 40.0 kg m^{-3}
Firn density estimate	± 100.0 kg m^{-3}

To obtain error estimates for the point balances, we adopted procedures and error estimates outlined by Heinrichs et al. (1995). Starting with individual independent sources of uncertainties (Table 4.2), we applied standard error propagation to arrive at the combined uncertainties: uncertainties in sums were combined in quadrature, while for uncertainties in products, the fractional uncertainties were combined in quadrature. For example, to determine the winter balance errors (E_{bw}) in the combined time system, we applied the equation

$$E_{bw} = \sqrt{\left(\frac{e_s}{s}\right)^2 + \left(\frac{e_d}{d}\right)^2} \cdot s \cdot d, \tag{4.1}$$

where s and d denote measured snow depth and estimated snow density, while e_s and e_d stand for the corresponding snow depth and snow density errors from Table 4.2. The equations for the seasonal balances (floating time system) and annual balances (stratigraphic time system) are similar but also include probing and stake reading errors from two dates, as well as potential errors from firn compaction and stake slip, both processes which move the stakes relative to the

summer surface. As emphasized by Heinrichs et al. (1995), these error estimates do not address errors caused by blunders (e.g., snow depth probing to erroneous summer surface). In addition, they do not reflect uncertainties that arise from comparing the point observations to the values produced by the mass balance model, where one cell represents 10,000 m^2 in our case (100 m cell size). We transferred the final point balances, including error estimates, into a relational database from which they served the mass balance model and other applications.

4.4.5 Climate data

4.4.5.1 Reanalysis data

The atmospheric forcing for the ~37 year hindcasting period January 3, 1979 to October 29, 2015 was provided by Bieniek et al. (2016). They applied the Weather Research and Forecasting (WRF) Advanced Research core (Skamarock et al., 2008) to dynamically downscale the ERA-Interim reanalysis (Dee et al., 2011) from ~100 km to 20 km spatial resolution. To force our mass balance model, we used near-surface (2 m) temperature means and precipitation sums at daily time steps, which we derived from the hourly WRF output.

4.4.5.2 Future scenarios

For the ~85 year forecasting period October 30, 2015 to December 31, 2100, we worked with two forcing scenarios, a lower bound constant climate scenario and an upper bound RCP 8.5 scenario. The RCP 8.5 scenario projects a warming of ~6.5 °C between 2015 and 2100 and a corresponding precipitation increase of ~30% relative to the 2015 value. This scenario was provided by Lader et al. (in preparation), who downscaled both the historical run and the RCP 8.5 scenario from the Geophysical Fluid Dynamics Laboratory Climate Model version 3 (GFDL-CM3, Donner et al., 2011). Employing a quantile-mapping algorithm, they determined the temperature and precipitation differences between the future and historical GFDL runs, and used these differences to adjust the WRF-downscaled ERA-Interim reanalysis from Bieniek et al. (2016), which served as the observational dataset. Using 30 years of ERA-Interim data (1981–2010), they produced adjusted data for the time periods 2011–2040, 2041–2070 and 2071–2100. Rather than employing their full 2011–2100 time series, we used the reanalysis data from Bieniek et al. (2016) until the overlap of the two series ended on October 30, 2015. For the constant climate scenario, we repeated the same 30 year period (1981–2010) as Lader et al. (in preparation) without adjusting temperatures and precipitation. Figure 4.3 illustrates the three time series used for the atmospheric forcing.

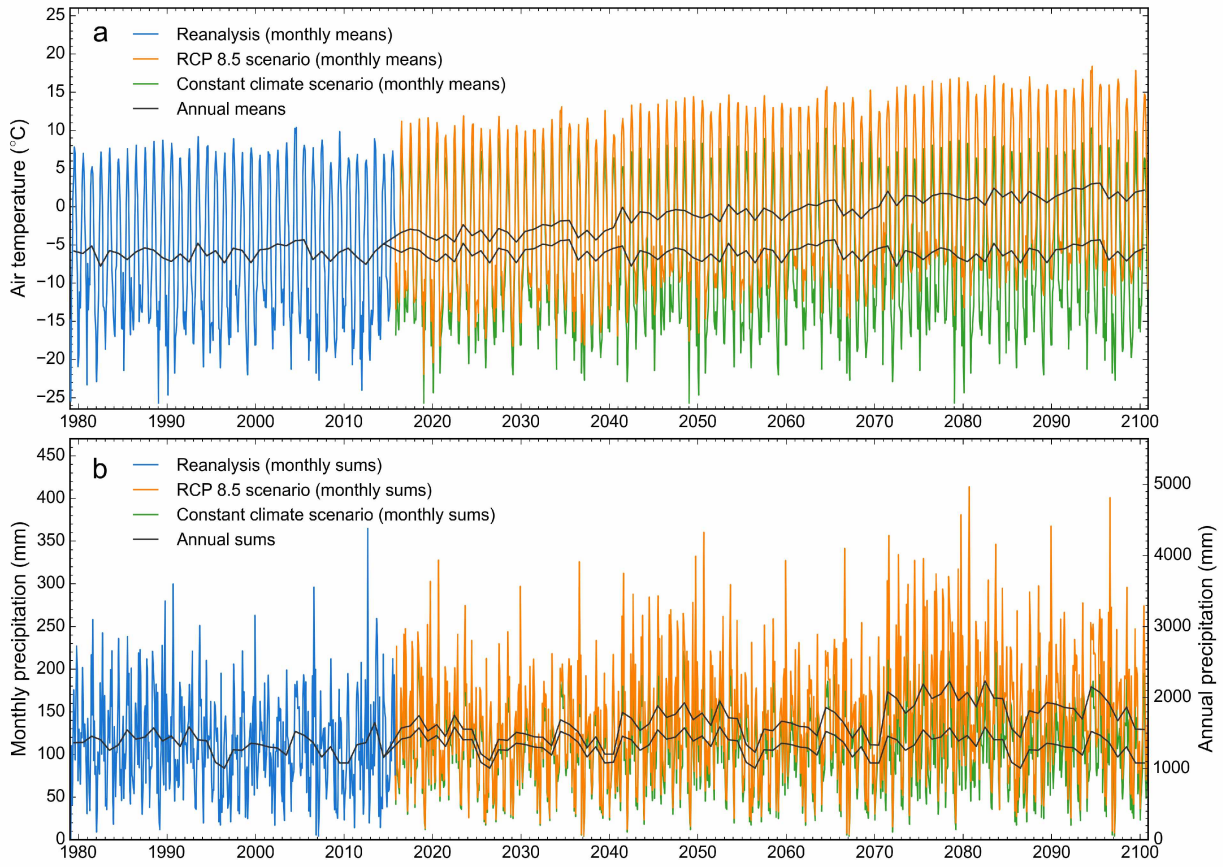

Figure 4.3: Near surface air temperature and precipitation time series taken from the WRF-downscaled ERA-Interim reanalysis (January 3, 1979 to October 29, 2015, used for hindcast) and the two forecast scenarios RCP 8.5 and constant climate (October 30, 2015 to December 31, 2100). The figures show monthly and annual means for (a) temperature and the corresponding sums for (b) precipitation. The data are taken from the WRF gridpoint with center at 63.42°N and 146.18°W and an elevation of 1525 m a.s.l.

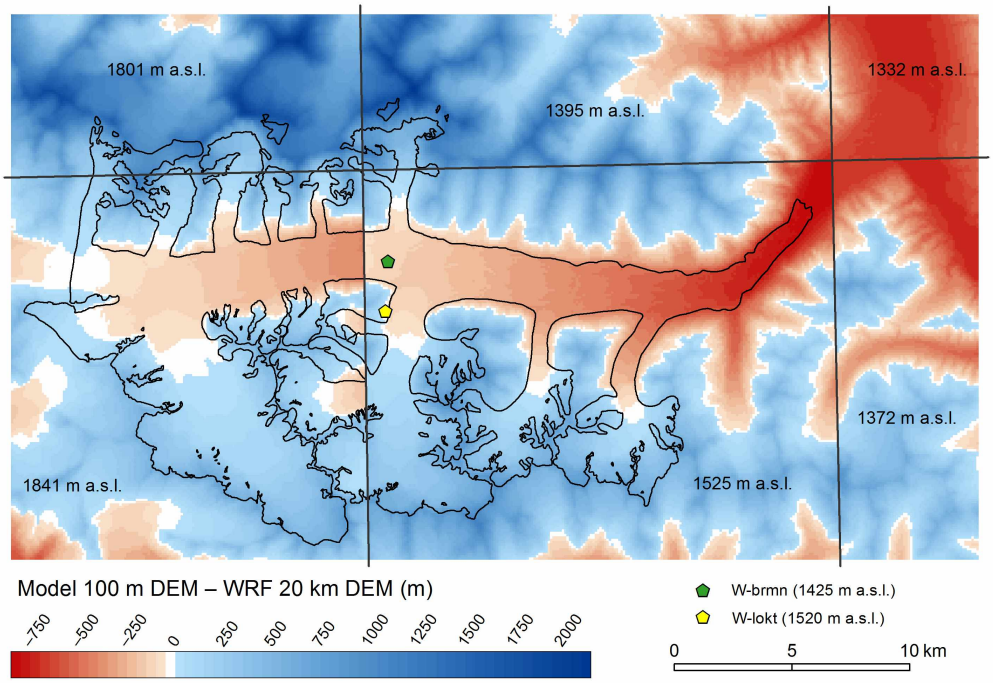

Figure 4.4: Elevation difference between the 100 m DEM used for the glacier modeling (year 2010) and the 20 km DEM used to dynamically downscale the ERA-Interim data. Elevation differences exceed 1000 m in the highest and –800 m in the lowest glacier reaches. The edges of the 20 km DEM cells are indicated with black lines and the cell elevations are annotated. Prior to the differencing, the 20 km DEM was resampled to 100 m. W-brmn and W-lokt mark the locations of the two weather stations.

4.4.5.3 Downscaling

The WRF-downscaled climate products (both reanalysis data and future scenarios) come with a spatial resolution of 20 km, considerably coarser than the 100 m resolution of our glacier model. The elevation differences between the 20 km DEM of the WRF-model and the DEM of our glacier model reach several 100 m (Figure 4.4), demanding additional downscaling steps. We took a simple approach similar to that of previous workers (e.g., Machguth et al., 2009; Schaefer et al., 2013). Assuming that the WRF-modeled temperature and precipitation reflect the center of each 20 km cell, we interpolated among cells, accounting for the topography using temperature lapse rates and precipitation gradients. In practice, we applied a three step procedure. For the temperatures, we brought the 20 km values (T^{20km}) to sea level (T^{20km}_{0m}), applying the lapse rate l to the WRF topography (z^{20km}):

$$T^{20km}_{0m} = T^{20km} - z^{20km}/l \tag{4.2}$$

We then bilinearly interpolated T_{0m}^{20km} to the 100 m grid (T_{0m}^{100m}) and computed temperatures for each grid cell of the 100 m DEM (z^{100m}) by applying the same lapse rate in reverse:

$$T^{100m} = T_{0m}^{100m} + z^{100m}/l \tag{4.3}$$

The processing for precipitation was similar. We first brought the 20 km precipitation (P^{20km}) to a reference elevation of 1500 m a.s.l. (P_{1500m}^{20km}) using the precipitation gradient s:

$$P_{1500m}^{20km} = P^{20km}/(1 + (z^{20km} - 1500) \cdot s) \tag{4.4}$$

We then bilinearly interpolated the precipitation to a 100 m grid (P_{1500m}^{100m}) and reintroduced topographic effects by applying s to z^{100m}:

$$P^{100m} = P_{1500m}^{100m} \cdot (1 + (z^{100m} - 1500) \cdot s) \tag{4.5}$$

Precipitation gradients are tied to a reference elevation, which defines the reference (100%) precipitation. With multiple distributed precipitation values at different elevations (defined by the WRF topography), we specified one reference elevation to ensure the same gradient was employed across the modeling domain. While this elevation can be chosen randomly (here, we chose 1500 m a.s.l.), the optimized gradient in the mass balance model will vary as a function of the reference elevation chosen.

While the precipitation gradient s is a calibration parameter of the mass balance model (Section 4.5.1), we derived the temperature lapse rates from the WRF near-surface temperatures directly. Over weekly periods, we combined the temperature-elevation pairs of the 12 WRF cells in the Black Rapids domain, and then estimated the lapse rates using linear regression. As expected, the lapse rates are lowest in winter and highest in spring. Throughout the melt season, they vary between 6.0 and 7.2 °C km^{-1}.

During the calibration of the mass balance model (Section 4.5.4), we used our DEM time series (Section 4.4.1) to annually update the 100 m topography z^{100m} employed during the downscaling. During the free hindcast and projection runs (Sections 4.6.1, 4.6.2), we used the updated DEMs produced by our model instead.

4.4.5.4 Bias check

We used in situ air temperature observations taken during the summers of 2012–2014 to evaluate potential biases in the WRF near-surface temperatures. Air temperatures were measured both off-ice and on-ice at the locations W-lokt and W-brmn, at 1520 and ~1425 m a.s.l., respectively (Figure 4.1). The deployed Vaisala temperature sensors recorded near-surface temperatures (~2 m above

ground) at sub-hourly time steps (varying between 10 and 15 minutes over the three seasons), which we averaged to match the daily resolution of the WRF data.

Overall, the in situ temperatures agree very well with the WRF temperatures. The off-ice comparison suggested very small warm biases (< 0.5 °C) in the WRF temperatures throughout the three seasons (Figure 4.5a–c), which we considered too small to justify a correction of the WRF input across the glacier domain. The temperatures at the on-ice station were several degrees colder than the WRF output during the melt season, while they matched well during times without melt (Figure 4.5d). During the melt season, the near-surface air cools by transferring heat to the ice (which cannot exceed 0 °C), a process not reproduced in the WRF model due to its coarse resolution (glacier ice is not represented in the WRF surface grid). Temperature index models have been shown to perform better when forced by off-ice temperatures (Lang, 1968), hence we refrained from correcting this seasonal difference in the WRF data prior to the calibration. It is indirectly accounted for during the calibration with the choice of appropriate melt and radiation factors.

4.5 Glacier model

The glacier model is based on code developed by Anderson et al. (2006, 2008) originally. For this project, we added the Enhanced Temperature Index Model by Hock (1999) to complement the melt models previously available (classic degree day, energy balance). We implemented calibration code that can leverage all types of calibration data including geodetic balances, snow line elevations, and point mass balances, with the latter in all possible time systems. Advancing the calibration included establishing communication with a relational database hosting calibration data and other model input. To account for the ice dynamics and the corresponding debris evolution, we implemented the retreat parametrization by Huss et al. (2010) and a simple debris evolution model.

4.5.1 Surface mass balance

The Enhanced Temperature Index Model runs in a distributed fashion, in our case, on a 100 m grid. Melt, M (mm d^{-1}), is derived from daily average air temperature, T (°C), by

$$M = \begin{cases} (f_m + r_{snow/ice} \cdot I) \cdot T & : \; T > 0 \\ 0 & : \; T < 0 \end{cases}, \tag{4.6}$$

where f_m is the melt factor (mm d^{-1} °C^{-1}), $r_{snow/ice}$ are the radiation factor of snow and ice (mm m^2 W^{-1} °C^{-1} d^{-1}), and I is the potential clear-sky direct solar radiation (W m^{-2}). When

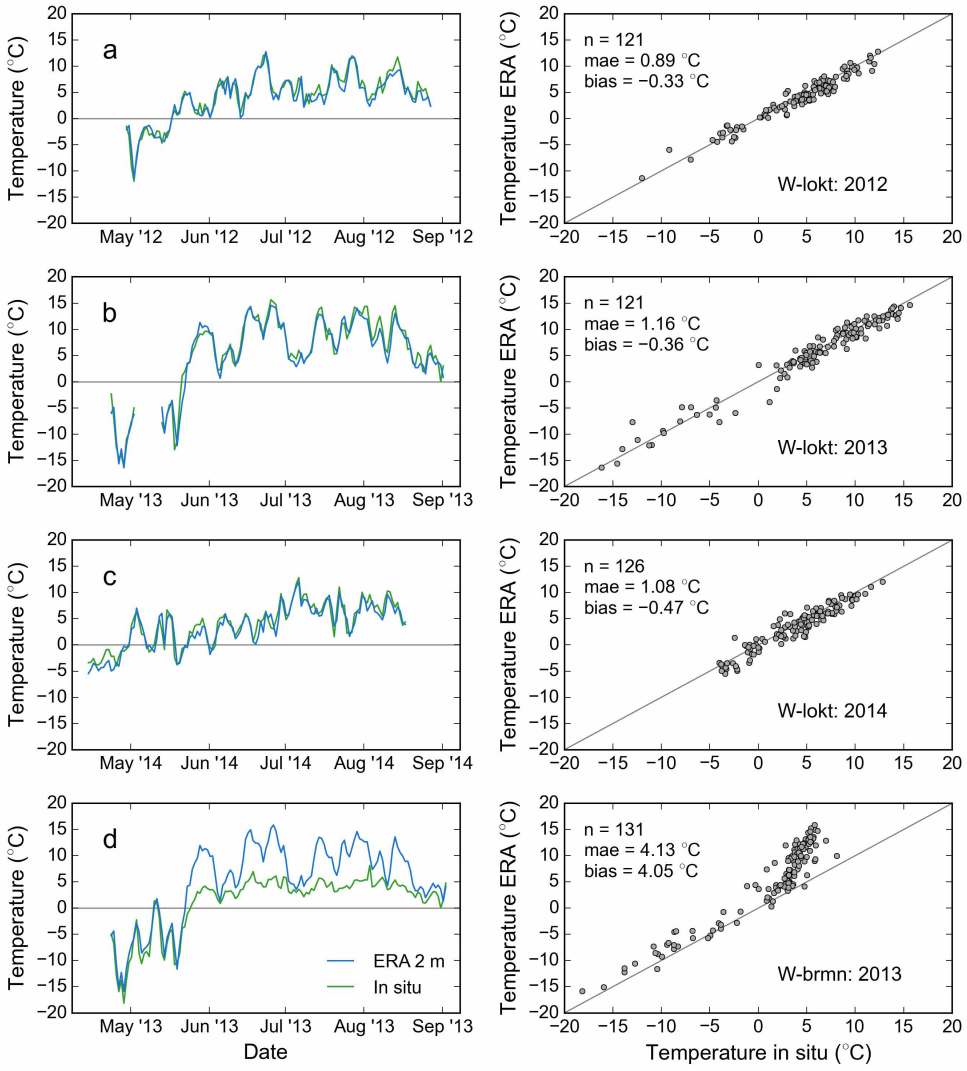

Figure 4.5: Daily average in situ air temperatures vs. downscaled ERA-Interim near-surface (2 m) temperatures for (a–c) the off-ice station W-lokt during the three summer seasons 2012–2014 and (d) the on-ice station W-brmn during summer 2013. W-lokt had a measurement gap in May 2013. Upon melt onset, the ERA near-surface temperatures become significantly warm biased when compared to the temperatures measured at the on-ice station. See Figure 4.4 for the locations of the stations.

firn is exposed at the glacier surface, the radiation factors of snow, r_{snow}, applies. While m and $r_{snow/ice}$ are calibration parameters, I is calculated from the DEM using standard algorithms. T is the near-surface air temperature as downscaled from the WRF data (Section 4.4.5.3). Upon complete debris exposure, M is multiplied with a melt reduction factor that varies as a function of the debris class. While the reduction factor for moraine debris (d_m) is a calibration parameter, the

reduction factor for the several meter thick rockslide debris d_s is kept constant at 0.05 (95% melt reduction compared to debris-free conditions). The latter value agrees with field measurements that show minimal ice melt below the rockslide debris (D. Shugar, personal communication, 2016). Before the debris surface is exposed completely (snow cover 0.1 m w.e. and less), both d_m and d_s are treated as melt enhancement factors. Between 0.1 w.e. snow cover and snow-free conditions, their values increase linearly from 1 to 5 to account for the accelerated snow melt above the debris surface.

To model snow accumulation, the solid part of the precipitation is retained, while the liquid part is assumed to run off without refreezing. A smooth transition between solid and liquid precipitation is obtained by applying a linear function between 0.5 and 2.0 °C. Beyond these thresholds, the retained solid precipitation is 100 and 0%, respectively. The accumulation model has two calibration parameters, the precipitation gradient s (used during the precipitation downscaling, Section 4.4.5.3) and a precipitation factor p, which acts as a glacier wide multiplier for the downscaled precipitation field.

At the end of each calendar year, the winter and summer surfaces of that year are determined by analyzing the cumulative mass balance grids. Detecting the seasonal surfaces allows for modeling mass balances in the stratigraphic and combined time systems, which is required to take full advantage of our calibration data. To be able to track the transient snow lines in the model, we distinguish snow from firn. Every year, snow older than the previous summer surface is added to the firn, which is treated crudely in our model: firn is retained for seven years or until the firn layer exceeds 10 m w.e. in thickness. To obtain realistic snow and firn thicknesses at the beginning of the modeling period, the mass balance model is run seven times for the first year before the actual run is launched.

4.5.2 Ice dynamics

The mass conserving Δh-parametrization by Huss et al. (2010) prescribes the relationship between ice thickness change and elevation, based on observations rather than application of an actual ice flow model. Compared to a flow model, the Δh-parametrization has low computational costs and requires no calibration in the typical sense (prescription of the glacier-specific Δh-curve is sufficient). We derived the Black Rapids' Δh-curve from centerline elevation changes measured between 1995 laser altimetry profiles and the 2010 InSAR DEM (Kienholz et al., 2016).

The Δh-parametrization is coupled to the surface mass balance model and run on annual time steps, yielding updated surface elevations and glacier extents each year. Following Huss et al. (2010), surface lowering is restricted not to deceed that year's most negative surface mass balance in ice equivalent; moreover, the Δh-parametrization is not applied in areas where ice thickness is

less than 10 m. The Δh-parametrization is well suited for glaciers with negative mass balances (and thus retreat), which applies to Black Rapids Glacier over the period of interest. For the few years with positive glacier wide mass balances, the excess mass is distributed evenly across the glacier, not allowing for glacier advance. This is considered appropriate given the small magnitude and frequency of the positive mass balances.

4.5.3 Debris

While the debris cover remained prescribed during the hindcasting period, we implemented a simple debris model to capture potential debris evolution during the forecasting period. This model, which runs on annual time steps, treats rockslide debris and moraine debris separately. While it adapts the extent of the debris layers, it does not capture thickness changes and neglects mass conservation in general.

Rockslide debris is translated downglacier based on an idealized ice flow velocity field. Without an ice flow model and complete velocity fields from satellite data, we derived the ice flow directions from the low-pass filtered 2010 InSAR DEM by determining the steepest downhill directions among each glacier cell and its neighbors. Annual speeds were assumed proportional to the cell's distance to the closest glacier margin, multiplied by a tuning factor to match sparse velocity observations derived from 2013 TanDEM-X satellite data.

The evolution of the moraine debris relies on a prescribed relationship between normalized elevation range and moraine debris cover fraction. Each year, considering the topography changes from the Δh-parametrization, the moraine debris layer is adapted to meet the prescribed debris fraction for each elevation bin. To achieve lateral debris growth, ice cells are converted to moraine debris cells along the boundaries of the existing moraine debris layer. Which of the bordering ice cells are converted to moraine debris is determined in a random fashion for each elevation bin. Removal of moraine debris is not allowed, which is considered appropriate given the predominant glacier retreat. We derived the Black Rapids-specific relationship between elevation range and moraine debris fraction from the debris layer for the year 2015 (Section 4.4.3.1) using 100 m elevation bins. To avoid a distorted relationship, we replaced the rockslide debris portion with the moraine debris underneath the rockslide debris (based on geomorphologic evidence in the 2015 Landsat image and satellite imagery taken before the 2002 rockslide event).

4.5.4 Model calibration and validation

We calibrated six parameters for the surface mass balance model: two for the accumulation model (s, p) and four for the melt model (f_m, r_{snow}, r_{ice}, d_m). The goal of the calibration was to maximize the

agreement between modeled and observed point mass balances as well as modeled and observed glacier wide (geodetic) mass balances. The calibration period comprised the hydrological years 1980–2013. Validation of the surface mass balance model was based on Landsat-derived snowline elevations.

Throughout the calibration, glacier extent, surface elevation and debris cover were prescribed from observations, in order to capture three important feedback mechanisms: 1) the positive climate-elevation feedback, 2) the negative feedback due to glacier retreat and 3) the negative feedback due to increasing debris cover. The positive climate-elevation feedback is caused by glacier thinning, which exposes the glacier surface to higher temperatures (and lower precipitation), which in turn increases the thinning further. In contrast, glacier retreat exerts a negative feedback on glacier mass balance, as the deglacierized areas are lowest in elevation and thus characterized by mass balances below the glacier wide average (due to debris cover, the mass balances of the deglacierized areas are not necessarily most negative). With the glacier wide mass balance more positive after the retreat, future retreat is suppressed, exerting a negative feedback. Finally, glacier thinning enables fast debris accumulation on the glacier surface, due to more intense gravitational processes (which add more debris to the glacier) and decreasing ice flow (which slows down debris evacuation). Growing debris layers (thick in the case of Black Rapids Glacier) in turn will moderate melt and thus thinning, decelerating further debris accumulation and thus exerting a negative feedback. The three feedbacks affect the geodetic balances, and in the case of the climate-elevation feedback also the in situ mass balance measurements (due to the elevation lowering of the index sites). To facilitate a meaningful calibration, the feedbacks were included in the model through our time series of glacier extent, surface elevation and debris cover. Upon completion of the surface mass balance model calibration, we ran the glacier model without prescribing the glacier evolution (extent, surface elevation) from observations.

4.5.4.1 Calibration

Following Trüssel et al. (2015), we searched the parameter space systematically within prescribed ranges, which is a simple, yet computationally intense process. To reduce the computational costs, we split the calibration into two steps. In the first step, we constrained a plausible range of precipitation factors and gradients based on our set of observed winter point mass balances. In the second step, we used both seasonal and annual point mass balances, as well as geodetic balances, to fine-tune the precipitation factors/gradients and to calibrate the four parameters of the melt model. To ensure independence of the seasonal and annual mass balances in the second step of the calibration, we relied on seasonal balances before 1989 and annual balances thereafter (Figure 4.6). Our grid search across the parameter space resulted in >150,000 model runs.

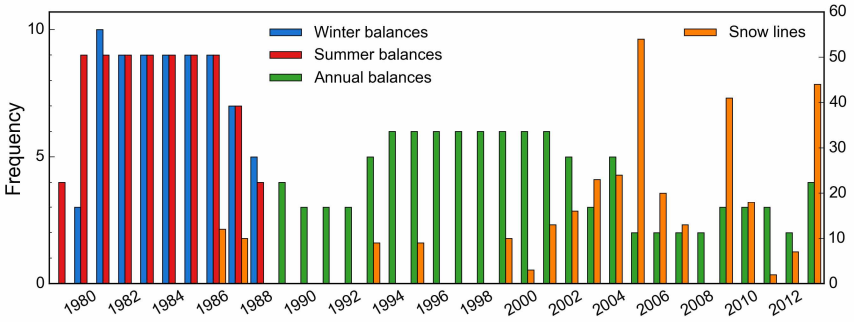

Figure 4.6: Mass balance and snow line data used for model calibration and validation. The numbers of point mass balances (used for calibration) and branch-specific snow line elevations (used for validation) are given on the left and right axes, respectively. Overall, we used 250 independent point mass balances and 328 branch-specific snow line elevations.

Rather than deriving one single best parameter combination for further analysis, as often done in previous studies, we determined a range of best parameter combinations which we all considered equally valid. We chose them as follows. First, we compared the modeled glacier wide mass changes to the three geodetic mass balances (available for the periods 1980–2001, 2001–2010 and 1995–2000, Section 4.4.4.1), and extracted all parameter combinations that yielded balances within the uncertainties of the observations for all three periods. This resulted in 4576 combinations, which we further reduced by considering the agreement between modeled and observed seasonal and annual point mass balances (workflow in Figure 4.7). To account for the uncertainties in the point balances (Section 4.4.4.2) we randomly varied the measured point balances within their errors 10,000 times in a Monte Carlo fashion. After each Monte Carlo run, we recalculated the mean absolute error (mae) of the modeled balances for each parameter combination and gave the solution with the lowest mae the first rank. Solutions that achieved the first rank at least once (40 solutions) were then kept as the best solutions (Figure 4.8). Figure 4.9 illustrates the parameter values of those best solutions.

All our selected parameter combinations have precipitation factors above one, suggesting the WRF-downscaled ERA-Interim precipitation has a dry bias across our study area. This differs from the findings of Bieniek et al. (2016), according to which the WRF-downscaled ERA-Interim precipitation is wetter than observations over most of mainland Alaska. While our results are based on winter balances measured at stakes, Bieniek et al. (2016) rely on weather station data and gridded observations for their comparison. Weather station data are available only at low elevations and thus not ideal for detecting biases at higher elevations such as the Black Rapids Glacier domain. Gridded observations come with considerable uncertainties themselves, leaving

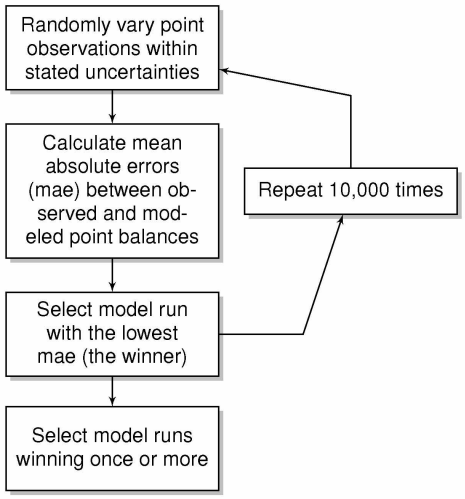

Figure 4.7: Flow chart illustrating derivation of the final parameter combinations.

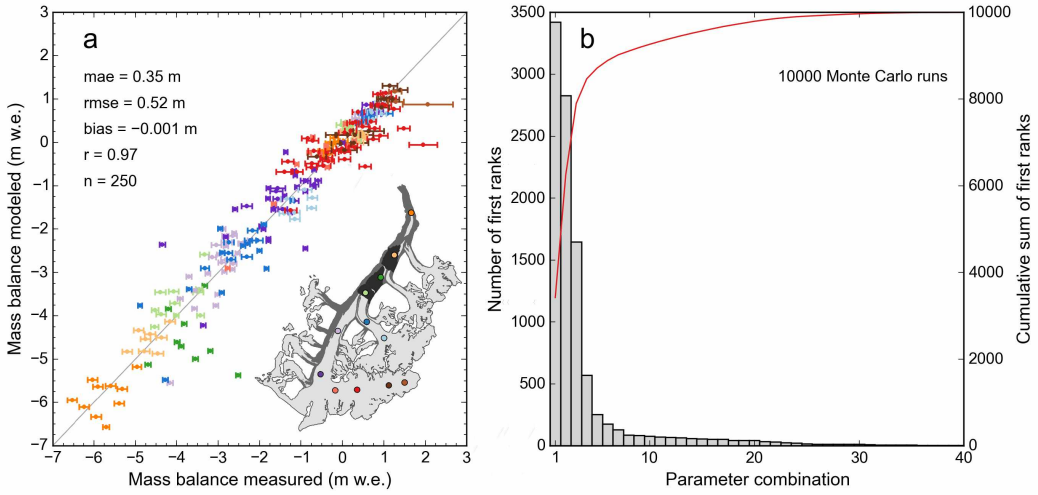

Figure 4.8: (a) Measured vs. modeled point mass balances for the best parameter combination modeled (f_m = 0.9, r_{snow} = 0.017, r_{ice} = 0.035, s = 12.4, p = 1.12, d_m = 0.45). Error bars indicate the uncertainties in the measured mass balances. Colors distinguish index sites with locations shown on inset map. (b) Histogram indicating the number of first ranks accumulated during 10,000 Monte Carlo runs. The parameter combinations are ordered by the number of first ranks.

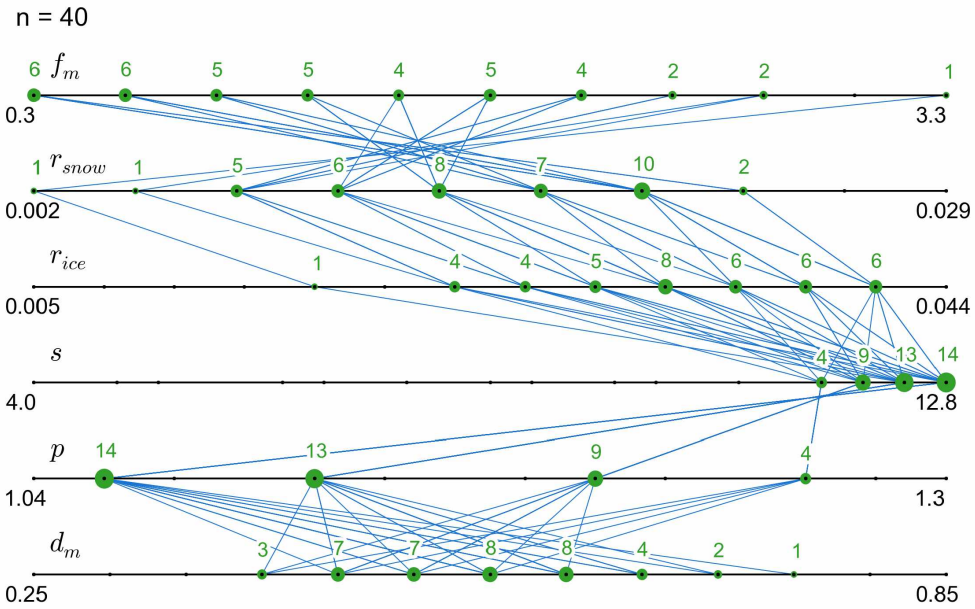

Figure 4.9: Parameter combinations of the 40 best calibration runs superimposed on the searched parameter space. f_m is the melt factor (mm d^{-1} $^{\circ}C^{-1}$); $r_{snow/ice}$ are the radiation factors of snow and ice (mm m^2 W^{-1} $^{\circ}C^{-1}$ d^{-1}); s is the precipitation gradient (% 100 m^{-1}); and p and d_m are the unitless precipitation and melt reduction factors. Numbers on the left and right sides are the end members of the parameter space. Small black dots on the lines show the parameter values tested. Blue lines connect the successful parameter combinations. The green points and their annotations indicate the number of successful combinations crossing through a particular parameter value. Precipitation gradients >12.8% 100 m^{-1} caused implausibly low precipitation at the glacier terminus and thus were not accepted.

it open whether the differences arise in the WRF-downscaled precipitation or the corresponding gridded observations.

4.5.4.2 Validation

Given the simplicity of the model applied, observed and modeled snow lines matched relatively well. Glacier wide, we found positive biases of 30–60 m when comparing the modeled snow line elevations from the best 40 parameter combinations to the Landsat-derived snow line elevations. The mean absolute error across all branches was typically ~100 m. Investigation of individual branches showed that the modeled snow lines of the north- and south-facing branches had opposite biases: in the south-facing branches, they were too low, while in the north-facing branches, they were too high (Figure 4.10a,b). Along the main branch, modeled and observed snow lines matched relatively well. Figure 4.10c illustrates the spatially varying mismatch using an example from August 2005. The biases found can not be attributed to errors in the Landsat-derived snow lines, although the derivation of snow lines from satellite imagery can be ambiguous. While the comparison of the two independently derived snow line datasets indicated considerable scatter (37 m mae) and a systematic difference (30 m bias), the biases among the branches did not match the pattern emerging in the model-observation comparison.

None of the radiation/melt factor combinations of the 4576 parameter combinations matching the geodetic balances eliminated the difference between north- and south-facing branches (Figure 4.10b). This indicates the biases are related to the modeled snow accumulation, which likely suffers from the use of spatially coarse precipitation input and our first-order downscaling approach. Our downscaling crudely represents orographic precipitation and neglects snow redistribution by avalanches and wind, the latter of which is important on Black Rapids Glacier. Snow redistribution by wind is challenging to model at present and often, redistribution grids based on observations are employed instead (e.g., Sold et al., 2013). However, our current observations at the index sites are too sparse to derive a glacier-wide snow redistribution grid, obliging us to accept the bias as-is for the present study. Future work may apply backward modeling of melt (e.g., Hulth et al., 2013) along the Landsat-derived snow lines to derive more spatially distributed end-of-winter accumulation information. Ideally, such modeling efforts will be complemented with in situ accumulation measurements by radar (Gusmeroli et al., 2014; McGrath et al., 2015).

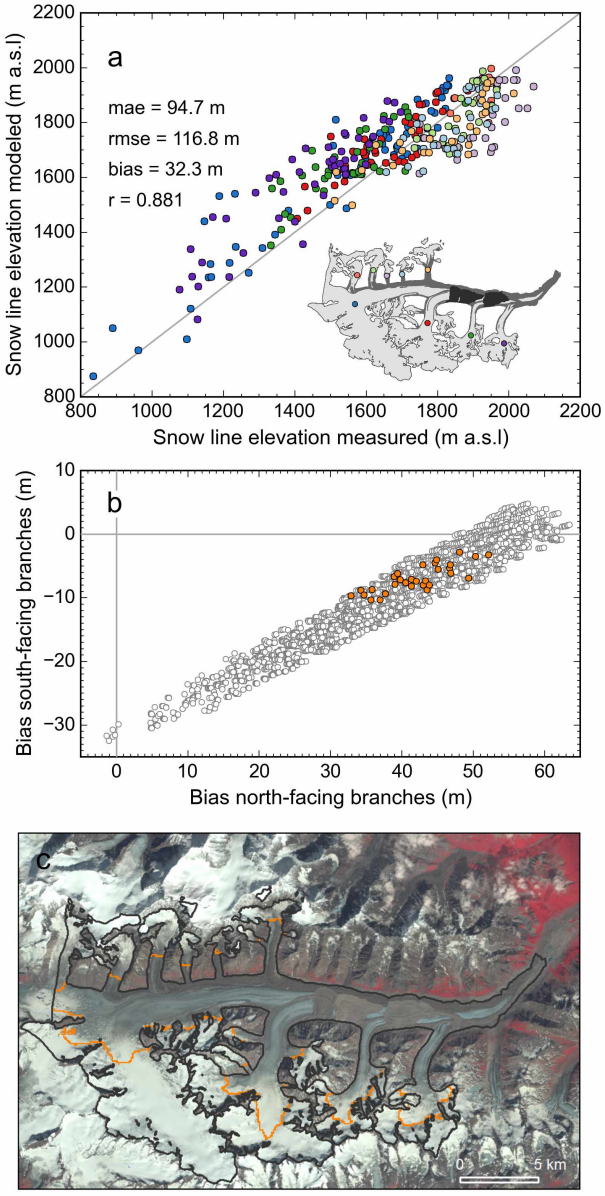

Figure 4.10: (a) Measured vs. modeled snow line elevations for one of the 40 best parameter combination. The color code in the inset map distinguishes individual branches. (b) Biases across the north-facing branches vs. biases across the south-facing branches for the 4576 parameter combinations matching the three geodetic mass balances (white points) and the 40 final parameter combinations (orange points). Ten final parameter combinations have biases identical to another final parameter combination, as the combinations differ only in the melt reduction factor under debris (d_m), which does not affect the snowline elevation. (c) Modeled snow lines (orange lines) vs. observation (Landsat Thematic Mapper (TM) composite) for August 8, 2005. This example shows the spatially varying mismatch between modeled and observed snow lines. While the modeled snow lines are too high in the north facing slopes, they are too low in the south facing slopes. Along the main branch, the match is relatively good.

4.6 Results and discussion

4.6.1 Hindcasting (1980–2015)

The hindcasting results are based on the free running model and the 40 most successful parameter combinations. Over the entire hindcasting period, Black Rapids Glacier lost $4.3^{+0.2}_{-0.2}$ Gt of ice (Figure 4.11), which is ~9.5% of its total mass estimated for the year 2010. The 4.3 Gt reflect the mean mass loss across the 40 parameter combinations, while sub-/superscripts delimit the full range of results. For the early hindcasting period (~1980–1988), the model indicates glacier wide mass balances close to zero and negligible area changes, with accumulation area ratios (AARs) and Equilibrium Line Altitudes (ELAs) clustering around 0.6 and 1700 m a.s.l., respectively (Figure 4.12a–c). After 1988, a negative mass balance trend sets in, causing lower AARs and considerable glacier retreat. Only two years (2000 and 2008) have positive annual mass balances after 1988, while seven years have balances deceeding –1 m w.e.. The year 2004 is a negative outlier with an annual specific mass balance deceeding –2 m w.e., resulting in an AAR close to 0.1 and an ELA at ~2150 m a.s.l. (Figure 4.12b,c). This extreme result is in line with field observations: Truffer et al. (2005) attributed 2004's record negative mass balances to the heat wave occurring that summer, which is reflected in our very negative summer balance of that year (–3 m w.e., Figure 4.12c).

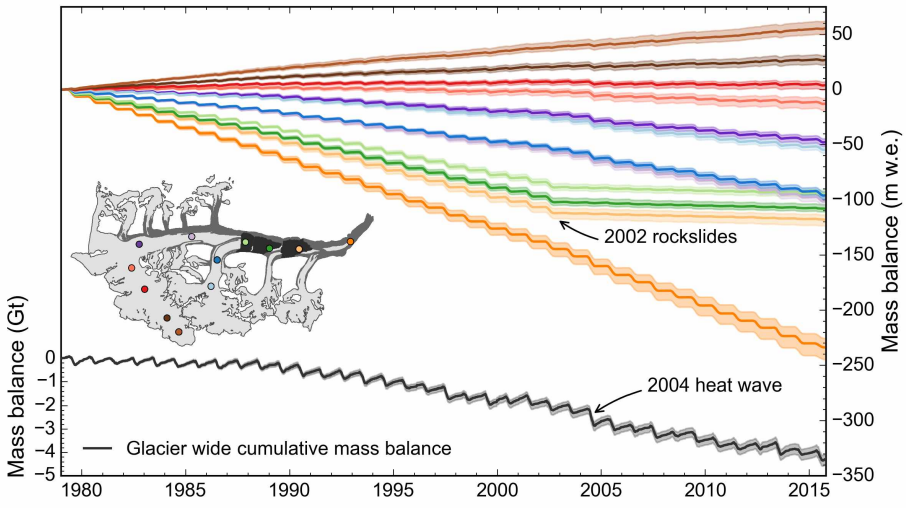

Figure 4.11: Evolution of the glacier wide cumulative mass balance (left axis) and the cumulative mass balances at the index sites (right axis) over the course of the hindcasting period. The color code for the index sites is given on the inset map. Bold lines indicate the mean of the results of the 40 parameter combinations while the semi-transparent areas delimit the full range of the results.

Of the 12 index site locations, only two (2 and 4 km) are located in the accumulation zone over the entire hindcasting period (Figure 4.11). The cumulative mass balance at index site 8 km is

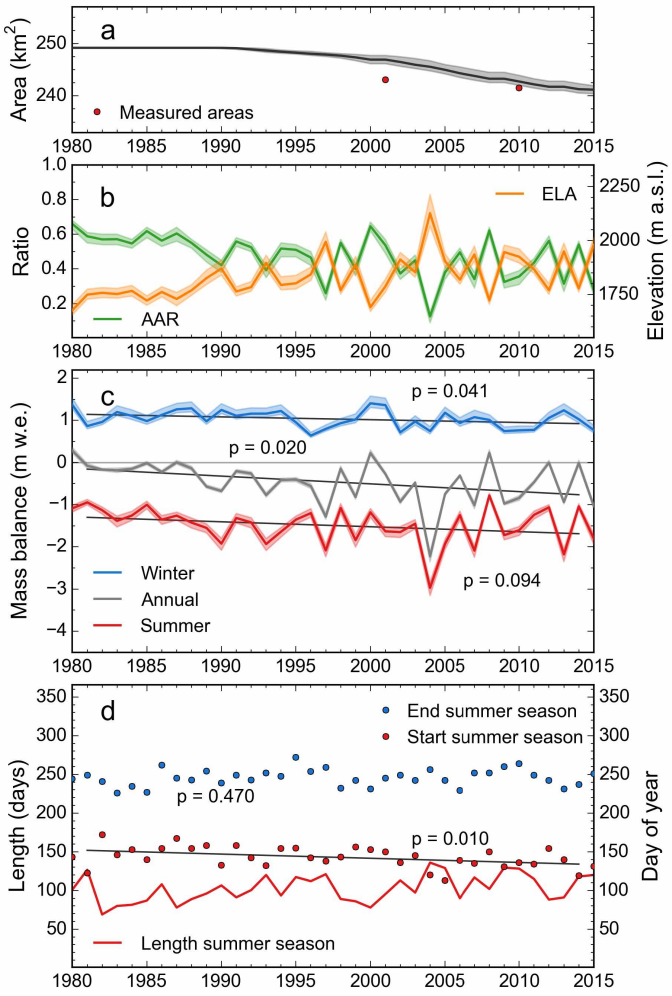

Figure 4.12: Evolution of (a) glacier area, (b) AAR and ELA, and (c) annual and seasonal glacier wide (specific) mass balances during the hindcasting period 1980–2015. (d) Evolution of the summer season length (left axis) and start/end dates of the summer seasons (right axis). Transition between winter and summer season occurs when reaching that years' maximum (winter-summer) and minimum (summer-winter) glacier mass. In (a)–(c), bold colored lines indicate the mean of the results of all parameter combinations while the semi-transparent areas (if available) delimit the full range of the results. The bold black lines show the trend lines with p values indicating the degree of statistical significance.

slightly positive over the hindcasting period, though only due to the residual mass accumulated in the early hindcasting period (Figure 4.11). Over the latter part of the hindcasting period the 8 km index site is close to the glacier's equilibrium line, with both positive and negative mass balance years occurring. Index site 11 km shows a similar pattern: while just at the equilibrium line in the early hindcasting period, it is located in the ablation zone in most of the recent years.

The index sites 26–32 km are affected by the 2002 rockslide deposits, which cause subdued annual mass balance cycles after 2002. Towards the end of the hindcasting period, the cumulative mass balances of the index sites 26–32 km approach those of the index sites L-22 km and 20 km, which are located ~200–400 m higher on the glacier. Index site 38 km close to the present terminus has the most negative surface mass balance, accumulating to –230 m w.e. over the 35 year hindcasting period.

Both the winter and summer balances, and thus the annual balances, show negative trends, implying decreasing mass accumulation in the winter season and increasing mass loss in the summer season (Figure 4.12c). The trends, fitted by linear regression, are significant at the 0.05 and 0.1 levels, with the summer trend nearly twice as negative as the winter trend. The negative trends coincide with summer seasons becoming longer and winter seasons becoming shorter (Figure 4.12d). The extension of the summer season occurs in spring only: while the summer season sets in earlier over time (significant at the 0.01 level), no significant trend is observed with regard to its end date ($p = 0.47$).

The hindcasting period is characterized by increasing debris cover and glacier retreat, both of which exert negative feedbacks on the glacier wide specific mass balances. Yet the model indicates increasingly negative mass balances, so that the atmospheric warming and the positive climate-elevation feedback must exceed the combined effects of the negative feedbacks. To evaluate the relative strengths of the climate-elevation feedback and the feedback due to glacier retreat, we ran the mass balance model without adapting the glacier's geometry (i.e., on the 1980 reference-surface, Elsberg et al., 2001) and compared the resulting specific mass balances to our conventional hindcasting runs. While the cumulative balances from the two experiments are nearly identical overall, the conventional balance becomes slightly more negative towards the end of the hindcasting period, indicating that the positive climate-elevation feedback is slightly stronger than the negative feedback due to glacier retreat. This suggests the glacier's adaptation leads to a geometry more susceptible to warming than without adaptation, setting the stage for unstable thinning similar to other glaciers in Alaska (e.g., Trüssel et al., 2015).

Observations indicate that the negative mass balance trend would be amplified without deposition of the 2002 rockslide debris. While the rockslide deposits are ~4.5 m thick on average (Kienholz et al., 2016), the deposits' surfaces were located ~15 m above the surrounding ice surface in 2007, only five years after the rockslides (Shugar and Clague, 2011). To evaluate the rockslides' effect on the glacier wide mass balance quantitatively, we compared the conventional hindcasting runs to runs without debris layer update after 2002. Between the 2003 and the 2015 hydrological years, the glacier wide cumulative mass balances differ by ~20% (Figure 4.13) although the rockslide deposits make up only ~4.5% of the total glacier area. The deposits' strong impact is

due to their location in the lower ablation zone (between ~1000 and 1400 m a.s.l., Figure 4.1), where the melt suppression is very effective by applying over a longer period than at higher, colder elevations.

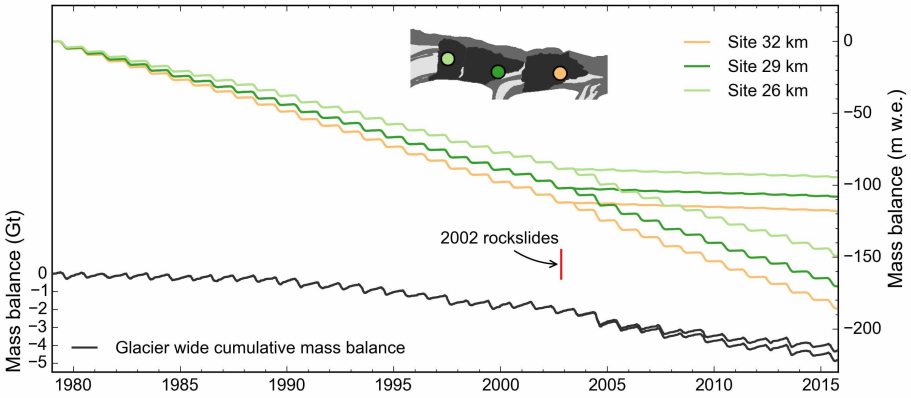

Figure 4.13: Cumulative mass balances modeled with and without considering the 2002 rockslide deposits. The glacier wide cumulative mass balances are shown on the left axis. The cumulative mass balances at the three index sites affected by the rockslide deposits are shown on the right axis. The inset map shows the index site locations. The lines reflect the mean of the results of all 40 parameter combinations.

The range in the results modeled, arising from the use of the 40 parameter combinations, is relatively small. At the end of the 35 year hindcasting period, the glacier wide cumulative mass balances of the most positive and most negative parameter combinations differ by only 0.2 Gt from the mean, which corresponds to ~5% of the total change modeled (Figure 4.11). The ranges in the modeled summer and winter balances have similar magnitudes which even out when combining the seasonal balances to annual balances (reflected by the annual balances' smaller uncertainty range, Figure 4.12c).

4.6.2 Projections (2015–2100)

4.6.2.1 GFDL-CM3 RCP 8.5 scenario

Our projections for the RCP 8.5 scenario indicate very negative surface mass balances throughout the 21st century (Figure 4.14a). Relative to 1979, Black Rapids Glacier will lose $46.2^{+0.6}_{-1.0}$ Gt by 2100 (Figure 4.15a). Only $2.9^{+1.0}_{-0.6}$ Gt of ice are projected to remain in 2100. The mass loss will be accompanied by glacier retreat, with $51.7^{+8.9}_{-7.5}$ km^2 of glacier area remaining by the end of the 21st century. Figure 4.16a illustrates modeled ice extents for the years 2025, 2050, 2075 and 2100 using probabilities based on extents from the 40 model runs.

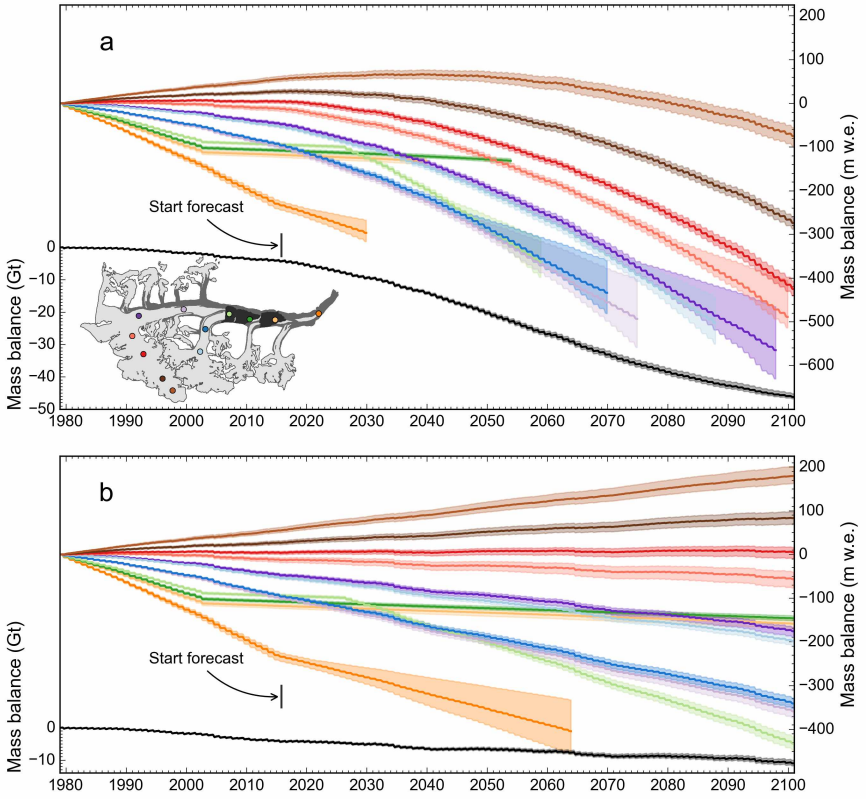

Figure 4.14: Evolution of the glacier wide cumulative mass balance (left axis) and the cumulative mass balances at the index sites (right axis) over the period 1980–2100, using (a) the RCP 8.5 scenario and (b) the constant climate scenario.

By the middle of the century, all index sites will be in the ablation zone, and all but the 2 and 4 km index sites will be deglacierized by the end of the century (Figure 4.14a). The mass balances at the index sites will become increasingly negative, with trends altered locally by the evolving debris cover. Moraine debris has covered index site 38 km since 2015 (according to the last Landsat-derived debris grid), suppressing the site's negative mass balance trend while also increasing the uncertainties (due to the large range of d_m values in our final parameter solutions). The step change in the mass balance trend of site 26 km in 2026 reflects the down-glacier advection of the rockslide debris, which is modeled to give way to moraine debris that year.

Over the course of the projection period, the ELAs rise from today's ~1900 m a.s.l. towards 3000 m a.s.l. and the AARs reach consistently low values around 0.1 (Figure 4.15b). The specific mass balances become increasingly negative, reaching –6 m w.e. in 2080 (Figure 4.15c). This suggests the glacier will evolve into a state of increasing imbalance with the projected climate. Remarkably, this occurs despite the strong glacier retreat (Figure 4.15a), which exerts a negative feedback on the specific mass balances. Only after 2080 is glacier recession sufficient to counteract

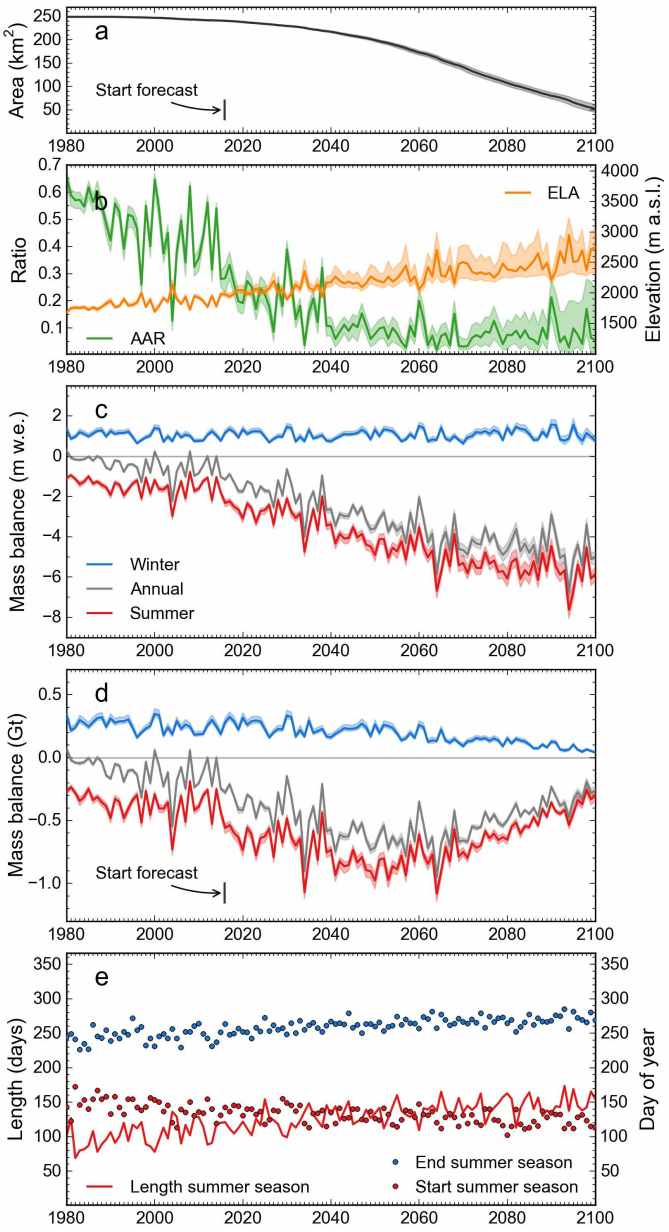

Figure 4.15: Evolution of (a) glacier area, (b) AAR and ELA, and (c–d) annual and seasonal glacier wide (specific) mass balances during the period 1980–2100, using the RCP 8.5 scenario. (e) Evolution of the summer season length (left axis) and start/end dates of the summer seasons (right axis). In (a)–(d), bold colored lines indicate the mean of the results of all parameter combinations while the semi-transparent areas delimit the full range of the results. In (e), lines and points indicate the mean of the 40 parameter combinations.

a further decrease of the specific mass balances. By then, the glacier will have lost most of its valley portion and lie in steeper terrain (Figure 4.16a), which strengthens the negative feedback from

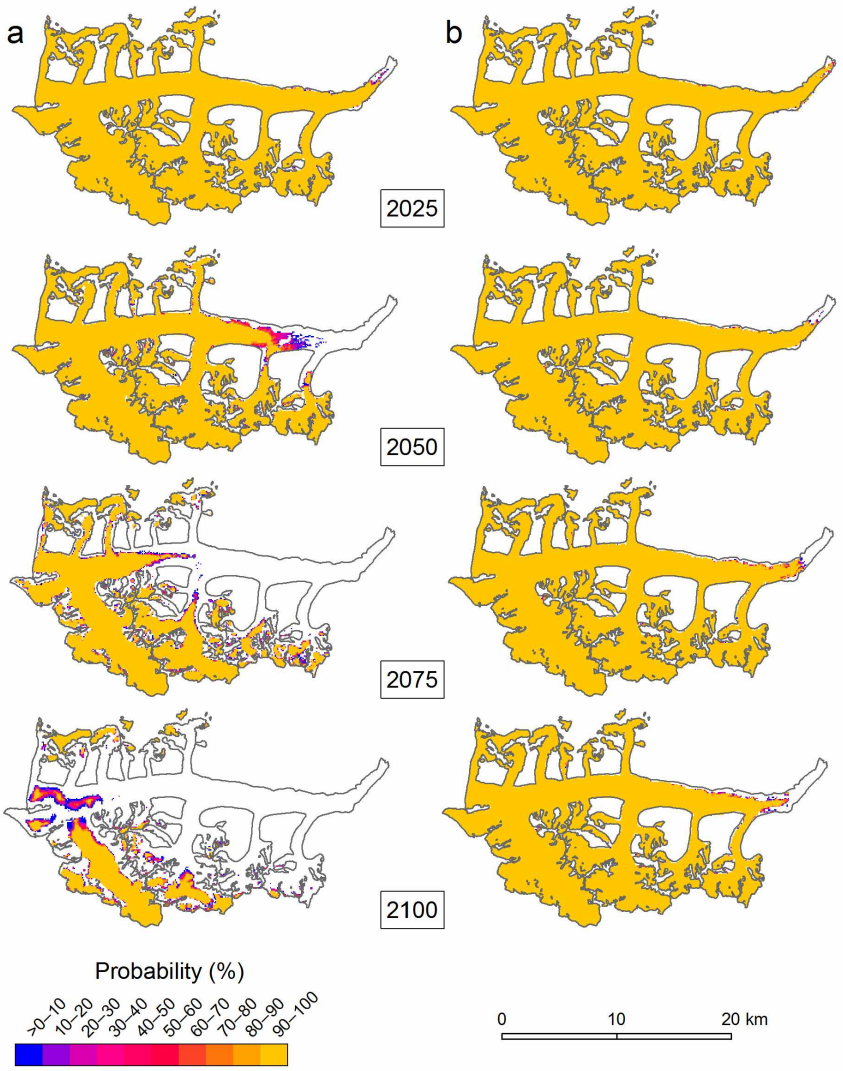

Figure 4.16: Probability for the presence of ice at the four time steps 2025, 2050, 2075 and 2100 for (a) the RCP 8.5 scenario and (b) the constant climate scenario. The probabilities are calculated from the stacked extents, where one extent reflects one mass balance parameter combination.

retreat. To ultimately stabilize the glacier, a trend towards a balanced mass budget is required, however, such a trend is not projected by the model. Given the small glacier area above 2100's projected ELA (~3000 m a.s.l.), Black Rapids Glacier will likely vanish almost completely within the first decades of the 22nd century.

Throughout the projection period, the winter seasons become significantly shorter (decreasing from ~250 to 200 days) due to both earlier onset and delayed termination of the summer season (which increases in length from ~100 to 150 days, Figure 4.15e). Yet the specific winter balances remain constant over the entire period (Figure 4.15c), likely due to the projected precipitation

increase and the glacier's retreat to higher elevations, where precipitation is increased due to orographic effects. The negative progression of the annual balances is thus caused solely by the summer balances, which become very negative due to both higher temperatures and longer summer seasons.

The behavior of the glacier wide mass loss, which is closely related to the glacier runoff, deviates from the glacier wide specific mass balance. The mass loss increases initially, but flattens out at around 2040 and starts to decrease after around 2060 (Figure 4.15d). By that time, the glacier will have shrunk sufficiently that the glacier wide mass loss will decrease despite record-negative specific mass balances. This implies Black Rapids' annual runoff will reach its maximum around the period 2050–2070 and then decrease sharply. In 2100, the runoff may have similar magnitude to that of today, however, it may differ in timing. The glacier runoff will also enter the watershed much higher in elevation than today.

4.6.2.2 Constant climate scenario

The constant climate scenario, repeating the climate of the period 1985–2010, indicates negative mass balances and glacier retreat, however, with changes much less distinct than modeled for the RCP 8.5 scenario. $226.5^{+1.4}_{-1.2}$ km^2 of glacier area are projected to remain by the end of the 21st century (Figure 4.16b). The corresponding mass loss is $10.9^{+0.8}_{-0.9}$ Gt since 1979 (Figures 4.14b, 4.17).

Continuing the trend from the hindcasting period, index sites 2 and 4 km gain ~180 and 80 m w.e. over the 120 year period modeled, thus lying in the accumulation zone. Site 8 km lies at the equilibrium line while the remaining sites are in the ablation zone. Only the lowermost index site (38 km) will be deglacierized before 2100, at around 2030.

The glacier wide annual mass loss is decreasing slightly over the course of the projection period, reflecting the decrease in glacier area (Figure 4.17d). In contrast, the annual specific mass balance shows a very slight negative trend (Figure 4.17c), suggesting that the positive feedback due to glacier thinning (the climate-elevation feedback) is slightly stronger than the negative feedback due to glacier retreat. Both the thick ice and the low slope surface of Black Rapids' main trunk explain the relative strength of the climate-elevation feedback (and similarly the weakness of the retreat feedback). With the climate-elevation feedback competing effectively, Black Rapids Glacier remains in a state of imbalance throughout the projection period, suggesting continued retreat after 2100.

The fact that Black Rapids Glacier is unlikely to achieve a balanced state in the 21st century, even under constant climate, raises the question how much of its valley portion it could support longer term if the current climate prevailed. To assess this question, we ran the glacier model until 2700, repeating the constant climate every 35 years (Figure 4.18). The results suggest strong retreat,

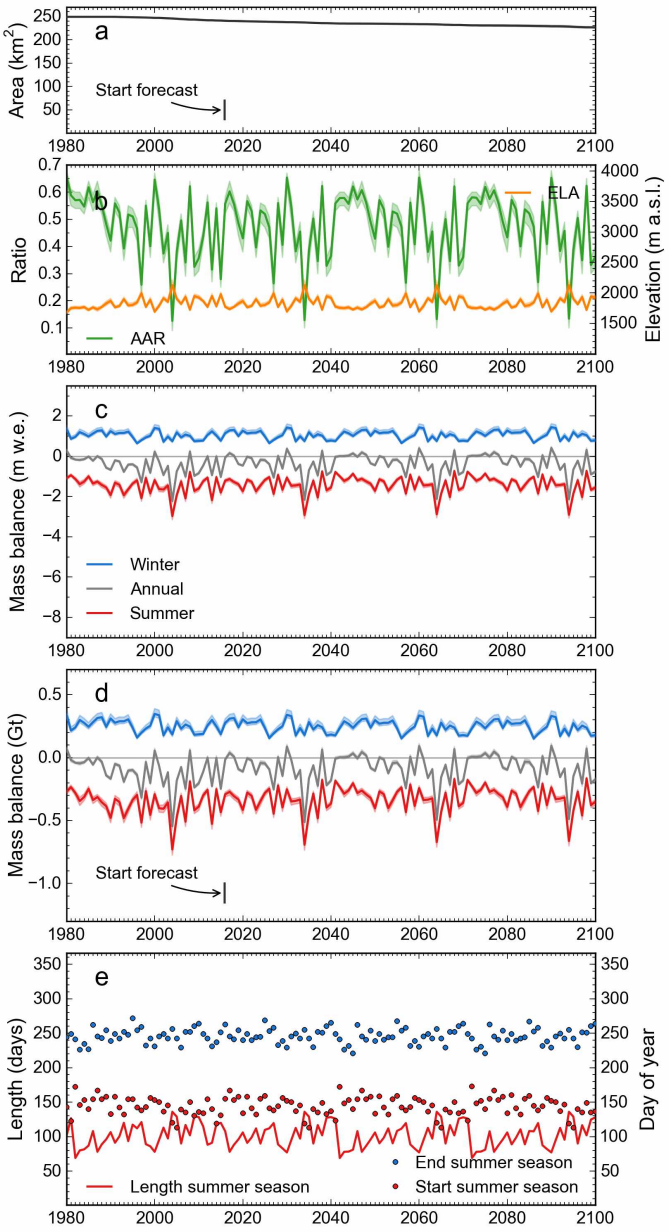

Figure 4.17: Evolution of (a) glacier area, (b) AAR and ELA and (c–d) annual and seasonal glacier wide (specific) mass balances during the period 1980–2100, using the constant climate scenario. (e) Evolution of the summer season length (left axis) and start/end dates of the summer seasons (right axis). In (a)–(d), bold colored lines indicate the mean of the results of all parameter combinations while the semi-transparent areas delimit the full range of the results. In (e), lines and points indicate the mean of the 40 parameter combinations.

with only ~160 km^2 of glacier area remaining in 2700. Black Rapids is projected to gradually approach steady state towards the end of the modeling period, with 35 year averages of the

specific mass balances close to zero and AARs around 0.6. The fact that the glacier continues to retreat in 2700 is due to the recurring extremely negative mass balance years (the extreme year 2004 is repeated every 35 years). Note that the actual (but unknown) recurrence interval of such extreme mass balance years may be longer; if this were the case, Black Rapids would approach steady state faster. Additional uncertainties arise from debris cover, which is very challenging to project on the time scale of this long-term experiment, and the fact that the Δh-parametrization is not ideal for positive mass balance years (i.e., not allowing for glacier advance), which occur increasingly towards the end of the modeling period.

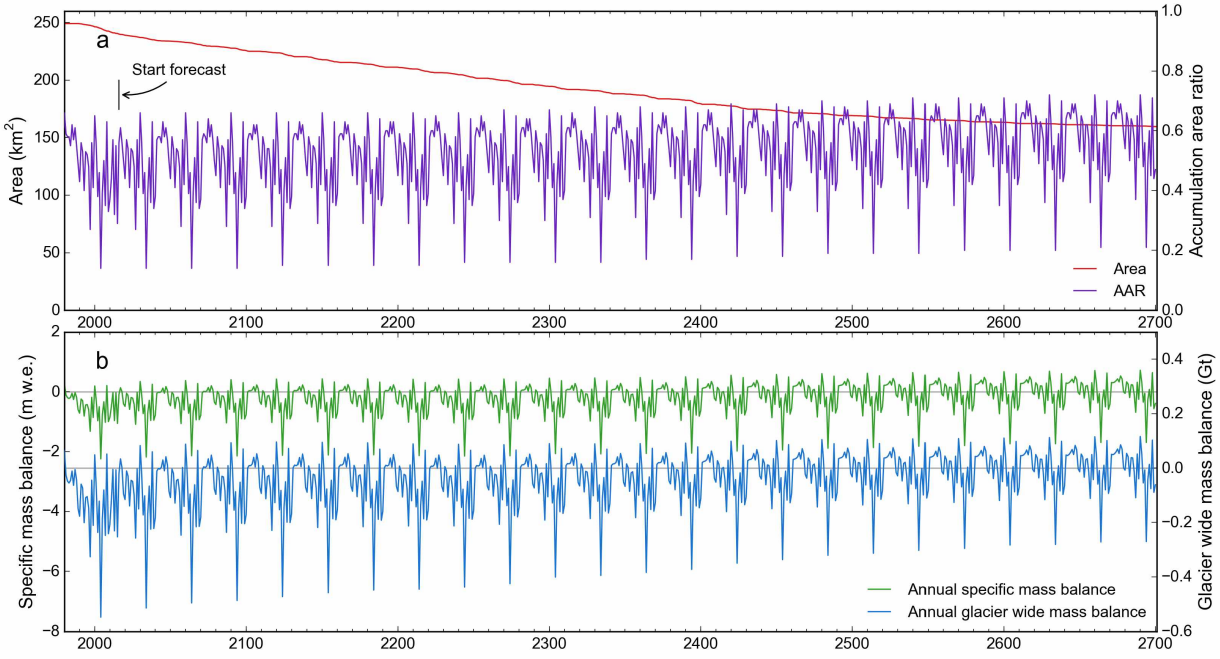

Figure 4.18: Evolution of (a) glacier area and accumulation area ratio and (b) annual specific and glacier wide mass balances over the period 1980–2700, repeating the constant climate scenario.

Despite its large uncertainties, this experiment highlights Black Rapids' distinct sensitivity to climate change and demonstrates the long time scales over which this glacier adjusts its shape. Both high sensitivity to climate change and long adjustment time scales are a result of Black Rapids' thick, low-slope valley portion. Many of the large glaciers in the Eastern Alaska Range have similar geometries and thus may be in a similarly distinct state of imbalance.

4.6.3 Implications for surge likelihood

While the mechanisms for surge initiation are not fully understood (e.g., Harrison and Post, 2003), it is commonly accepted that the surge reservoir needs to reach a certain critical geometry for a

next surge to occur. Slope and ice thickness both control the glacier's basal shear stress, which may ultimately trigger a surge upon reaching critical level. Black Rapids' critical geometry is unknown due to the lack of observations prior to the 1936–37 surge. For the same reason, precise delineation of Black Rapids' surge reservoir is difficult, though the reservoir most likely encompasses the entire area above index site 20 km (i.e., above the Loket confluence, Heinrichs et al. (1995)). Our analysis focuses on the surge reservoir of Black Rapids' main branch, given the availability of in situ elevation and mass balance measurements, and the fact that surge initiation most likely occurs in this area. As all current branches of Black Rapids Glacier participated in the 1936–37 surge (Heinrichs et al., 1996), each branch technically has a separate surge reservoir.

With the glacier geometry considered a key factor for surge initiation, our surge likelihood assessment focuses on the reservoir's response to the negative mass balance trend. In the case of Black Rapids, surface elevation changes were measured at individual index sites over parts of the hindcasting period (Heinrichs et al., 1995; Truffer et al., 2005). Combined with surface mass balance measurements, they allow for the derivation of time-averaged ice flow emergence velocities, which in turn allow converting the modeled mass balance time series into continuous surface elevation time series. We calculated such elevation time series for the index sites 4, 8, 14 and 20 km, all of which are located in the surge reservoir. The emergence velocities at these four sites, –0.75, –0.10, 1.00 and 2.25 m w.e. a^{-1}, were derived from surface elevation changes between 1980 and 2010 (Kienholz et al., 2016) and the corresponding cumulative surface mass balances. To hypothesize about the surface elevation changes in the near future, we continued the time series until 2035, based on the modeled surface mass balances from the RCP 8.5 scenario. We refrained from projections beyond 2035 as the assumption of constant emergence velocities becomes increasingly unrealistic (changing glacier geometry may affect ice flow considerably). Even for the hindcasting period, the assumption of constant emergence velocities is uncertain in light of Black Rapids' complex flow behavior (Heinrichs et al., 1996). As a consequence, the temporal variations in the derived surface elevations need to be interpreted cautiously.

Figure 4.19 shows the mass balance, emergence velocity and elevation change time series from 1979 to 2035. From the start of the modeling period until ~1988, the computed cumulative elevation changes indicate ice thickening at all four sites. This period corresponds to the period with relatively favorable glacier wide mass balances (Section 4.6.1). Interestingly, neighboring West Fork Glacier surged in 1987–88 (Harrison et al., 1994), just at the end of this period. The negative trend after 1988 includes all four sites, however, it is particularly pronounced for the two lower-lying sites 14 and 20 km. While they are calculated to lose ~9 and 15 m over the entire hindcasting period, the net elevation change at the sites 4 and 8 km is close to zero. Over the forecasting period, the projected elevation loss becomes increasingly pronounced due to the very

negative mass balances under the RCP 8.5 scenario. Assuming constant emergence velocities, the index sites' locations are projected to lose between ~30 (site 4 km) and 60 m (site 20 km) of ice until 2035.

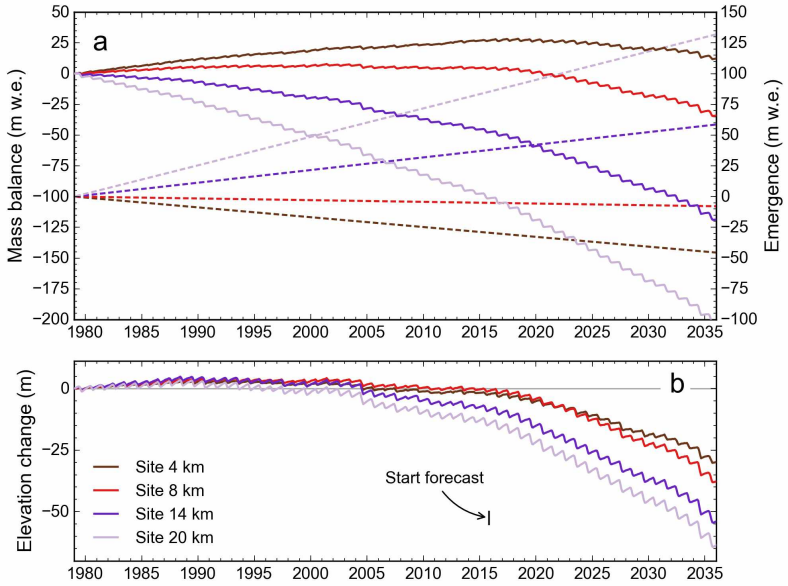

Figure 4.19: (a) Cumulative surface mass balance (solid lines, left axis) and ice flow emergence (dashed lines, right axis) for four selected index sites in the surge reservoir, over the time period 1979–2035. (b) Cumulative elevation change, corresponding to the difference between surface mass balance and flow emergence. The vertical scale in (b) is twice as large as in (a).

Overall, these results indicate a surge is unlikely to occur in the near future due to mass starvation and corresponding lack of thickening in the reservoir area. This conclusion, which supports conjectures from previous studies (Kienholz et al., 2016), applies to the current climate and to the projected climate under the RCP 8.5 scenario. To re-initiate thickening in the surge reservoir, the surface mass balances would need to be at least as favorable as they were in the early 1980s.

4.7 Conclusions

We employed a surface mass balance model coupled to a parametrized glacier dynamics model to assess the evolution of surge-type Black Rapids Glacier throughout the 21st century. The mass balance model was forced by daily temperature and precipitation fields. In the case of the 35 year hindcasting period 1980–2015, they originated from dynamically downscaled ERA-Interim data with 20 km spatial resolution (Bieniek et al., 2016). For the 85 year forecasting period 2015–2100, both a constant climate scenario (repeating the 1985–2010 climate) and a warming climate scenario

(corresponding to the GFDL-CM 3 RCP 8.5 scenario, Lader et al., in preparation) were applied. The reanalysis provided by Bieniek et al. (2016) was applied for the first time in a glaciological study. Its quality marks a step forward compared to climate data used in previous glacier studies in Alaska (e.g., Ziemen et al., 2016).

Six parameters were calibrated for the mass balance model through application of a grid search procedure. Calibration and validation were based on three geodetic mass balances, ~250 in situ mass balance measurements and >300 snowline elevations. Considering the uncertainties in the calibration data, we selected a set of 40 best parameter combinations by means of a Monte Carlo approach. We then modeled the glacier evolution for each parameter combination, which quantified the uncertainties arising from applying different (but similarly good) combinations. This improves on the widely used approach of choosing one single optimal parameter combination (e.g., the parameter combination with the lowest rmse), which lacks this uncertainty information as a consequence.

The modeling indicates Black Rapids Glacier is far out of balance, both with respect to the current and the projected climate. Only for the early hindcasting period (1980–1988), the glacier model shows approximate equilibrium. A negative mass balance trend emerges thereafter and continues through the forecasting period. With the constant climate scenario, Black Rapids is projected to lose ~10% of its 1980 area and ~22% of its 1980 mass by 2100. By 2100, Black Rapids Glacier will not have achieved a state of equilibrium with the climate, even under constant climate. Additional retreat will thus occur after 2100, ultimately causing the loss of large parts of Black Rapids' valley portion. With the GFDL-CM3 RCP 8.5 scenario, the modeled glacier wastage is yet accelerated, with ~80% area and ~94% mass loss relative to 1980. The small glacier portions remaining will be in a very strong state of imbalance with the climate and vanish in the first decades of the 22nd century, except for a few ice remnants above 2100's projected ELA (lying at 3000 m a.s.l.).

Although the RCP 8.5 scenario assumes rapidly increasing greenhouse gas emissions and thus projects substantial radiative forcing (8.5 W m^{-2}, Riahi et al., 2011), this scenario may be more likely to occur than the constant climate scenario, in light of the recent evolution of the greenhouse gas emissions (Sanford et al., 2014). While the three remaining RCP scenarios (RCP 6, RCP 4.5 and RCP 2.6) have not been modeled as part of this study, the corresponding projections would lie within the projections from our two scenarios (each of the scenarios assumes slower increase of the greenhouse gas emissions than RCP 8.5). Note that the downscaled versions of these RCP scenarios were unavailable at the time of the analysis, preventing us from using them in our modeling efforts.

While the choice of the climate scenario is likely the single most important source of uncertainty, our projections are subject to additional uncertainties not currently considered in our uncertainty estimates. For example, the errors in the ice thickness distributions are large in the case of Black Rapids Glacier (mae ~100 m when compared to profiles). With the glacier retreat responding to this quantity directly, substantial uncertainties result in the final projections. Likewise, the future debris evolution comes with large uncertainties. Debris cover affects the modeled surface mass balances, and as such the projected glacier evolution. Note that the uncertainties due to future climate and debris evolution as well as current-date ice thickness do not apply to our hindcasting runs, which have much smaller final uncertainties as a consequence.

Several improvements could help reduce the uncertainties in our results modeled, of which we consider more accurate ice thicknesses most important. Ideally, an improved ice thickness dataset would come with an uncertainty mask, which would allow for propagating the uncertainties into the final results. While sophisticated approaches for the ice thickness derivation exist (e.g., Brinkerhoff et al., 2016), their application requires high quality ice velocity fields, which we do not currently possess for Black Rapids Glacier. Application of an actual ice flow model rather than the Δh-parametrization may further improve our results, however, successful application would warrant higher quality ice thicknesses than currently available. The strength of a flow model would become most evident towards the end of the forecasting period. Applying the same Δh curve repeatedly, the Δh-parametrization cannot account for the glacier's evolving geometry (which ultimately changes ice flow and thus the Δh curve), while an ice flow model can. Also, given the application of a single Δh curve, the Δh-parametrization is a priori unable to reproduce thinning rates that vary among branches, which applies to Black Rapids Glacier (Kienholz et al., 2016). Besides modeling a more realistic glacier evolution, a flow model would yield ice flow velocities that can be used for sophisticated projections of future debris cover (e.g., Rowan et al., 2015).

Although the used climate reanalysis sets high quality standards, its spatial resolution remains low compared to the resolution of a typical glacier model. In our case, this required application of an additional downscaling step. The statistical downscaling used is crude, for example, it fails to conserve mass and energy. WRF-downscaled ERA-Interim data with higher spatial resolution would be ideal to mitigate potential problems arising from this additional downscaling step. In the absence thereof, the additional downscaling from 20 km to 100 m may be improved by applying a more sophisticated downscaling approach, for example, based on a model that applies the linear theory of orographic precipitation (Smith and Barstad, 2004). Likewise, given the absence of a debris thickness map, the modeling of the debris melt suppression remained crude. To apply a more sophisticated approach (e.g., Reid et al., 2012; Carenzo et al., 2016), a debris

thickness map should be obtained in the future, by combining new remotely sensed techniques (e.g., Schauwecker et al., 2015) and in situ debris thickness measurements. Given its wide range of debris types/thicknesses and its close proximity to infrastructure, Black Rapids Glacier would be ideal to study melt suppression under debris.

4.8 Acknowledgements

We thank R. Wastlhuber for processing one of the snow line elevation datasets. A. Roth is acknowledged for help with the model code development. K. Echelmeyer, M. Stuefer, and R. Flanders were instrumental in maintaining the mass balance program on Black Rapids Glacier during the 1990s and 2000s. C. Larsen has been important for the mass balance program over the recent years and also co-led the research program on Black Rapids from 2012–2014. This work was funded by grants from the National Science Foundation (OPP-1107491), the National Aeronautics and Space Administration (NNX11AF41G) and the U.S. Department of the Interior Climate Science Center. C. Kienholz was also funded by a fellowship from the University of Alaska Fairbanks Graduate School.

References

Anderson, B., W. Lawson, and I. Owens (2008). Response of Franz Josef Glacier Ka Roimata o Hine Hukatere to climate change. *Global and Planetary Change 63*(1), 23–30.

Anderson, B., W. Lawson, I. Owens, and B. Goodsell (2006). Past and future mass balance of 'Ka Roimata o Hine Hukatere' Franz Josef Glacier, New Zealand. *Journal of Glaciology 52*(179), 597–607.

Arendt, A., J. Walsh, and W. Harrison (2009). Changes of glaciers and climate in northwestern North America during the late twentieth century. *Journal of Climatology 22*(15), 4117–4134.

Bevington, A. and L. Copland (2014). Characteristics of the last five surges of Lowell Glacier, Yukon, Canada, since 1948. *Journal of Glaciology 60*(219), 113–123.

Bieniek, P. A., U. S. Bhatt, R. L. Thoman, H. Angeloff, J. Partain, J. Papineau, F. Fritsch, E. Holloway, J. E. Walsh, C. Daly, M. Shulski, G. Hufford, D. Hill, S. Calos, and R. Gens (2012). Climate divisions for Alaska based on objective methods. *Journal of Applied Meteorology and Climatology 51*(7), 1276–1289.

Bieniek, P. A., U. S. Bhatt, J. E. Walsh, T. S. Rupp, J. Zhang, J. R. Krieger, and R. Lader (2016). Dynamical downscaling of ERA-Interim temperature and precipitation for Alaska. *Journal of Applied Meteorology and Climatology 55*(3), 635–654.

Bieniek, P. A., J. E. Walsh, R. L. Thoman, and U. S. Bhatt (2014). Using climate divisions to analyze variations and trends in Alaska temperature and precipitation. *Journal of Climate 27*(8), 2800–2818.

Brinkerhoff, D. J., A. Aschwanden, and M. Truffer (2016). Bayesian Inference of Subglacial Topography Using Mass Conservation. *Frontiers in Earth Science 4*, 1–8.

Brooks, P. D. (1988). The Alaska High-Altitude Aerial Photography (AHAP) Program. Technical report, State of Alaska.

Carenzo, M., F. Pellicciotti, J. Mabillard, T. Reid, and B. Brock (2016). An enhanced temperature index model for debris-covered glaciers accounting for thickness effect. *Advances in Water Resources 94*, 457–469.

Cogley, J. G., R. Hock, L. A. Rasmussen, A. A. Arendt, R. J. Bauder, A.and Braithwaite, P. Jansson, G. Kaser, M. Möller, L. Nicholson, et al. (2011). Glossary of glacier mass balance and related terms. *IHP-VII Technical Documents in Hydrology 86*.

Daly, C., R. P. Neilson, and D. L. Phillips (1994). A Statistical-Topographic Model for Mapping Climatological Precipitation over Mountainous Terrain. *Journal of Applied Meteorology 33*(2), 140–158.

Dee, D., S. Uppala, A. Simmons, P. Berrisford, P. Poli, S. Kobayashi, U. Andrae, M. Balmaseda, G. Balsamo, P. Bauer, et al. (2011). The ERA-Interim reanalysis: Configuration and performance of the data assimilation system. *Quarterly Journal of the Royal Meteorological Society 137*(656), 553–597.

Donner, L. J., B. L. Wyman, R. S. Hemler, L. W. Horowitz, Y. Ming, M. Zhao, J.-C. Golaz, P. Ginoux, S.-J. Lin, M. D. Schwarzkopf, et al. (2011). The dynamical core, physical parameterizations, and basic simulation characteristics of the atmospheric component AM3 of the GFDL global coupled model CM3. *Journal of Climate 24*(13), 3484–3519.

Eisen, O., W. Harrison, and C. Raymond (2001). The surges of Variegated Glacier, Alaska, USA, and their connection to climate and mass balance. *Journal of Glaciology 47*(158), 351–358.

Elsberg, D. H., W. D. Harrison, K. A. Echelmeyer, and R. M. Krimmel (2001). Quantifying the effects of climate and surface change on glacier mass balance. *Journal of Glaciology 47*(159), 649–658.

Flowers, G., N. Roux, S. Pimentel, and C. Schoof (2011). Present dynamics and future prognosis of a slowly surging glacier. *The Cryosphere 5*(1), 299–313.

Gades, A. M. (1998). *Spatial and temporal variations of basal conditions beneath glaciers and ice sheets inferred from radio echo soundings*. Ph. D. thesis, University of Washington.

Gusmeroli, A., G. J. Wolken, and A. A. Arendt (2014). Helicopter-borne radar imaging of snow cover on and around glaciers in Alaska. *Annals of Glaciology 55*(67), 78–88.

Harrison, W., K. Echelmeyer, E. Chacho, C. Raymond, and R. Benedict (1994). The 1987–88 surge of West Fork Glacier, Susitna Basin, Alaska, USA. *Journal of Glaciology 40*(135), 241–254.

Harrison, W. D. and A. S. Post (2003). How much do we really know about glacier surging? *Annals of Glaciology 36*, 1–6.

Heinrichs, T., L. Mayo, D. Trabant, and R. March (1995). Observations of the surge-type Black Rapids Glacier, Alaska, during a quiescent period, 1970–92. Open-file report 94-512, U.S. Geological Survey.

Heinrichs, T. A., L. Mayo, K. Echelmeyer, and W. Harrison (1996). Quiescent-phase evolution of a surge-type glacier: Black Rapids Glacier, Alaska, USA. *Journal of Glaciology 42*(140), 110–122.

Hock, R. (1999). A distributed temperature-index ice- and snowmelt model including potential direct solar radiation. *Journal of Glaciology 45*(149), 101–111.

Hulth, J., C. Rolstad Denby, and R. Hock (2013). Estimating glacier snow accumulation from backward calculation of melt and snowline tracking. *Annals of Glaciology 54*(62), 1–7.

Huss, M. and D. Farinotti (2012). Distributed ice thickness and volume of all glaciers around the globe. *Journal of Geophysical Research 117*(F4), F04010.

Huss, M., G. Jouvet, D. Farinotti, and A. Bauder (2010). Future high-mountain hydrology: a new parameterization of glacier retreat. *Hydrology and Earth System Sciences 14*(5), 815–829.

Kienholz, C., S. Herreid, J. Rich, A. Arendt, R. Hock, and E. Burgess (2015). Derivation and analysis of a complete modern-date glacier inventory for Alaska and northwest Canada. *Journal of Glaciology 61*(227), 403–420.

Kienholz, C., R. Hock, M. Truffer, A. A. Arendt, and S. Arko (2016). Geodetic mass balance of surge-type Black Rapids Glacier, Alaska, 1980–2001–2010, including role of rockslide deposition and earthquake displacement. *Journal of Geophysical Research: Earth Surface 121*, 1–24.

Lader, R. T., J. E. Walsh, U. S. Bhatt, and P. A. Bieniek (in preparation). Projections of 21st century climate extremes for Alaska via dynamical downscaling. *Journal of Applied Meteorology and Climatology*.

Lang, H. (1968). Relations between glacier runoff and meteorological factors observed on and outside the glacier. In *IUGG General Assembly, Berne, International Association of Scientific Hydrology*, Number 79, pp. 429–439.

Larsen, C., E. Burgess, A. Arendt, S. O'Neel, A. Johnson, and C. Kienholz (2015). Surface melt dominates Alaska glacier mass balance. *Geophysical Research Letters 42*(14), 5902–5908.

Machguth, H., F. Paul, S. Kotlarski, and M. Hoelzle (2009). Calculating distributed glacier mass balance for the Swiss Alps from regional climate model output: A methodical description and interpretation of the results. *Journal of Geophysical Research: Atmospheres 114*(D19), D19106.

McGrath, D., L. Sass, S. O'Neel, A. Arendt, G. Wolken, A. Gusmeroli, C. Kienholz, and C. McNeil (2015). End-of-winter snow depth variability on glaciers in Alaska. *Journal of Geophysical Research: Earth Surface 120*(8), 1530–1550.

Pfeffer, W. T., A. A. Arendt, A. Bliss, T. Bolch, J. G. Cogley, A. S. Gardner, J. O. Hagen, R. Hock, G. Kaser, C. Kienholz, E. S. Miles, G. Moholdt, N. Mölg, F. Paul, V. Radić, P. Rastner, B. H. Raup,

J. L. Rich, and M. J. Sharp (2014). The Randolph Glacier Inventory: a globally complete inventory of glaciers. *Journal of Glaciology 60*(221), 537–552.

Radić, V., A. Bliss, A. C. Beedlow, R. Hock, E. Miles, and J. G. Cogley (2014). Regional and global projections of twenty-first century glacier mass changes in response to climate scenarios from global climate models. *Climate Dynamics 42*(1), 37–58.

Reid, T., M. Carenzo, F. Pellicciotti, and B. Brock (2012). Including debris cover effects in a distributed model of glacier ablation. *Journal of Geophysical Research: Atmospheres 117*(D18), D18105.

Riahi, K., S. Rao, V. Krey, C. Cho, V. Chirkov, G. Fischer, G. Kindermann, N. Nakicenovic, and P. Rafaj (2011). RCP 8.5–A scenario of comparatively high greenhouse gas emissions. *Climatic Change 109*(1), 33–57.

Rowan, A. V., D. L. Egholm, D. J. Quincey, and N. F. Glasser (2015). Modelling the feedbacks between mass balance, ice flow and debris transport to predict the response to climate change of debris-covered glaciers in the Himalaya. *Earth and Planetary Science Letters 430*, 427–438.

Sanford, T., P. C. Frumhoff, A. Luers, and J. Gulledge (2014). The climate policy narrative for a dangerously warming world. *Nature Climate Change 4*(3), 164–166.

Schaefer, M., H. Machguth, M. Falvey, and G. Casassa (2013). Modeling past and future surface mass balance of the Northern Patagonia Icefield. *Journal of Geophysical Research: Earth Surface 118*(2), 571–588.

Schauwecker, S., M. Rohrer, C. Huggel, A. Kulkarni, A. Ramanathan, N. Salzmann, M. Stoffel, and B. Brock (2015). Remotely sensed debris thickness mapping of Bara Shigri Glacier, Indian Himalaya. *Journal of Glaciology 61*(228), 675–688.

Sevestre, H. and D. I. Benn (2015). Climatic and geometric controls on the global distribution of surge-type glaciers: implications for a unifying model of surging. *Journal of Glaciology 61*(228), 646–662.

Shugar, D. H. and J. J. Clague (2011). The sedimentology and geomorphology of rock avalanche deposits on glaciers. *Sedimentology 58*(7), 1762–1783.

Shugar, D. H., B. T. Rabus, and J. J. Clague (2010). Elevation changes (1949–1995) of Black Rapids Glacier, Alaska, derived from a multi-baseline InSAR DEM and historical maps. *Journal of Glaciology 56*(198), 625–634.

Skamarock, W. C., J. B. Klemp, J. Dudhia, D. O. Gill, D. M. Barker, D. M. G., X. Huang, W. Wang, and J. G. Powers (2008). A Description of the Advanced Research WRF Version 3. Technical report, NCAR Technical Notes, Boulder, Colorado, USA.

Smith, R. B. and I. Barstad (2004). A linear theory of orographic precipitation. *Journal of the Atmospheric Sciences 61*(12), 1377–1391.

Sold, L., M. Huss, M. Hoelzle, H. Andereggen, P. C. Joerg, and M. Zemp (2013). Methodological approaches to infer end-of-winter snow distribution on alpine glaciers. *Journal of Glaciology 59*(218), 1047–1059.

Truffer, M., W. D. Harrison, and R. S. March (2005). Record negative glacier balances and low velocities during the 2004 heatwave in Alaska, USA: implications for the interpretation of observations by Zwally and others in Greenland. *Journal of Glaciology 51*(175), 663–664.

Trüssel, B. L., M. Truffer, R. Hock, R. J. Motyka, M. Huss, and J. Zhang (2015). Runaway thinning of the low-elevation Yakutat Glacier, Alaska, and its sensitivity to climate change. *Journal of Glaciology 61*(225), 65–75.

Ziemen, F., R. Hock, A. Aschwanden, C. Khroulev, C. Kienholz, A. Melkonian, and J. Zhang (2016). Modeling the evolution of the Juneau Icefield between 1971 and 2100 using the Parallel Ice Sheet Model (PISM). *Journal of Glaciology 62*(231), 199–214.

Appendix 4.A Snow line derivation

We initiated the snow line derivation by searching the USGS EarthExplorer archive for cloud-free or partially cloudy (< 40% cloud coverage) Landsat scenes taken between May and September. This yielded 77 Landsat scenes, from which we excluded scenes with the snow line below the glacier terminus and scenes too obscured by clouds. We also excluded scenes where we could not distinguish the snow line from the firn line, which was a recurring problem toward the end of the melt season. Overall, 59 scenes proved usable.

Figure 4.A-1 shows a flow chart of the steps applied. In the first step, the original Landsat scenes are converted to false-color composites and automatically added to a GIS project file with the glacier outlines of that scene (one project file per satellite scene, zoomed in to the glacier). Next, the glacier polygons are clipped manually along the ice-snow or firn-snow boundary and allocated to the two categories ice/firn and snow. The snow lines are then extracted automatically by comparing the original glacier polygons to the adapted annotated ice/firn and snow polygons. Finally, the DEM is sampled along the snow lines and the elevation statistics for each individual glacier branch are derived (mean and standard deviation, as well as median and quartiles).

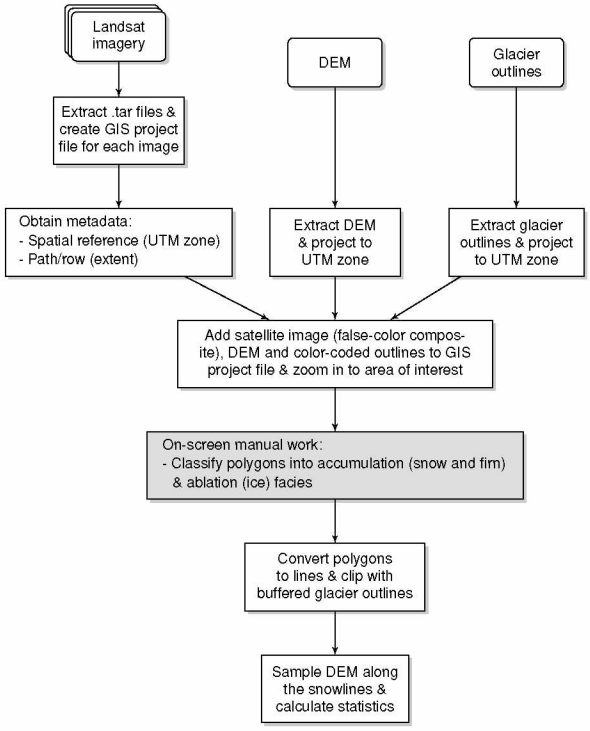

Figure 4.A-1: Flow chart illustrating the main steps of the snow line derivation workflow. The gray box indicates the manual step.

Chapter 5

General Conclusions

We compiled a glacier database for Alaska and neighboring Canada using satellite data taken between 2000 and 2011. The inventory yielded 27,100 glaciers (86,720 km^2 of ice, equivalent to ~12% of the global glacierized area outside the ice sheets), for which we derived outlines and more than 50 variables, including centerline lengths, outline types, and debris cover. In terms of area covered and inventory variables, this study is among the most complete regional scale inventory studies published. Beyond the inventory analysis, our goal was to provide key input data for other glaciology-related studies. We thus submitted the outlines to the global Randolph Glacier Inventory (RGI, Pfeffer et al., 2014), where they are freely available (http://www.glims.org/RGI/randolph.html). Since the study's publication in the Journal of Glaciology in 2015, several studies have taken advantage of the new data, among them Alaska wide observational studies (e.g., Fahnestock et al., 2015; Larsen et al., 2015) and regional (Ziemen et al., 2016) to global (Huss and Hock, 2015) modeling studies. Several other studies employing the inventory data are currently in preparation.

The inventory study resulted in the first Alaska wide glacier database and thus the first accurate snapshot of Alaska's glaciers. Unlike other inventory studies (e.g., Bolch et al., 2010), we did not determine glacier changes (e.g., area changes), because comprehensive glacier inventories from earlier dates were unavailable on an Alaska wide scale. While topographic maps from the 1950s exist for all of Alaska, the quality of their glacier outlines varies considerably, hampering direct comparisons (Le Bris et al., 2011; Loso et al., 2014). An Alaska wide 1950–2010 glacier comparison remains useful and should be attempted in a future study. Such a project should attempt to derive outlines from the original 1950 aerial imagery directly, which are archived and available online (e.g., through the USGS EarthExplorer website, http://earthexplorer.usgs.gov). Newly available data (e.g., accurate DEMs for ground control) combined with modern processing algorithms (e.g., structure from motion algorithms) would allow for efficient reprocessing of the imagery. Unfortunately, the images' subideal dates (sometimes taken in the early melt season) remain a problem for the derivation of high quality 1950 outlines across the state.

Future updates of the Alaska wide inventory should occur on a regular schedule, every ~20 to 25 years. Given the uncertainties in the glacier outlines, more frequent updates may not gain sufficient insight to justify this costly procedure more often. For glaciers undergoing very large changes (e.g., tidewater glaciers, McNabb and Hock, 2014), more frequent updates are recommended. In the future, new satellite data and improved algorithms for the derivation of outlines may make more frequent inventory updates feasible Alaska wide.

Following the Alaska wide inventory work, we conducted two case studies on Black Rapids Glacier, Eastern Alaska Range, to assess its evolution over the 1980–2001–2100 period through observations and modeling. Observed glacier shrinkage since 1980 and modeled future retreat showed Black Rapids Glacier in a severe state of disequilibrium with the climate. The measured and predicted surface mass balances were sufficiently negative that we assessed Black Rapids' surge likelihood to be low under current and anticipated future climate conditions. Given its thick, long and low-slope valley portion, Black Rapids Glacier is very susceptible to climate change. Many glaciers in the Eastern Alaska Range have similar characteristics, suggesting region wide glacier retreat in the future. To constrain this further, the Black Rapids case study should be extended to the entire Eastern Alaska Range (185 glaciers > 1 km^2, ~2650 km^2 of ice), similar to studies in neighboring regions (e.g., Clarke et al., 2015; Ziemen et al., 2016). While previous glaciological studies modeled the evolution of all Alaska glaciers already (Marzeion et al., 2012; Radić et al., 2014; Huss and Hock, 2015), these studies had a global scope and thus constraints on the modeling and analysis side (e.g., by excluding the effects of supraglacial debris or by analyzing the results for large regions only), which makes application of a regional model worthwhile.

While some of our model code will allow for immediate application to the Alaska Range scale (e.g., facilitated by the relational database interface), other code will need adaptations beforehand. The simple statistical downscaling of the climate data, which proved sufficient for Black Rapids Glacier, will likely fail on a regional scale, especially with regard to precipitation (e.g., Machguth et al., 2009). A more sophisticated downscaling approach, for example based on the linear theory of orographic precipitation (Smith and Barstad, 2004), may need to be implemented instead. Likewise, application of a full parameter grid search for the calibration will not be feasible due to the larger computational resources needed when modeling on a regional scale. A more sophisticated approach, for example a Shuffled Complex Evolution Metropolis algorithm (Vrugt et al., 2003), will likely need to be implemented. The availability of sufficient calibration data, often a challenge for the calibration of regional glacier models, is promising in the case of the Eastern Alaska Range. A considerable number of glaciers are covered by laser altimetry data, allowing for the derivation of geodetic mass balances (Larsen et al., 2015). Both Black Rapids and Gulkana Glaciers have a high number of in situ mass balance measurements collected over several decades (Heinrichs et al., 1995; O'Neel et al., 2014). Moreover, a range of in situ measurements were conducted on the glaciers in the Susitna River watershed (southern part of the Hayes Range) during the 1980s (Harrison et al., 1994) and from 2012 to 2015 (Gusmeroli et al., 2014; Wolken et al., 2015). Finally, Jarvis Glacier on the northern portion of the Alaska Range has in situ mass balance measurements from recent years (M. Debolskiy, personal communication, 2016). Together with snow lines from satellite data and DEMs from AHAP imagery (both used in the Black Rapids case

studies), sufficient observational data are available for calibrating the glacier model Alaska Range wide. Such regional model application highlights the importance of extensive data collection campaigns for modeling studies. Though costly, such campaigns (e.g., Wolken et al., 2015) should be supported long-term to facilitate future glaciological and hydrological modeling studies.

References

Bolch, T., B. Menounos, and R. Wheate (2010). Landsat-based inventory of glaciers in western canada, 1985-2005. *Remote Sensing of Environment 114*(1), 127–137.

Clarke, G. K., A. H. Jarosch, F. S. Anslow, V. Radić, and B. Menounos (2015). Projected deglaciation of western Canada in the twenty-first century. *Nature Geoscience 8*(5), 372–377.

Fahnestock, M., T. Scambos, T. Moon, A. Gardner, T. Haran, and M. Klinger (2015). Rapid large-area mapping of ice flow using Landsat 8. *Remote Sensing of Environment 185*, 84–94.

Gusmeroli, A., G. J. Wolken, and A. A. Arendt (2014). Helicopter-borne radar imaging of snow cover on and around glaciers in Alaska. *Annals of Glaciology 55*(67), 78–88.

Harrison, W., K. Echelmeyer, E. Chacho, C. Raymond, and R. Benedict (1994). The 1987–88 surge of West Fork Glacier, Susitna Basin, Alaska, USA. *Journal of Glaciology 40*(135), 241–254.

Heinrichs, T., L. Mayo, D. Trabant, and R. March (1995). Observations of the surge-type Black Rapids Glacier, Alaska, during a quiescent period, 1970–92. Open-file report 94-512, U.S. Geological Survey.

Huss, M. and R. Hock (2015). A new model for global glacier change and sea-level rise. *Frontiers in Earth Science 3*(54), 1–22.

Larsen, C., E. Burgess, A. Arendt, S. O'Neel, A. Johnson, and C. Kienholz (2015). Surface melt dominates Alaska glacier mass balance. *Geophysical Research Letters 42*(14), 5902–5908.

Le Bris, R., F. Paul, H. Frey, and T. Bolch (2011). A new satellite-derived glacier inventory for Western Alaska. *Annals of Glaciology 52*(59), 135–143.

Loso, M., A. Arendt, C. F. Larsen, J. L. Rich, and N. Murphy (2014). Alaskan National Park Glaciers: Status and Trends. Technical report, National Park Service, Fort Collins, Colorado.

Machguth, H., F. Paul, S. Kotlarski, and M. Hoelzle (2009). Calculating distributed glacier mass balance for the Swiss Alps from regional climate model output: A methodical description and interpretation of the results. *Journal of Geophysical Research: Atmospheres 114*(D19), D19106.

Marzeion, B., A. H. Jarosch, and M. Hofer (2012). Past and future sea-level change from the surface mass balance of glaciers. *The Cryosphere 6*(6), 1295–1322.

McNabb, R. W. and R. Hock (2014). Alaska tidewater glacier terminus positions, 1948–2012. *Journal of Geophysical Research: Earth Surface 119*(2), 153–167.

O'Neel, S., E. Hood, A. Arendt, and L. Sass (2014). Assessing streamflow sensitivity to variations in glacier mass balance. *Climatic Change 123*(2), 329–341.

Pfeffer, W. T., A. A. Arendt, A. Bliss, T. Bolch, J. G. Cogley, A. S. Gardner, J. O. Hagen, R. Hock, G. Kaser, C. Kienholz, E. S. Miles, G. Moholdt, N. Mölg, F. Paul, V. Radić, P. Rastner, B. H. Raup, J. L. Rich, and M. J. Sharp (2014). The Randolph Glacier Inventory: a globally complete inventory of glaciers. *Journal of Glaciology 60*(221), 537–552.

Radić, V., A. Bliss, A. C. Beedlow, R. Hock, E. Miles, and J. G. Cogley (2014). Regional and global projections of twenty-first century glacier mass changes in response to climate scenarios from global climate models. *Climate Dynamics 42*(1), 37–58.

Smith, R. B. and I. Barstad (2004). A linear theory of orographic precipitation. *Journal of the Atmospheric Sciences 61*(12), 1377–1391.

Vrugt, J. A., H. V. Gupta, W. Bouten, and S. Sorooshian (2003). A Shuffled Complex Evolution Metropolis algorithm for optimization and uncertainty assessment of hydrologic model parameters. *Water Resources Research 39*(8), 1201–1214.

Wolken, G., A. Bliss, R. Hock, E. Whorton, J. Braun, A. Liljedahl, J. Zhang, E. Youcha, J. Schulla, A. Gusmeroli, C. Aubry-Wake, C. Beedlow, and A. Hoffman (2015). Susitna-Watana Hydroelectric Project: Glacier and Runoff Changs Study. Technical report, Division of Geological & Geophysical Surveys, Alaska Department of Natural Resources.

Ziemen, F., R. Hock, A. Aschwanden, C. Khroulev, C. Kienholz, A. Melkonian, and J. Zhang (2016). Modeling the evolution of the Juneau Icefield between 1971 and 2100 using the Parallel Ice Sheet Model (PISM). *Journal of Glaciology 62*(231), 199–214.